

FAKULTÄT FÜR PHYSIK UND ASTRONOMIE

RUPRECHT-KARLS-UNIVERSITÄT HEIDELBERG

# Master Thesis in Physics

submitted by  
Lennart Hoenen  
born in Düren

June 5, 2025



# Manipulating and Probing Dysprosium with Near-Resonant Light

From sensitive imaging schemes for bosonic  
Dysprosium to slowing and cooling schemes for  
fermionic Dysprosium

This Master Thesis has been carried out by  
**Lennart Hoenen**

at the  
**Physikalisches Institut Heidelberg**

under the supervision of  
**Prof. Dr. Lauriane Chomaz**





# Abstract

This thesis reports on two separate projects that have been carried out for the two different Dy experiments in Heidelberg.

The first part focusses on improving an imaging system to enable the in-situ imaging of dense atomic clouds. The signal to noise ratios of different possible imaging schemes is calculated, a new phase contrast imaging setup is designed and a high intensity absorption imaging system, capable of imaging self-structured density modulated phases of Dy in-situ, is added. The alignment of absorption imaging arm is described, featuring the use of a Bahtinov-type mask.

Further the trapping of the fermionic isotope  $^{161}\text{Dy}$  in a 2DMOT is investigated using both analytical models and a numerical simulation. It is found, that due to the complex hyperfine structure of  $^{161}\text{Dy}$  the cooling transition cannot be considered to be a closed transition. Instead it is found that optical pumping to hyperfine states of small total atomic angular momentum  $F$  causes a depletion of the cooling transition at moderate magnetic fields of around 100 Gauss.



# Acknowledgements

First and foremost, I would like to express my deepest gratitude to Prof. Lauriane Chomaz for her continuous support and guidance throughout this journey. Her remarkable ability to maintain a calm and encouraging atmosphere, while entrusting me with challenging projects that taught me an incredible amount, made this thesis a rewarding and fun experience. I could not have imagined better supervision. It has been a privilege to work under her guidance, and I look forward to continuing this journey. Second, I would like to thank Prof. Selim Jochim for kindly agreeing to be the second examiner for this thesis.

A special thanks goes to Philipp Lunt for proofreading the thesis, and to Ximeng Song for providing the code that correctly sorts the hyperfine states of Dy. I am grateful to both of them for many insightful discussions on the trapping simulation.

I want to thank the entire DyLab team for essentially raising me academically and for being ever helpful. I want to thank the FerDy team for creating a fun and supporting environment to work in, and the BoDy team, especially Manon Ballu, for providing the images of the density-modulated phase used in this thesis.

Heartfelt thanks to Johannes and Kaddi for doing their very best to proofread this thesis.

And last, but by no means least, I would like to thank my parents, my sister, and again Kaddi for their unwavering support, and for being there, offering help and guidance whenever I needed it. They have made this thesis possible.



Erklärung:

Ich versichere, dass ich diese Arbeit selbstständig verfasst habe und keine anderen als die angegebenen Quellen und Hilfsmittel benutzt habe.

Heidelberg, den 05. Juni 2025

A handwritten signature in black ink, consisting of a stylized 'C' followed by a horizontal line and a small flourish.



# Contents

<b>1</b>	<b>Cold Quantum Gases</b>	<b>1</b>
1.1	Dipolar Quantum Gases . . . . .	1
1.1.1	Degenerate Quantum Gases . . . . .	1
1.1.2	Dipolar Atomic Interactions . . . . .	2
1.1.3	Supersolidity . . . . .	4
1.2	Dipolar Experiments in Heidelberg:	
	BoDy and FerDy . . . . .	5
1.2.1	BoDy Experiment . . . . .	5
1.2.2	FerDy Experiment . . . . .	7
<b>2</b>	<b>Atom Light Interactions</b>	<b>9</b>
2.1	Atomic Electronic Structure of Dysprosium . . . . .	9
2.2	Electronic Structure and Light Interactions . . . . .	12
2.2.1	Non-Relativistic Hamiltonian of a Many-Electron Atom . . . . .	12
2.2.2	Electronic Spin-Orbit Coupling . . . . .	15
2.2.3	Hyperfine Structure . . . . .	18
2.2.4	Atoms in a Magnetic Field . . . . .	19
2.2.5	Light-Atom Interactions . . . . .	22
2.2.6	Clebsch-Gordan Coefficients and Wigner Symbols . . . . .	24
2.3	Optical Trapping of Dysprosium Atoms . . . . .	27
2.3.1	Optical Molasses . . . . .	27
2.3.2	Zeeman Slowers . . . . .	28
2.3.3	Magneto Optical Traps . . . . .	29
2.3.4	Optical Dipole Traps . . . . .	31
<b>3</b>	<b>Imaging Ultracold Quantum Gases</b>	<b>33</b>
3.1	Imaging Optics . . . . .	33
3.1.1	Light Field Propagation through Optical Media . . . . .	34
3.1.2	Fourier Optics . . . . .	35
3.1.3	Resolution Limit . . . . .	40
3.1.4	4f-Imaging . . . . .	42

3.2	Overview of Imaging Schemes . . . . .	43
3.2.1	Absorption Imaging at Low and High Intensity . . . . .	44
3.2.2	Phase Contrast Imaging . . . . .	46
3.2.3	Fluorescence Imaging . . . . .	50
3.3	Noise and the Photon Transfer Curve . . . . .	51
3.3.1	Shot Noise . . . . .	52
3.3.2	Fixed Pattern Noise . . . . .	53
3.3.3	Read Noise . . . . .	53
3.3.4	Total Noise and Photon Transfer Curve . . . . .	54
<b>4</b>	<b>Design and Implementation of In-Situ Imaging Schemes for high OD in BoDy Experiment</b>	<b>55</b>
4.1	Characterisation of Imaging System . . . . .	55
4.2	Appropriate Probe Conditions . . . . .	58
4.2.1	Doppler Limit . . . . .	58
4.2.2	Random Walk Limit . . . . .	59
4.2.3	Pixel Saturation Limit . . . . .	59
4.3	Estimation of Signal to Noise Ratios for Different Imaging Schemes . . .	60
4.3.1	Signal to Noise Ratio for High Intensity Absorption Imaging . . . . .	60
4.3.2	Signal to Noise Ratio of Bright Background Dispersive Imaging . . . . .	63
4.3.3	Choice of Suitable Imaging Scheme . . . . .	65
4.4	Simulating Phase Contrast Imaging . . . . .	65
4.5	Design of new Phase Contrast Imaging Setup . . . . .	68
4.6	High Intensity Setup and Beam Shaping . . . . .	71
4.7	Alignment of a 4f Setup . . . . .	73
4.7.1	Alignment of 4f-setup with a large Gaussian beam . . . . .	75
4.7.2	Alignment of 4f-Setup with a Bahtinov-type mask . . . . .	76
4.7.3	In-Situ Images of Density Modulated States . . . . .	79
<b>5</b>	<b>Simulating <math>^{161}\text{Dy}</math> Trapping for FerDy Experiment</b>	<b>83</b>
5.1	Experimental Results from BoDy . . . . .	83
5.2	Analytical Model . . . . .	85
5.3	PyLCP Simulation . . . . .	92
5.3.1	PyLCP Overview . . . . .	92
5.3.2	Adaptations to PyLCP . . . . .	94
5.3.3	Limitations of the rate equation formalism and the PyLCP Package	95
5.3.4	Simulation Results . . . . .	96



5.4	Conclusions from Analytics and PyLCP . . . . .	98
<b>6</b>	<b>Outlook</b>	<b>101</b>

# Chapter 1

## Cold Quantum Gases

### 1.1 Dipolar Quantum Gases

#### 1.1.1 Degenerate Quantum Gases

In his 1924 PhD Thesis [Bro24], Louis de Broglie discovered, that not only photons have both wave- and particle-like behaviour, but that this dualism extends to particles. He found that any particle can be associated with a wavelength, that depends on the particles energy. In an ideal thermal gas that contains only point-like particles that can collide purely elastically, the momentum distribution of these particle is given by Boltzmann statistics. The *de Broglie wavelength* associated with each particle is then given by [FF12]:

$$\lambda_T = \frac{\hbar}{\sqrt{mk_B T}} \quad (1.1)$$

where the particle has a mass  $m$  and temperature  $T$  and where  $\hbar$  and  $k_B$  are the reduced Planck constant and the Boltzmann constant. In the classical limit, where  $\hbar \ll T$  this wavelength is very small and has negligible effect. Explicitly in this case, the inter-particle distance  $n^{-1/3}$  in a thermal gas of density  $n$  is much greater than the de Broglie wavelength and the density in the space of all states approaches  $n\lambda^3 \approx 1$ .

If the temperature of the gas reduced to near zero, however, the de Broglie wavelength can become comparable to or greater than the inter-particle distance. Around this temperature, the wave-like behaviour of the individual atoms can no longer be neglected and the gas will start to exhibit quantum behaviour. To better understand this regime of cold quantum gases, the distinction between fermions (particles with half-integer spin) and bosons (particles with integer spin) is necessary. One isotope of some element may be fermionic and another may be bosonic. While this difference in overall spin may appear harmless, it fundamentally changes the behaviour of the particles close to zero temperature.

Fermions follow *Fermi-Dirac statistics*, where the average number of fermions in some

state  $i$  is given by [FF12]:

$$\bar{n}_i = \frac{1}{\exp[(\varepsilon_i - \mu)/k_B T] + 1} \quad (1.2)$$

where  $\varepsilon_i$  is the energy of the state  $i$  and  $\mu$  is the chemical potential.

Bosons on the other hand, follow *Bose-Einstein statistics*, where the average number of bosons in some state  $i$  is given by [FF12]:

$$\bar{n}_i = \frac{g(\varepsilon)}{\exp[(\varepsilon_i - \mu)/k_B T] - 1} \quad (1.3)$$

where  $g(\varepsilon)$  is the density of states at the energy  $\varepsilon_i$ . At ‘high’ temperature and ‘low’ particle density (e.g. for an ideal gas at room temperature and pressure) both these distributions approach the *Maxwell-Boltzmann distribution*. At temperatures close to absolute zero, both fermions and bosons may condense to form degenerate gases. Due to their fundamentally different nature these processes become distinct. Here the condensation of Bosons in a harmonic trap will be described briefly.

In a harmonic trap, the density of states of Bosons at energy  $\varepsilon$  can be found to be [FF12]:

$$g(\varepsilon) = \frac{\varepsilon^2}{2\hbar^3\omega^3} \quad (1.4)$$

The chemical potential  $\mu$  depends on the particle density and temperature and under room conditions it is large and negative. It decreases with temperature however and (in the case of bosons) when it approaches the lowest state energy  $\mu \approx \varepsilon_0$ , the average number of bosons in state  $\varepsilon_0$  diverges. This condition defines the critical temperature  $T_c$ , below which the thermal gas undergoes a phase transition and the particles collapse/condense into the single state with energy  $\varepsilon_0$ . In a harmonic trap with a mean trapping frequency  $\omega_0 = (\omega_x\omega_y\omega_z)^{1/3}$  the critical temperature can be found to be [FF12]:

$$T_c \approx 0.94 \frac{\hbar\omega}{k_B} N^{1/3} \quad (1.5)$$

Below this critical temperature the gas form a *Bose-Einstein Condensate* (BEC). In this case, all particles can be described by a single macroscopic wavefunction that extents over the whole system

$$\psi = \sum_j^N \psi_j = N\psi_j \quad (1.6)$$

where the wavefunction  $\psi_j$  describes a single particle.

### 1.1.2 Dipolar Atomic Interactions

In BECs realized in experiments, interactions between the particles, that have so far been neglected, have to be taken into account. At the low temperature limit and at large

inter-particle spacing, the *van der Waals interaction* between two natural particle may well be described by s-wave scattering. In this limit the two-body contact interaction can be approximated by the isotropic potential

$$V_c(\mathbf{r} - \mathbf{r}') = g_s \delta(\mathbf{r} - \mathbf{r}') \quad (1.7)$$

where  $g_s = 4\pi\hbar^2 a_s/m$  and  $a_s$  is the s-wave scattering length, which can be widely tuned by exploiting *Feshbach resonances*. Experimentally, that means by merely tuning a constant offset magnetic field, the s-wave scattering length can be chosen over a large range of values.

In a gas with many particles, a solution accounting for interactions between each and every particle cannot be found. Instead the interaction can be treated as an effective mean field potential acting on the  $i$ th particle, given by [FF12]

$$V_c(\mathbf{r}_i) = \sum_{j \neq i} g_s \delta(\mathbf{r} - \mathbf{r}') \approx g_s n(\mathbf{r}_i) \quad (1.8)$$

where  $n(\mathbf{r}_i)$  is the local density.

In the case of Dysprosium (Dy), with a large magnetic moment  $\mu_m$ , the dipole-dipole interaction between the atoms has to be accounted for as well. Within an external magnetic field the dipoles become polarised and the dipole-dipole interaction can be described by [Cho25]:

$$V_{dd}(\mathbf{r} - \mathbf{r}') = \frac{3g_{dd}}{4\pi r^3} (1 - 3\cos^2 \theta) \quad (1.9)$$

where  $r = |\mathbf{r} - \mathbf{r}'|$ ,  $\theta$  is the angle between the magnetic field  $\mathbf{B}$  and the inter-particle position  $\mathbf{r} - \mathbf{r}'$  and where  $g_{dd} = 4\pi\hbar^2 a_{dd}/m$  is the coupling constant, associated with the dipolar length  $a_{dd} = m\mu_B\mu_m^2/12\pi\hbar^2$ . The dipole-dipole interaction potential is anisotropic and may be attractive, repulsive or zero, depending on the angle  $\theta$ . In the case of Dy  $a_{dd} \approx 130a_0$  where  $a_0$  is the *Bohr radius* and with the scaling of  $1/r^3$  the dipole-dipole interaction remains long-range and anisotropic in the regime of cold quantum gases.

The relative importance of the contact and dipole-dipole interaction can be tuned with a magnetic field. Feshbach resonances can be exploited [Cho+19] by tuning the magnitude of the magnetic field and the character of the dipole interaction can be tuned by the direction of the magnetic field. Magnetic lanthanide atoms exhibit a dense spectrum of Feshbach resonances at low magnetic fields, such that both  $a_s$  and  $\theta$  can be tuned easily in experiment.

Accounting for both contact and dipolar interactions, a weakly interacting BEC at very low temperature, where nearly all particles have condensed, the system may well be described by a classical complex field  $\psi(\mathbf{r})$ , that embodies the macroscopic wavefunction, but neglects its fluctuations and where all interactions are only accounted for in a mean-

field approach [Cho25]. The total particle number is then given by  $N = \int |\psi(\mathbf{r})|^2 d^3r$ , while the local density is  $n(\mathbf{r}) = |\psi(\mathbf{r})|^2$ . Within this description, the system obeys the *Gross-Pitaevskii equation* (GPE)

$$i\hbar \frac{\partial \psi}{\partial t} = \left[ -\frac{\hbar^2 \Delta}{2m} + V(r) + g_s n(r) + \Phi_{dd}(r) \right] \psi. \quad (1.10)$$

where the first two terms give the kinetic and potential energy analogous to a Schrödinger equation and the last two terms describe the mean-field contact and dipole-dipole interaction. The latter is given by

$$\Phi_{dd}(\mathbf{r}) = \int V_{dd}(\mathbf{r} - \mathbf{r}') n(\mathbf{r}') d^3r' \quad (1.11)$$

### 1.1.3 Supersolidity

By investigating the dispersion relation of the solutions to the GPE interesting observations can be made. In the absence of any confinement, the fundamental excitations of a Bose gas are plane waves of momentum  $\mathbf{k}$ . The energies of these excitations can be found to be [Cho25]:

$$\varepsilon(\mathbf{k}) = \sqrt{\frac{\hbar^2 k^2}{2m} \left( \frac{\hbar^2 k^2}{2m} + 2\tilde{V}_{\text{int}}(\mathbf{k})n \right)}, \quad (1.12)$$

where  $\tilde{V}_{\text{int}}(\mathbf{k})$  is the total interaction potential  $V_{\text{int}}(\mathbf{r}) = V_{dd}(\mathbf{r}) + V_c(\mathbf{r})$  in momentum space which is given by the Fourier transform of the total interaction potential:

$$\tilde{V}_{\text{int}}(\mathbf{k}) = g_s + g_{dd}(3 \cos(\theta_k)^2 - 1) \quad (1.13)$$

Thus the energy of the excitations become dependent on  $\theta$ , the angle between the  $\mathbf{k}$  and the dipole axis, and can both increase and decrease, depending on the value of  $\theta$ . In 2015 it was shown experimentally [Kad+16] that this can lead to self-structured and self-stabilised density modulations *in the ground state* of a strongly confined dipolar quantum gas. Exemplary pictures from the report on this first discovery are shown in Figure 1.1. Furthermore, theory predicts [RBB23; Her+21] a small zoo of different supersolid phases, forming droplets, stripes, honeycombs and more. These formation of these states and the transitions between them are studied currently being studied in the bosonic Dy experiment in Heidelberg. This thesis will partly focus on improvement to the imaging system of the bosonic Dy experiment and partly on the development of a new experiment, able to trap fermionic Dy. A short overview on both experiments is given in the following section.

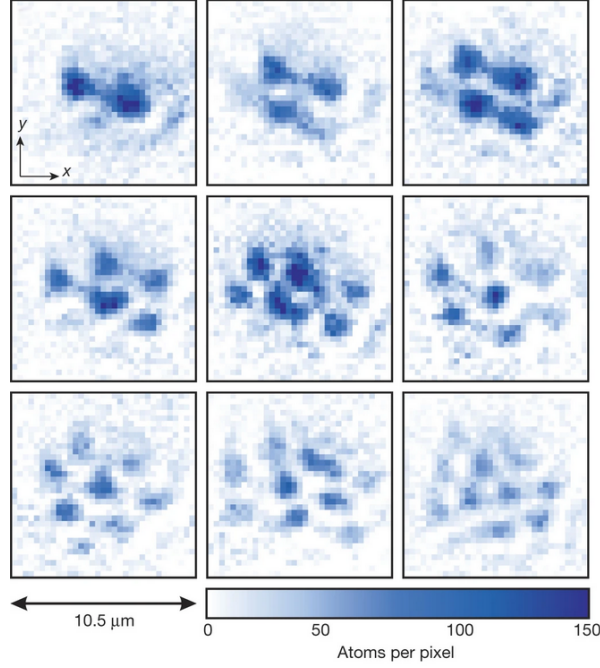


Figure 1.1: Single shot in-situ images of self-structured droplets in a confined dipolar quantum gas of Dy. Figure adapted, taken from [Kad+16]

## 1.2 Dipolar Experiments in Heidelberg: BoDy and FerDy

In the following section, an overview of the two Dysprosium experiments in our group will be given and the contents of this thesis will be associated with the two experiment.

### 1.2.1 BoDy Experiment

In the recent years a new experiment was built to study bosonic Dysprosium (BoDy). Due to the large magnetic moment  $\mu_m \approx 10$  of Dy, the atoms exhibit strong, long-range dipolar interactions. As described in the previous section, under 2D confinement and at large densities, this can lead to interesting and novel self-structured phases of matter.

An overview of the experimental layout is given in Figure 1.2. The experiment consists mainly of an oven, a 2DMOT chamber and a 3DMOT chamber. The novel design does not feature a Zeeman Slower, but instead loads the permanent magnet 2DMOT from a thermal jet of atoms directly [Jin+23]. From the 2DMOT, atoms may be transferred to a 3DMOT with a push beam. The metallic chamber surrounding the 3DMOT contains large, re-entrant viewports in the vertical direction to enable the use of a high NA objective. From the 3DMOT they may be transferred to an accordion lattice and an optical dipole trap at the same place.

The BoDy experiment currently focusses on self-structured density modulated states similar to those depicted in Figure 1.1. The focus especially lies on whether these state

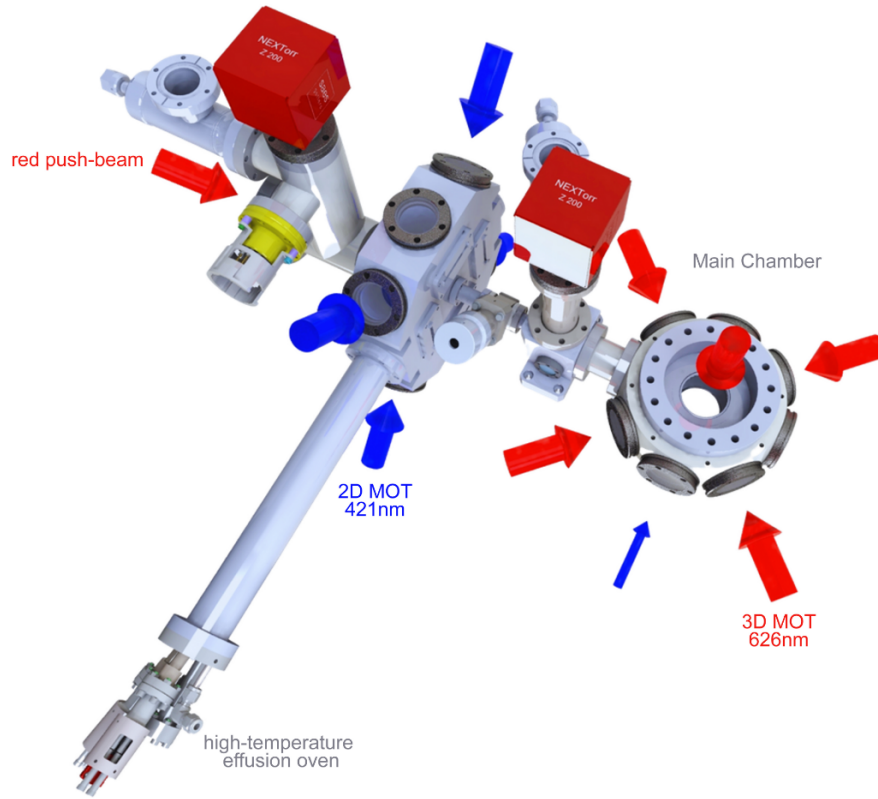


Figure 1.2: Overview of the experimental setup of BoDy. Arrows indicate the blue 421nm and the red 626nm light that is mainly used for the MOTs and transfer. On the lower left, the effusion oven can be seen. The long, water-cooled arm entails a large crucible and the aperture of the oven extends slightly into the 2DMOT chamber (middle). The upper left side of the schematic contains pumps for the high vacuum section of the experiment and a viewport for the push beam that transfers atoms from 2DMOT to 3DMOT. Just after the 2DMOT a valve, a differential pumping stage and a pump for the ultra-high vacuum section are positioned. Finally on the right hand side, the octagonal 3DMOT chamber with the re-entrant viewports on the top and bottom can be seen. Figure taken from [Sil23]

form a supersolid, a state of matter that has both the superfluid property of frictionless flow and the long-range order of a crystalline solid. Also identifying the regimes of different supersolid phases & the nature of the phase transitions between them will be studied. As these fragile but highly dense states form on small length scales inside a high-vacuum chamber, measuring their density profiles requires some thought. Chapter 4 will describe the development two imaging schemes able to image these structures in-situ. Chapter 3 will introduce the physical concepts relevant to imaging.

### 1.2.2 FerDy Experiment

While the BoDy experiment reaches ‘completion’, a new experiment is being designed that will be able to study fermionic Dysprosium (FerDy).

As will be seen later on in this thesis, the trapping of fermionic Dy in a 2DMOT is rather more complicated than in the bosonic case due to the complex hyperfine structures of the fermions. That means a Zeeman slower will have to be re-incorporated into the design. The slowed atomic jet will then be deflected by an angled 2DMOT into a 3DMOT. The 3DMOT will be contained in a glass cell, surrounded by a modular arrangement of breadboard pieces following the design of the *Heidelberg Quantum Architecture* [Ham+25]. Equally, the whole vacuum setup will be movable, so that the point in space where the atoms are trapped is accessible.

Once the atoms are trapped in a 3DMOT, they will be transferred into an optical tweezer where the number of fermions can be, controlled precisely by reducing the trap depth and thus ‘spilling’ almost all atoms out of the tweezer [Ser+11]. With few atoms of well controlled number, the crossover between few- and many-body physics and the emergence of collective behaviour in few dipolar atoms will be studied.

Within this thesis, the trapping of  $^{161}\text{Dy}$ , especially in a 2DMOT, was investigated both analytically and with a numerical simulation. The relevant physical concepts will be introduced in Chapter 2 and the results of the simulation and analytical consideration will be presented in Chapter 5.





# Chapter 2

## Atom Light Interactions

Accurate manipulation and trapping of atoms relies on a good understanding of their internal structure and of their interaction with light. Specifically, trapping fermionic Dy requires a good understanding of its electronic structure including the availability of closed transition and their hyperfine structure. As the interaction of fermionic Dy and light be analysed analytically and numerically (see Chapter 5), a brief overview will on the most important aspects involved will be given in the following. First, some data on the relevant Dy isotopes and their optical transition will be listed. Then, the Hamiltonian of an atom with many electrons will be introduced, then the dependence of electronic energy levels on external magnetic fields will be discussed and finally the interaction with light will be described.

### 2.1 Atomic Electronic Structure of Dysprosium

Dysprosium is a lanthanide with atomic number 66. It has a metallic silver surface and a melting point of 1412°C [You11], but at low pressures Dy will sublime at significantly lower temperatures so that even at an oven temperature of  $T=800^\circ\text{C}$  (with a hotlip temperature of  $1100^\circ\text{C}$ ) the atomic flux is high enough to collect the atoms in a 2DMOT, without using a Zeeman slower [Jin+23]. The four isotopes  $^{161}\text{Dy}$  to  $^{164}\text{Dy}$  are roughly equally abundant (see Table 2.1), while the remaining stable isotopes make up less than 3%. With a value of  $\mu_m = 10\mu_B$  (where  $\mu_B$  is the Bohr magneton), Dysprosium (together with Terbium) has the highest atomic magnetic moment of all elements. The availability of both fermionic and bosonic isotopes of an element with a strongly dipolar character (due to the magnetic moment) makes Dy an interesting element to study in the regime of ultra-cold quantum gases. The anisotropic interatomic interaction gives rise to new physics, while the availability of Feshbach resonances allows the character of the interatomic interactions to be tuned conveniently.

The electronic ground state of Dy is given by [Mai15]:

$$[\text{Xe}]4f^{10}6s^2 \quad (2.1)$$

where [Xe] indicates the closed shell configuration of the noble gas Xenon, which contains 54 electrons. The remaining 12 electrons are distributed in the  $4f$  and  $6s$  shells. While the closed  $6s$  shell does not contribute to the ground state quantum numbers, the 10 electrons in the  $4f$  shell combine to maximise both the total spin  $S = 2$  and the total orbital angular momentum  $L = 6$ . The ground state may be described with L-S coupling, giving rise to a total angular momentum quantum number of  $J = L + S = 8$ . The ground state electronic configuration may thus be expressed by the term symbol  $^5I_8$ .

The nuclear spin of  $I = 5/2$  of the fermionic isotopes gives rise to a hyperfine structure (see Section 2.2.3) with hyperfine coefficients  $A_{HFS}$  and  $B_{HFS}$  which connect to the magnetic dipole and the electric quadrupole moments in the atom-light interaction, that be found in Table 2.1. The nuclear magnetic moment associated with the nuclear spin is given in Table 2.1 as well.

Isotope	$^{160}\text{Dy}$	$^{161}\text{Dy}$	$^{162}\text{Dy}$	$^{163}\text{Dy}$	$^{164}\text{Dy}$	Reference
Abundance [%]	2.3	18.9	25.5	24.9	28.2	[Mei+16]
Mass [u]	159.9	160.9	161.9	162.9	163.9	[Lae+09]
Nuclear spin $I$	0	$5/2$	0	$5/2$	0	[LCB09]
Nuclear Magn. Mom. $\mu_I [\mu_N]$	0	-0.4806	0	0.6726	0	[Mer25]
<i>Ground state</i>						
$A_{HFS}$ [MHz]	–	-116.2	–	162.8	–	[FDG74]
$B_{HFS}$ [MHz]	–	1091.6	–	1152.9	–	[FDG74]
<i>Excited state 421nm</i>						
$A_{HFS}$ [MHz]	–	-86.9	–	121.6	–	[LCB09]
$B_{HFS}$ [MHz]	–	1747.4	–	1844.9	–	[LCB09]

Table 2.1: Nuclear and atomic properties of dysprosium isotopes  $^{160}\text{Dy}$  through  $^{164}\text{Dy}$ . The ground state is the  $4f^{10}6s^2 \ ^5I_8$  state. The excited state  $4f^{10}6s^2(^5I_8) \ 6s6p(8,1)_9$  belongs the 421nm cooling transition.

Dysprosium features a complex electronic excitation spectrum. An overview can be seen in Figure 5.1. The strongest transition, frequently used for slowing and cooling is the broad 421nm transition between the ground state and the excited state  $4f^{10}6s^2(^5I_8) \ 6s6p(^1P_1) \ (8,1)_9$ . As indicated by the  $4f^{10}6s^2(^5I_8)$  term, the electrons in the submerged half-filled  $f$  shell remain unaffected in this transition. However one of the  $6s^2$  electrons is lifted into the  $p$  orbital giving rise to the singlet state  $^1P_1$  (where the odd parity is sometimes indicated by  $^1P_1^\circ$ ). The excited state is best described in jj-coupling, where the electrons in the  $f$  shell with  $J = 8$  couple to the singlet with  $J = 1$  to give the total electronic angular momentum  $J = 9$ , described by the coupling term  $(8,1)_9$ . For

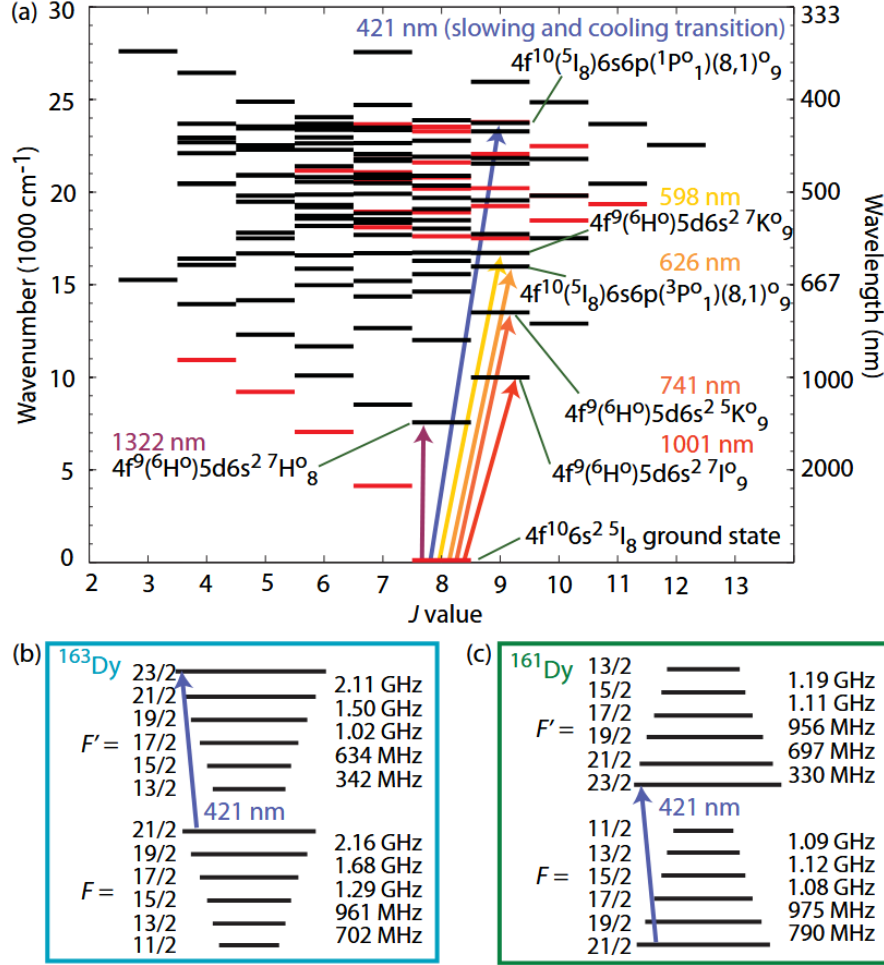


Figure 2.1: (a) Overview of the spectrum of electronic states. The arrows indicate different transitions relevant to trapping and cooling Dy. Within this thesis the 421nm and 626nm transitions are relevant especially. (b) Illustrates the hyperfine structure of  $^{163}\text{Dy}$ . The arrow indicates the closed 421nm cooling transition. (c) Illustrates the hyperfine structure of  $^{161}\text{Dy}$  where the arrow again indicates the closed 421nm cooling transition. Figure taken from [You+10]

the ground state, the Landé factor associated with the total angular momentum is given by  $g_J^g = 1.242$  while for the excited state it is  $g_J^e = 1.22$  [You11].

Similarly, the  $6s^2(^1S_0)$  electrons can be excited into a triplet configuration  $6s6p(^3P_1)$ . Transitions between different spin multiplicities are typically called ‘spin-forbidden’ as they are not allowed in pure LS-coupling. Due to a more complex structure in the complex electronic configuration of Dy, the transition is allowed with a small probability. This gives rise to the narrow inter-combination 626nm line where the excited state is described by  $4f^{10}6s^2(^5I_8)6s6p(^3P_1)(8,1)_9$ . The narrow linewidth allows both to choose large relative detunings (that can be useful in dipole traps and imaging schemes) and reduces the recoil temperature.

An overview on the relevant parameters of the 421nm and the 626nm transitions is

given in Table 2.2.

## 2.2 Electronic Structure and Light Interactions

### 2.2.1 Non-Relativistic Hamiltonian of a Many-Electron Atom

To understand the electronic structure of Dy  $Z = 66$  protons and  $N = 66$  electrons with charge  $e$  and mass  $m_e$  we will write down the Hamiltonian for the interaction of the electrons and the nucleus. Here, the approaches presented in Foot's *Atomic Physics* [Foo05a; Foo05b] and in Bransden & Joachain's *Physics of Atoms and Molecules* [BJ83a; BJ83b] will be followed. Both provide comprehensive and rigorous derivations of the relevant concepts. The nucleus will be assumed to be point-like and of infinite mass and only kinetic and electrostatic energies will be included (for now). In this case we can write the non-relativistic Hamiltonian as:

$$\hat{H}_0 = \sum_{i=1}^N \left( -\frac{\hbar^2}{2m_e} \nabla_{r_i}^2 - \frac{Ze^2}{4\pi\epsilon_0 r_i} \right) + \sum_{i<j=1}^N \frac{e^2}{4\pi\epsilon_0 r_{ij}} \quad (2.2)$$

where  $r_i = |\mathbf{r}_i|$  is the distance between one electron and the nucleus and  $r_{ij} = |\mathbf{r}_i - \mathbf{r}_j|$  is the distance between two electrons.  $\hbar$  is the reduced Planck constant and  $\epsilon_0$  is the vacuum permittivity. For now relativistic and quantum fluctuation effects will be neglected.

The Schrödinger equation for the atomic wavefunction  $\Psi(q_1, q_2, \dots, q_N)$  is then given by:

$$\hat{H}_0 \Psi(q_1, q_2, \dots, q_N) = E \Psi(q_1, q_2, \dots, q_N) \quad (2.3)$$

where the  $q_i$  describe the spatial ( $\mathbf{r}_i = (r_i, \theta_i, \varphi_i)$ ) and spin ( $s_i$ ) coordinates of the electrons. As the  $N$  electrons are indistinguishable fermions, the Hamiltonian must be invariant under exchange of any two electrons and the total wavefunction  $\Psi$  must be anti-symmetric.

Because the Hamiltonian 2.2 does not depend on the spin of the electrons, the Schrödinger equation may equally be written in terms of a purely spatial wavefunction  $\psi(\mathbf{r}_1, \mathbf{r}_2, \dots, \mathbf{r}_N)$ . Using atomic units to further declutter the notation the Schrödinger equation reads:

$$\left[ \sum_{i=1}^N \left( -\frac{1}{2} \nabla_{r_i}^2 - \frac{Z}{r_i} \right) + \sum_{i<j=1}^N \frac{1}{r_{ij}} \right] \psi(\mathbf{r}_1, \mathbf{r}_2, \dots, \mathbf{r}_N) = E \psi(\mathbf{r}_1, \mathbf{r}_2, \dots, \mathbf{r}_N) \quad (2.4)$$

The term  $1/r_{ij}$  prohibits us from separating this  $3N$  dimensional differential equation and as the sum of all these inter-electronic interactions can (for the outer electrons for example) become comparable to the strength of interaction of between electron and nucleus, we cannot treat this term perturbatively.

Instead we approximate this hamiltonian by treating each electron as an independent particle, moving in the Coulomb potential of the nucleus and the averaged Coulomb potential of all other  $(N - 1)$  electrons. This centrally symmetric potential may be written for some electron  $i$  as:

$$V(r_i) = \langle \psi | \sum_{i \neq j}^N \frac{1}{r_{ij}} | \psi \rangle \quad (2.5)$$

With this *central field approximation* we can rewrite Equation (2.2) as:

$$\hat{H} = \sum_i^N \left( -\frac{1}{2} \nabla_{r_i}^2 - \frac{Z}{r_i} \right) + \sum_{i < j=1}^N \frac{1}{e_{ij}} \quad (2.6)$$

and by adding and subtracting the potential  $V(r_i) = -Z/r_i + S(r_i)$ , the central field Hamiltonian can be separated into a centrally symmetric part  $\hat{H}_c$  and (small) not necessarily spherically symmetric correction to the centrally symmetric part  $\hat{H}_{nc}$  as:

$$\hat{H}_0 = \hat{H}_c + \hat{H}_{nc} \quad (2.7)$$

$$\hat{H}_c = \sum_{i=1}^N \left( -\frac{1}{2} \nabla_{r_i}^2 + V(r_i) \right) \quad (2.8)$$

$$\hat{H}_{nc} = \sum_{i < j=1}^N \frac{1}{r_{ij}} - \sum_i^N \left( \frac{Z}{r_i} + V(r_i) \right) \quad (2.9)$$

$$= \sum_{i < j=1}^N \frac{1}{r_{ij}} - \sum_i^N S(r_i) \quad (2.10)$$

The energy contribution of  $\hat{H}_{nc}$  is much smaller than that of  $\hat{H}_c$  and the former can be treated as perturbation to the latter.

Finding a good approximation of  $V(r_i)$  at all radii is no trivial task but can be done with several methods such as the Thomas-Fermi and Hatree-Fock methods [BJ83b] or by the the density functional theory [AF05]. A full discussion of these methods exceeds the scope of this thesis, however the potential can be readily approximated for neutral atoms ( $Z = N$ ) at small and large radii by:

$$V(r_i) \rightarrow -\frac{Z}{r_i} \quad r \rightarrow 0 \quad (2.11)$$

$$V(r_i) \rightarrow -\frac{1}{r} \quad r \rightarrow \infty \quad (2.12)$$

In other words, for an electron far away from the nucleus the Coulomb interaction of the  $Z = N$  protons is shielded by the remaining  $N - 1$  electrons, whereas close to the nucleus the full potential of the  $Z = N$  protons acts on the electron.

Closed subshells will not contribute to the non-central part of the hamiltonian, an most of the electronic structure may be captured by  $\hat{H}_c$  alone. Within the central field approximation, neglecting the perturbation  $\hat{H}_{nc}$  the Schrödinger equation can now be written as:

$$\hat{H}_c \psi_c(\mathbf{r}_1, \mathbf{r}_2, \dots, \mathbf{r}_N) = \sum_{i=1}^N \left( -\frac{1}{2} \nabla_{r_i}^2 + V(r_i) \right) \psi_c(\mathbf{r}_1, \mathbf{r}_2, \dots, \mathbf{r}_N) = E_c \psi_c(\mathbf{r}_1, \mathbf{r}_2, \dots, \mathbf{r}_N) \quad (2.13)$$

This equation is now separable into  $N$  equations for  $N$  electrons. The electronic wavefunction  $\psi_c(q_1, q_2, \dots, q_N)$  which has to satisfy the *Pauli exclusion principle* can be determined by calculating the *Slater determinant* (see [BJ83b]). It may be written as:

$$\psi_c(\mathbf{r}_1, \mathbf{r}_2, \dots, \mathbf{r}_N) = u_{nlm_l}^1(\mathbf{r}_1) \cdot u_{nlm_l}^2(\mathbf{r}_2) \cdot \dots \cdot u_{nlm_l}^N(\mathbf{r}_N) \quad (2.14)$$

where each of the central one-electron orbitals  $u_{nlm_l}^i(\mathbf{r}_i)$  are products of radial functions and spherical harmonics that come from the analytical solution of the Hydrogen atom:

$$u_{nlm_l}^i(\mathbf{r}_i) = R_{nl}(r_i) Y_{lm_l}(\theta_i, \phi_i) \quad (2.15)$$

Here, the spin of the electrons can be reintroduced by simply multiplying the orbitals with spin-1/2 eigenfunctions  $\chi_{m_s}$  as:

$$u_{nlm_l m_s}^i(\mathbf{r}_i) = \chi_{m_s} R_{nl}(r_i) Y_{lm_l}(\theta_i, \phi_i) \quad (2.16)$$

$$E_{nl}^i u_{nlm_l m_s}^i(\mathbf{r}) = \left( -\frac{1}{2} \nabla_r^2 + V(r) \right) u_{nlm_l m_s}^i(\mathbf{r}) \quad (2.17)$$

and

$$E_c = \sum_i E_{nl}^i \quad (2.18)$$

The  $n, l, m_l$  are the quantum numbers with

$$n = 1, 2, \dots \quad (2.19)$$

$$l = 0, 1, \dots, n-1 \quad (2.20)$$

$$m_l = -l, -l+1, \dots, l-1, l \quad (2.21)$$

$$m_s = \pm \frac{1}{2} \quad (2.22)$$

The orbital angular momentum of the electrons  $\mathbf{L}$  has the simultaneous eigenstates to the operators  $\mathbf{L}^2$  and  $\mathbf{L}_z$ , that are described by the quantum numbers  $l$  and  $m_l$ . The energies  $E_{nl}^i$  will be  $2(2l+1)$  times degenerate and only give a first approximation of course. To describe the electronic energy levels within an atom to a meaningful degree of precision

further corrections will have to be included, which can be treated as a perturbation to  $\hat{H}_c$ .

### 2.2.2 Electronic Spin-Orbit Coupling

So far, only the Coulomb interactions between electrons and the nucleus was included into the Hamiltonian. To improve the central field approximation relativistic corrections will have to be included that give rise to the coupling the electronic spin  $\mathbf{S}$  and the electronic angular momentum  $\mathbf{L}$  (Spin-Orbit coupling), a relativistic correction to the electronic mass and the Darwin term. In total these corrections give rise to the *fine structure* which splits degenerate energies  $E_{nl}$ . In the following an overview on the Spin-Orbit coupling will be given, as similar concepts will become relevant in the later discussion of the hyperfine structure of Dy.

For an independent electron in a central field given by a potential  $V(r_i)$ , the spin-orbit-coupling term can be written as:

$$\hat{H}_{so} = \sum_i \frac{1}{2m_e^2 c^2 r_i} \frac{dV(r_i)}{dr_i} \mathbf{L}_i \cdot \mathbf{S}_i \quad (2.23)$$

where  $\mathbf{L}_i$  is the orbital angular momentum,  $\mathbf{S}_i$  is the spin angular momentum of an electron and  $m_e$  is its mass.

It turns out that only partially filled subshells contribute to the spin-orbit coupling and that the relative strength of the terms  $\hat{H}_{nc}$  and  $\hat{H}_{so}$ , depends on the nuclear charge number  $Z$ . For small  $Z$ , in the so-called *LS-coupling regime*,  $\hat{H}_{so}$  may be treated as a perturbation to  $\hat{H}_c + \hat{H}_{nc}$ . For large  $Z$  however, in the *jj-coupling regime*, the term  $\hat{H}_{so}$  has a much stronger contribution than the electrostatic correction term  $\hat{H}_{nc}$  and in turn  $\hat{H}_{nc}$  may be treated as a perturbation to  $\hat{H}_c + \hat{H}_{so}$ .

The case of Dysprosium with  $Z = 66$  actually lies somewhere in between these regimes, while the atomic ground state may be described by LS-coupling the excited state of the 421nm transition is better described in jj-coupling. To illustrate this transition from the LS to jj-coupling regime, Figure 2.2 shows the fine-structure of the first excited  $^1P$  and  $^3P$  terms along the carbon sequence. At small  $Z$ , the levels are first split according to their orbital quantum number  $L$  and the electronic spin quantum number  $S$  and at large  $Z$  split according to the total angular momenta of the electrons  $j_i$ . Here the the coupling regimes and the resulting energy shifts will be described briefly, following [BJ83b].

#### LS-Coupling

If the Spin-Orbit coupling hamiltonian  $\hat{H}_{so}$  contributes much weaker to the electronic energy levels, than the non-central hamiltonian  $\hat{H}_{nc}$ , the eigenstates of  $\hat{H}$  can be calculated



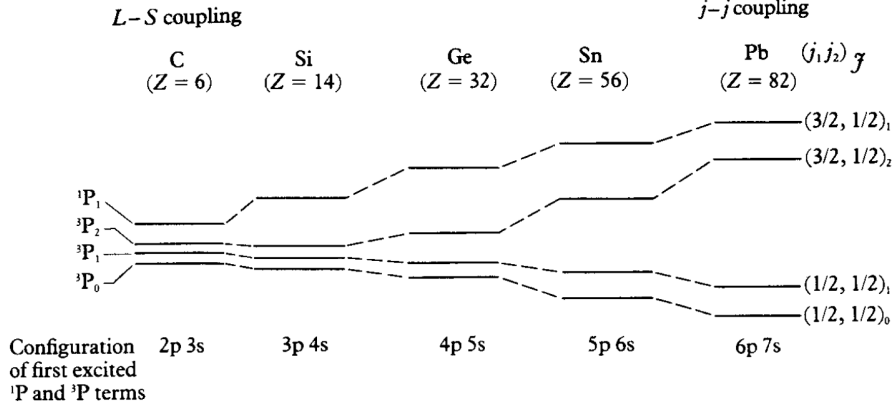


Figure 2.2: Energy levels of the first excited  $^1P$  and  $^3P$  states along the carbon sequence. The transition from the LS-coupling regime at small  $Z$  to the jj-coupling regime at large  $Z$  can be seen. Within the LS-coupling regime the electronic states are described by the term symbol  $^{2+1}L_J$ , in the jj-coupling regime they are described by the term  $(j_1, j_2)_J$ . Figure taken from [BJ83b].

by treating  $\hat{H}_{so}$  as a perturbation as:

$$\hat{H} = \hat{H}' + \hat{H}_{so} \quad (2.24)$$

where  $\hat{H}' = \hat{H}_c + \hat{H}_{nc}$ . To do so, first the eigenfunctions of  $\hat{H}'$  have to be found by diagonalizing the perturbation  $\hat{H}_{nc}$  within the degenerate manifold of  $\hat{H}_c$ , and treating  $\hat{H}_{so}$  as a first order perturbation to  $\hat{H}_c$ , yielding corrected eigenstates.

To find the fine-structure corrections on these states, the perturbation  $\hat{H}_{so}$  now has to be included. As  $\hat{H}_{so}$  will clearly *does* depend on  $\mathbf{L}$  and  $\mathbf{S}$ , a change of basis is necessary. By changing from the basis  $|sLSm_Lm_S\rangle$  to  $|sLSJm_J\rangle$  new eigenstates can be found, described by the *Russel-Sounders term symbol*  $^{2S+1}L_J$  that are  $2J + 1$  times degenerate in  $m_J$ . The energies of these states with respect to the term  $^{2S+1}L$  is given by:

$$E(J) = \frac{A_{FS}}{2} [J(J+1) - L(L+1) - S(S+1)] \quad (2.25)$$

and an energy spacing between levels of  $E(J) - E(J-1) = A_{FS}J$ .

The change of basis from  $|sLSm_Lm_S\rangle$  to  $|sLSJm_J\rangle$  is dictated by the *Clebsch-Gordan Coefficients*.  $|sLSJm_J\rangle$  can be expressed in the basis of  $|sLSm_Lm_S\rangle$  as:

$$|sLSJm_J\rangle = \sum_{m_L, m_S} C(LSJm_Lm_Sm_J) |sLSm_Lm_S\rangle \quad (2.26)$$

where  $C(LSJm_Lm_Sm_J)$  are the Clebsch-Gordan Coefficients.

## jj-Coupling

In contrast, in the jj-coupling case the the hamiltonian  $\hat{H}_{nc}$  will be treated as a perturbation with

$$\hat{H} = \hat{H}' + \hat{H}_{nc} \quad (2.27)$$

where  $\hat{H}' = \hat{H}_c + \hat{H}_{so}$ . The eigenstates of  $\hat{H}'$  will in this case be fully characterised by a set of  $(j_1, j_2, \dots, j_N)$  for  $N$  electrons.

The spin orbit term splits the degenerate energy levels  $E_{nl}$  (for  $l \neq 0$ ) into two sublevels levels  $E_{nlj}$ . One electron with spin  $\mathbf{s} = \pm 1/2$  couples to its orbital momentum  $\mathbf{l}$  to  $\mathbf{j} = \mathbf{l} + \mathbf{s}$  with the quantum number  $j = l \pm 1/2$ . Because of this splitting in sub levels with a quantum number  $j$ , this regime is called *jj-coupling* regime. Including the smaller perturbation of  $\hat{H}_{nc}$ , the eigenenergies of  $\hat{H}'$  are again split into sublevels according to the angular momentum  $\mathbf{j}$ , where each sublevel  $E_{nlj}$  remains  $2j + 1$  times degenerate.

For the excited states of Dysprosium relevant here, the special case of  $J_1 J_2$ -coupling is applicable[Ilz20]. Here the inner electrons of the closed subshells in the [Xe] configuration couple together to  $\mathbf{J}_1$  with quantum number  $J_1$  while the outer electrons in the 6s shell couple together to  $\mathbf{J}_2$  with quantum number  $J_2$ . They then couple to give the total angular momentum  $\mathbf{J} = \mathbf{J}_1 + \mathbf{J}_2$  with quantum number  $J$ . The (excited) state is then described by the notation  $(J_1, J_2)_J$  [Fri14]. Within this description the 421nm and the 626nm transitions between the ground and excited states can be characterised. The wavelength  $\lambda$  corresponds to the energy difference of these states,  $\Gamma$  (or  $\Delta\nu = 2\pi\Gamma$ ) gives their linewidth and  $\tau = 1/\Gamma$ . With this, the Doppler temperature and velocity and the recoil temperature and velocity may be calculated.

Transition	421nm	626nm
$\lambda$	421.291 nm	626.082 nm
$\Gamma$	$2.02 \times 10^8$	$0.85 \times 10^6$
$\tau$	4.94 ns	1.17 $\mu$ s
$\Delta\nu$	32.2 MHz	136 kHz
$I_{\text{sat}}$	56.3 mW/cm <sup>2</sup>	72 $\mu$ W/cm <sup>2</sup>
$T_{\text{Doppler}}$	773 $\mu$ K	3.3 $\mu$ K
$v_{\text{Doppler}}$	198 mm/s	12.9 mm/s
$T_{\text{recoil}}$	659 nK	298 nK
$v_{\text{recoil}}$	5.8 mm/s	3.9 mm/s

Table 2.2: Comparison of relevant atomic parameters for the 421 nm and 626 nm transitions, including the vacuum wavelength  $\lambda$ , transition rate  $\Gamma$ , lifetime  $\tau = 1/\Gamma$ , natural linewidth  $\Delta\nu = \Gamma/(2\pi)$ , saturation intensity  $I_{\text{sat}} = 2\pi^2\hbar c\Gamma/(3\lambda^3)$ , Doppler temperature  $T_{\text{Doppler}} = \hbar\Gamma/(2k_B)$ , Doppler velocity  $v_{\text{Doppler}} = \sqrt{\hbar\Gamma/(2m)}$ , recoil temperature  $T_{\text{recoil}} = (\hbar k)^2/(mk_B)$  and recoil velocity  $v_{\text{recoil}} = 2\pi\hbar/(\lambda m)$ , where  $\hbar$  is the reduced Planck constant,  $k = 2\pi/\lambda$  the wavenumber and  $m = 162.5$  a.u. the mean atomic mass of Dy. Table adapted, taken from [Mai15].

### 2.2.3 Hyperfine Structure

To include another subtle effect of the electronic energy levels, the nucleus has to be described a bit more precisely. So far the nucleus was assumed to be a point like electric monopole of infinite mass. In reality however, the nucleus definitely has a finite mass and it can exhibit an electromagnetic multipole moments of order  $2^k$  [BJ83a]. The finite (isotope-dependent) mass will only cause some small *isotope shifts* across all energy levels without changing the structure of the levels, while the different electric and magnetic multipole moments of the nucleus will cause an additional (small) splitting of the fine structure energy levels, giving rise to the so-called *hyperfine structure*.

It can be shown, that the nucleus can only exhibit electric multipole moments of even  $k$  (electric monopole, quadrupole...) while the magnetic multipole moments may only have orders of odd  $k$  (magnetic dipole, octapole ...). These multipole moments will only interact with non-circularly symmetric, partially filled sub-shells and as their range will roughly be proportional to  $1/r^{(k+1)}$  their contributions will become ever smaller with increasing  $k$ .

In the following (apart from the usual electric monopole) only the magnetic dipole and the electric quadrupole will be taken into account. This description will give rise to the hyperfine structure constants  $A_{HFS}$  &  $B_{HFS}$ .

It can also be shown [BJ83a], that a nucleus of nuclear spin  $I$  may only exhibit multipole moments of order  $2^n$ , where  $n \leq 2I$ . Thus, bosonic Dysprosium with a nuclear spin  $I = 0$  will not exhibit any hyperfine structure, as the nucleus can be accurately treated as an electric monopole. Fermionic Dysprosium with  $I = 5/2$ , however, will exhibit a hyperfine structure with significant consequences for trapping and cooling.

Similar to the spin-orbit coupling that was described above, the nuclear magnetic moment may couple to the total magnetic flux of the orbiting electrons, depending on their relative orientation.

The nuclear magnetic moment  $\mu_I$  may be written as:

$$\mu_I = g_I \mu_N I / \hbar \quad (2.28)$$

with nuclear magneton, comparing the electron mass  $m_e$  and the proton mass  $m_p$

$$\mu_N = \frac{m_e}{m_p} \mu_B \quad (2.29)$$

and where  $g_I$  is the *Landé factor* associated with the nuclear spin  $I$ . Often,  $\mu_I$  is given in units of the Bohr magneton  $\mu_B$  as:

$$\mu_I = g'_I \mu_B I / \hbar \quad (2.30)$$

with an adjusted Landé factor

$$g'_I = \frac{\mu_N}{\mu_B} g_I \quad (2.31)$$

As  $g'_I$  is very small, its contribution can typically be neglected.

Much more detail may be found in Bransden & Joachain's *Physics of Atoms and Molecules* ([BJ83a; BJ83b]), this description shall be limited however to the resulting energy splitting of the fine structure levels. Similar to the energy splitting found for the LS-Coupling (see Equation (2.25)) the energy splitting is given by:

$$\Delta E = \frac{A_{HFS}}{2} [F(F+1) - I(I+1) - J(J+1)] \quad (2.32)$$

where the constant  $A_{HFS}$  may best be determined experimentally via the *hyperfine interval law*  $\Delta E(F) - \Delta E(F-1) = A_{HFS}F$ .

Similarly, the electric quadrupole moment will give rise to another interaction with the magnetic moments of the orbiting electrons and causes a energy shift, deviating from the hyperfine interval law:

$$\Delta E = \frac{A_{HFS}}{2} K + \frac{B_{HFS}}{4} \frac{\frac{3}{2}K(K-1) - 2I(I+1)J(J+1)}{I(2I-1)J(2J-1)} \quad (2.33)$$

with

$$K = F(F+1) - I(I+1) - J(J+1) \quad (2.34)$$

The values of  $A_{HFS}$  and  $B_{HFS}$  for the ground state and the excited state of the 421nm transition for Dysprosium can be found in Table 2.1. Transition between hyperfine levels have to obey  $F' = F + \Delta F$  with  $\Delta F = 0, \pm 1$  and where  $F = 0 \rightarrow F' = 0$  is forbidden (see section 2.2.6). Each hyperfine level is  $F(F+1)$  times degenerate. For Dysprosium, the hyperfine levels have energy differences on the order of hundreds MHz (see Figure 2.1 (b), (c)).

## 2.2.4 Atoms in a Magnetic Field

So far, the hamiltonian of an atom was only described without the effects of any external fields. To include the effect of an external magnetic field on the hyperfine structure, another interaction term is introduced.

The interaction with a (constant) external magnetic field is described by the sum of the interaction of the electronic magnetic moment with magnetic field and the nuclear magnetic moment with the magnetic field. Taking the quantisation axis to be along the

z-axis we can write:

$$\hat{H}_{Zem} = \mu_e \mathbf{B} - \mu_I \mathbf{B} \quad (2.35)$$

$$= \frac{\mu_B}{\hbar} B_z (m_L + 2m_S) - g_I \frac{\mu_N}{\hbar} B_z m_I \quad (2.36)$$

where  $m_L, m_S, m_I$  are the projections of  $\mathbf{L}, \mathbf{S}, \mathbf{I}$  along the quantisation axis and  $g_I$  is the Landé factor associated with the nuclear spin. This interaction will lift the degeneracy of the hyperfine states.

## Weak Magnetic Field

In the case of a weak magnetic field the energy correction due to  $\hat{H}$  can be treated as a small perturbation to the hyperfine Hamiltonian. Then the corresponding energy shift to the hyperfine sublevels will be given by:

$$\Delta E = g_F \mu_B |\mathbf{B}| m_F \quad (2.37)$$

where the direction of the z-axis was arbitrarily chosen along the magnetic field direction and with:

$$g_F = g_J \frac{F(F+1) + J(J+1) - I(I+1)}{2F(F+1)} - g_I' \frac{F(F+1) - J(J+1) + I(I+1)}{2F(F+1)} \quad (2.38)$$

and

$$g_J = 1 + \frac{J(J+1) + S(S+1) - L(L+1)}{2J(J+1)} \quad (2.39)$$

This value of  $g_J$  is only a first approximation however. Including the Schwinger correction, that gives an accurate value of the gyromagnetic ratio of the electron, a correction for non-perfect LS-coupling, a correction for relativistic kinetic energies and diamagnetic correction depending on the charge density of the inner electrons, for the ground state of Dy a theoretical value of

$$g_J^{theo} = 1.2370 \quad (2.40)$$

is determined [JL61].

Experimentally the values

$$g_J^{161} = 1.2415870(10) \quad (2.41)$$

$$g_J^{164} = 1.2415867(10) \quad (2.42)$$

are obtained for the ground states of  $^{163}\text{Dy}$  and  $^{164}\text{Dy}$  [FDG74].

## Strong Magnetic Field

For strong magnetic fields, the energy due to the interaction with the magnetic field will be much larger than that of the hyperfine states. The hyperfine structure will then be treated as a perturbation to the magnetic field interaction and the splitting will rather be given by

$$\Delta E = (m_J g_J - m_I g_I) \mu_B |\mathbf{B}| \quad (2.43)$$

where the contribution of the total angular momentum is much larger than that of the nuclear spin, as  $g_I \ll g_J$ . At very large fields, the eigenstates will regroup according to their  $m_J$  values. This gradual transition between the weak and strong field regime can be seen in Figure 2.3. There both in the weak and strong field regime the Zeeman effect is linear in  $|\mathbf{B}|$ . The strength of the Zeeman Hamiltonian at magnetic fields around a few hundred Gauss will become comparable or larger than that of the hyperfine Hamiltonian  $\hat{H}_{HFS}$ , which means that treating  $\hat{H}_{Zem}$  as a perturbation to  $\hat{H}_{HFS}$  is no longer possible and  $|F m_F\rangle$  will no longer be a good basis.

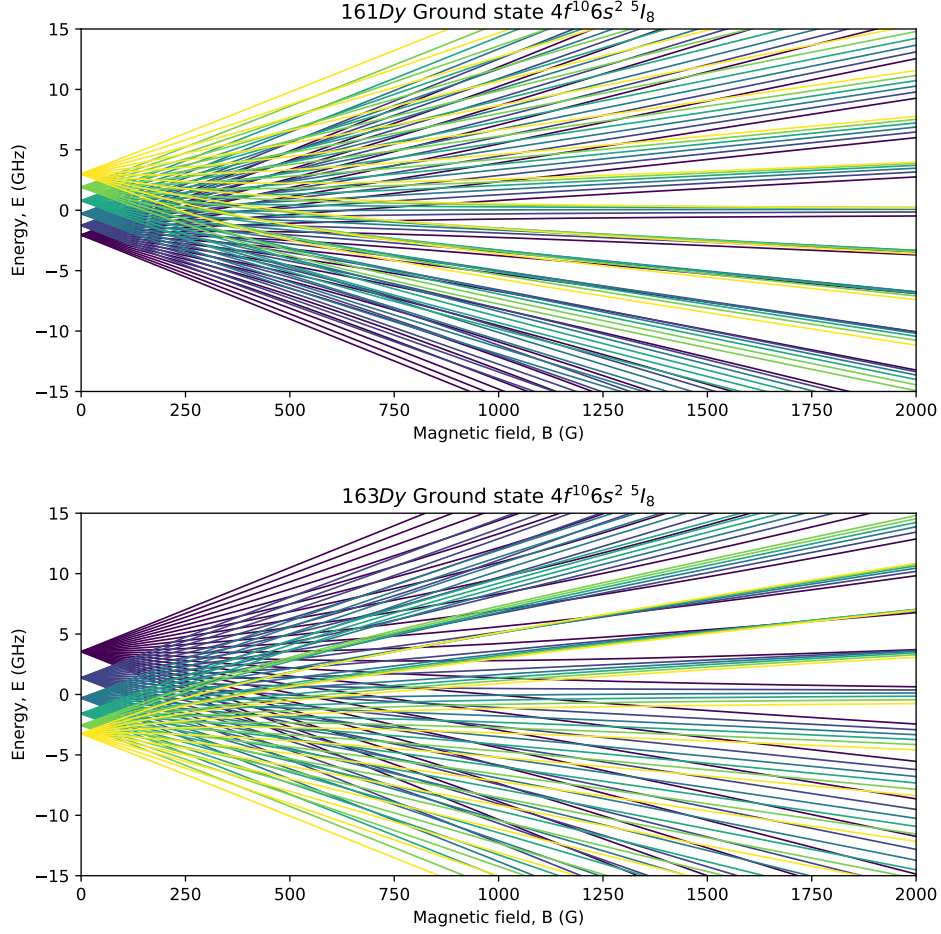


Figure 2.3: Energies of the hyperfine states of the ground states of  $^{161}\text{Dy}$  (top) and  $^{163}\text{Dy}$  (bottom). At zero magnetic field, the hyperfine manifolds (from  $F = 21/2$  in purple to  $F = 11/2$  in yellow) are degenerate. At small fields, the approximately linear Zeeman effect lifts the degeneracy. At large fields, in the Paschen-Back regime the energy is again approximately linear with the field. However, because  $g_I \ll g_J$  the eigenstates begin to regroup into 17 manifolds of 6 nearly degenerate states, according to the 17 possible values of  $m_J$  for  $J = 8$  while the contribution of  $m_I$  is only a small perturbation.

### 2.2.5 Light-Atom Interactions

Following [Foo05b; CDG98], to describe the interaction of an atom with light, we will consider a toy model of an atom with only two states  $|a\rangle$  and  $|b\rangle$ , separated by the energy  $\hbar\omega$ , with a rate of spontaneous emission  $\Gamma$ . We will consider monochromatic light, described by the field

$$\mathbf{E}(\mathbf{r}, t) = \varepsilon E_0 \cos(\omega_L t + \phi(\mathbf{r})) \quad (2.44)$$

As the number of photons emitted from the atom into the field will be small compared to the number of photons in the field itself, we can assume any back-action of the atom on the field to be negligible. Also, as the distance between an electron and the nucleus will be much smaller than the wavelengths used in this theses, the field will be assumed

to be constant over the extend of the atoms and the dipole approximation becomes valid.

The Hamiltonian  $\hat{H}$  can then be a term describing the center of mass motion  $\mathbf{p}^2/2m$ , a term describing the internal electronic structure of the atom  $\hat{H}_{int}$  as described above and a time dependent part  $\mathbf{dE}(\mathbf{r}, t)$  describing the interaction with the field:

$$\hat{H} = \frac{\mathbf{p}^2}{2m} + \hat{H}_{ab} + \mathbf{dE} \quad (2.45)$$

The equations of motion for the position  $\mathbf{R}$  and momentum  $\mathbf{p}$  operator of the atom are then given by the Heisenberg equations as [CDG98]:

$$\dot{\mathbf{R}} = \frac{\partial \hat{H}}{\partial \mathbf{p}} = \frac{\mathbf{p}}{m} \quad (2.46)$$

$$\dot{\mathbf{p}} = m\ddot{\mathbf{R}} = -\frac{\partial \hat{H}}{\partial \mathbf{R}} = \sum_{i=x,y,z} d_i \nabla_{\mathbf{R}} E_i(\mathbf{R}, t) \quad (2.47)$$

To describe the motion of the center of mass  $\mathbf{r}_C = \langle \mathbf{R} \rangle$ , we will take the average of this equation:

$$m\ddot{\mathbf{r}}_C = \sum_{i=x,y,z} \langle d_i \rangle \nabla_{\mathbf{R}} E_i(\mathbf{R}, t) \quad (2.48)$$

$$= \sum_{i=x,y,z} \langle d_i \rangle \varepsilon_i [\cos(\omega_L t) \nabla E_0 - \sin(\omega_L t) E_0 \nabla \phi] \quad (2.49)$$

The two terms in the above equation will lead to reactive force, proportional to the gradient of the amplitude of the field and and a dissipative force, proportional to the phase gradient of the field.

The average of the dipole operator can be found to be [CDG98]:

$$\langle d_i \rangle = 2 \langle a | \mathbf{d} | b \rangle_i (u_{st} \cos(\omega_L t) - v_{st} \sin(\omega_L t)) \quad (2.50)$$

where  $u_{st}$  and  $v_{st}$  are the steady state solutions to the Bloch equations given by

$$u_{st} = \frac{\Omega}{2} \frac{\delta}{\delta^2 + (\Gamma^2/4) + (\Omega^2/2)} \quad (2.51)$$

$$v_{st} = \frac{\Omega}{2} \frac{\Gamma/2}{\delta^2 + (\Gamma^2/4) + (\Omega^2/2)} \quad (2.52)$$

where  $\Omega = E_0 \langle a | \mathbf{d} | b \rangle / \hbar$  is the Rabi frequency and  $\Delta = \omega_L - \omega$  is the detuning of the light to the atomic transition.

For a plane wave  $\phi(\mathbf{r}) = \mathbf{k}\mathbf{r}$  and so, by averaging over on period of the light field the two following forces are obtained [CDG98]. The radiative pressure, proportional to the



phase gradient:

$$\mathbf{F}_{sc} = \hbar \mathbf{k} \frac{\Gamma}{2} \frac{\Omega^2}{\Omega^2 + \Gamma^2/2 + 2\Delta^2} \quad (2.53)$$

As  $\Omega^2$  is proportional to intensity, the force will be proportional to intensity at low intensities but it will saturate to the value  $\hbar \mathbf{k} \Gamma/2$  at large intensity.

The second force is the dipole force, proportional to the gradient of the field amplitude is given by:

$$\mathbf{F}_{dip} = -\hbar \frac{\delta}{8} \frac{\nabla(\Omega^2)}{\Omega^2 + \Gamma^2/2 + 2\Delta^2} \quad (2.54)$$

This force acts along the gradient of the intensity, while the sign of the detuning determines whether the force will be directed to the intensity maximum or minimum. In contrast to the radiation pressure its magnitude may increase with intensity without saturating.

## 2.2.6 Clebsch-Gordan Coefficients and Wigner Symbols

Finally, some subtleties in the coupling of photons to atoms have to be discussed. The relative angle between the angular momenta of a photon and the electronic states (indicated by the  $m_F, m'_F$  quantum numbers in the case of hyperfine splitting) gives rise to certain weights being associated with certain transitions. Here a brief overview on the correct handling of transitions between angular momentum states will be given where the weights of different possible transitions and the selection rules of dipolar transitions will be found.

We can describe a transition probability between two states  $|F m_F\rangle$  and  $|F' m'_F\rangle$  induced by an electric dipole operator  $\mathbf{d}$  as the electric dipole cross-section:

$$\langle F' m'_F | d_q | F m_F \rangle \quad (2.55)$$

where  $d_q$  is the projection of the dipole operator along spherical coordinates  $e_+$ ,  $e_-$ ,  $e_z$  which relate to the Cartesian coordinates as:

$$e_{\pm} = \frac{1}{\sqrt{2}}(e_x \pm i e_y) \quad \& \quad e_z = e_z \quad (2.56)$$

Remember that the dipole operator  $\mathbf{d} = e\mathbf{r}$  only acts on the relative position between electron and nucleus. The dipole operator therefore does not act on the spin of electron or nucleus. As the total atomic angular momentum  $\mathbf{F} = \mathbf{J} + \mathbf{I} = (\mathbf{L} + \mathbf{S}) + \mathbf{I}$  is composed of both spin angular momenta and orbital angular momenta, the dipole operator will only affect ‘a part of’  $\mathbf{F}$ . That means that the dipole operator will not affect these parts of the atomic states, which means that they can be factored out of the equation.

An excellent discussion of this process can be found in the lecture notes of D.A. Steck

[Ste07], especially in chapters 7.3.4-7.3.7<sup>1</sup>. The key points of which will be summarised here. For convenience the projection  $m_j$  of an angular momentum  $j$  will be written as  $m$ .

Let us look at the action of a tensor operator of rank  $k$  on an angular momentum state

$$\mathbf{T}_q^{(k)} |\alpha' j' m'\rangle \quad (2.57)$$

where  $\alpha'$  represents all (radial) quantum numbers that do not interact with the angular momentum operator. It can be found that the action of that angular momentum operator looks just like the mixing of two angular momenta. This gives rise to the *Wigner-Eckart theorem*:

$$\langle \alpha j m | T_q^{(k)} | \alpha' j' m' \rangle = (-1)^{2k} \langle \alpha j | \mathbf{T}^{(k)} | \alpha' j' \rangle \langle j m | j' m'; k q \rangle \quad (2.58)$$

Equation (2.58) splits the interaction with the angular momentum operator into a orientation independent *reduced matrix element*  $\langle \alpha j | \mathbf{T}^{(k)} | \alpha' j' \rangle$  which is just a scalar and an orientation dependent part which is the *Clebsch-Gordan Coefficient*  $\langle j m | j' m'; k q \rangle$ . These can be calculated explicitly (using [Tea25] for example) or can be found in look-up tables [con25].

Explicitly in the case of the dipole operator  $\mathbf{d} = e\mathbf{r}$  (which is of rank  $k = 1$ ) and the hyperfine state  $|F m_F\rangle$  (omitting the radial part) the Wigner-Eckart theorem can be written explicitly as:

$$\langle F' m_{F'} | d_q | F m_F \rangle = \langle F' || \mathbf{d} || F \rangle \langle F m_F | F' m_{F'}; 1q \rangle \quad (2.59)$$

Further, it can be found that for an operator, that acts only on a part  $\mathbf{J}_1$  of a composite angular momentum state  $\mathbf{J} = \mathbf{J}_1 + \mathbf{J}_2$  the reduced matrix element is given by:

$$\langle j || \mathbf{T}^{(k)} || j' \rangle = \delta_{j_2 j'_2} (-1)^{j' + j_1 + k + j_2} \sqrt{(2j' + 1)(2j_1 + 1)} \begin{Bmatrix} j_1 & j'_1 & k \\ j' & j & j_2 \end{Bmatrix} \langle j_1 || \mathbf{T}^{(k)} || j'_1 \rangle \quad (2.60)$$

That means the reduced matrix element for the composite angular momentum can be further reduced into a reduced matrix element for the interacting angular momentum  $\mathbf{J}_1$  and a Wigner-6j symbol (in curly brackets). This Wigner-6j symbol again is just a scalar that can readily be computed (by use of [Tea25] for example). Now one should remember that the dipole operator  $\mathbf{d} = e\mathbf{r}$  only acts on the relative position of electron and nucleus, but not on any spin angular momenta.

Thus finally by combining equations 2.58 & 2.60 the transition between two hyperfine states, induced by the dipole operator  $\mathbf{d}$  can be decomposed as follows:

$$\langle F' m_{F'} | d_q | F m_F \rangle = \langle F' || \mathbf{d} || F \rangle \langle F m_F | F' m_{F'}; 1q \rangle \quad (2.61)$$

---

<sup>1</sup>As these lecture notes are presumably work in progress, the chapter numbers might change. The entire chapter 7 on *Atomic Angular-Momentum Structure* is worth reading. Here however, especially the subchapter on the *Wigner-Eckart Theorem* to the *Application to Atomic Transitions* are useful.

where  $1q$  corresponds to the photon of angular momentum 1 and its projection  $q$ , that drives the transition. The angular dependence is then absorbed by a Clebsch-Gordan coefficient. The reduced matrix element still consists on  $F$  however, which needs to be decomposed into the total electronic angular momentum  $\mathbf{J}$  and the nuclear spin  $\mathbf{I}$ , giving rise to a Wigner 6j symbol:

$$\langle F' \| \mathbf{d} \| F \rangle \equiv \langle J I F' \| \mathbf{d} \| J' I F \rangle \quad (2.62)$$

$$= \langle J \| \mathbf{d} \| J' \rangle (-1)^{F'+J+1+I} \sqrt{(2F'+1)(2J+1)} \begin{Bmatrix} J & J' & 1 \\ F' & F & I \end{Bmatrix} \quad (2.63)$$

To find  $\langle J \| \mathbf{d} \| J' \rangle$  a further decomposition of  $\mathbf{J} = \mathbf{L} + \mathbf{S}$  may be done in the same way. This finally ends in the reduced matrix element  $\langle L \| \mathbf{d} \| L' \rangle$  which can be calculated via the analytical solutions for the orbitals  $u_{nlm_l}(\mathbf{r})$ . (For complex atoms like the lanthanides, this can of course become quite an involved affair.)

However, one can also recognise, that:

$$\Gamma_{J_g J_e} = \frac{\omega_0^3}{3\pi\epsilon_0\hbar c^3} \cdot \frac{2J_g + 1}{2J_e + 1} |\langle J_g \| \mathbf{d} \| J_e \rangle|^2 \quad (2.64)$$

which means that the reduced matrix element  $\langle J \| \mathbf{d} \| J' \rangle$  is proportional to the decay rate (or linewidth) which is readily available in experiment to great precision. To understand the general effect of the Wigner 6J symbols, as an example Table 2.3 gives the Wigner 6j symbol values for  $J = 1/2$  with  $S = 1/2$  and  $L = 0$  to states of  $L' = 0, 1, \dots$  with  $S' = 1/2$  and  $J' = 1/2, 1/2, 3/2, \dots$ <sup>2</sup>. This could represent a single photon transition from a  $^3S_{1/2}$  state to some other state. For Dy, a similar table is given in Section 5.2.

$L_p$	$J_p$	Wigner 6-j
0	0.5	0.000000
1	0.5	0.408248
1	1.5	-0.408248
2	0.5	0.000000
2	1.5	0.000000
2	2.5	0.000000
$\vdots$	$\vdots$	$\vdots$

Table 2.3: Values of Wigner 6-j symbols for  $L = 0$ ,  $J = L + S = 1/2$  and given  $L'$  and  $J'$

The Wigner-6j symbols thus just compute how different angular momenta can be added together. From a conservation of angular momenta point of view it is clear that an electron in an S-shell ( $L = 0$ ) can be transferred (in a single photon process) only to a P-shell with  $L' = 1$ . For the two possible combination of  $\mathbf{J} = \mathbf{L} + \mathbf{S}$  the Wigner-6j symbols

<sup>2</sup> $J = 1/2$  is mentioned twice deliberately, as there is two different ways for  $J = L + S$  to add to  $1/2$ .

gives a certain ‘weight’. These are the only allowed transitions. All other processes aren’t allowed due to conservation of angular momentum and the Wigner-6j symbol is 0.

And finally to clarify the influence of the Clebsch-Gordan coefficients, a similar example will be given. As the Clebsch-Gordan coefficients capture the angular dependence of the process, the Clebsch-Gordan coefficients will be given here for a transition of  $|J; L S\rangle = |\frac{1}{2}; 0 \frac{1}{2}\rangle$  to  $|J'; L' S'\rangle = |\frac{3}{2}; 1 \frac{1}{2}\rangle$  will be given. There are different possibilities of the light to couple the atomic state resulting in different possible  $m_J$  and  $m'_J$ . Which values of  $\Delta m_J = m'_J - m_J$  are allowed is given by projection of the photon angular momentum on the quantisation axis  $q = 0, \pm 1$ , which depends on the polarisation of the light. The resulting Clebsch-Gordan coefficients for this process are given in Table 2.4. Again, for values of  $m'_J$  that are impossible due to conservation of angular momenta, the

$m$	$q$	$m'$	CGC
-1/2	-1	-3/2	1.000000
-1/2	0	-1/2	0.816497
-1/2	1	1/2	0.577350
1/2	-1	-1/2	0.577350
1/2	0	1/2	0.816497
1/2	1	3/2	1.000000

Table 2.4: Clebsch–Gordan coefficients (CGC) for the given  $(m, q) \rightarrow m'$  combinations for  $J = 1/2$ ,  $J' = 3/2$ .

Clebsch-Gordan coefficients are zero. However for those, that are allowed, we can clearly see that not all  $m_J \rightarrow m'_J$  are created equal. Finally the scattering rate for a certain process will depend the square of these Clebsch-Gordan coefficients, so there might be a large scattering rate between different transitions.

In summary, we retrieve the expected selection rules for single photon transitions of  $F' = F \pm 1$  except  $F' = F = 0$  and  $m'_F = m_F \pm 1$  while  $S' = S$  and  $I' = I$ .

## 2.3 Optical Trapping of Dysprosium Atoms

### 2.3.1 Optical Molasses

From the radiative pressure given in Equation (2.53) we can see that a near resonant laser causes a force on an atom, increasing with intensity and decreasing with detuning. With this, a first step into laser-cooling and trapping can be made: An atom moving with a velocity  $\mathbf{v}$  along some direction in a laser beam of wavevector  $\mathbf{k}$  will experience

the frequency of the light shifted by a *Doppler Shift*:

$$\Delta_{Dop} = -\frac{\mathbf{k}\mathbf{v}}{2\pi} \quad (2.65)$$

If the laser light has some detuning  $\Delta_L$  (as defined above Equation (3.5)), the effective detuning seen by the atoms will be  $\Delta_L + \Delta_{Dop}$  such the force of the laser acting on the atoms will be largest at some velocity of the atom where the effective detuning is smallest.

By using two counter-propagating beams that will be oppositely Doppler detuned, each with some small negative detuning  $\Delta_L$  an atom within the light field will experience a velocity-dependent force from both beams. Due to the effective detuning, the force from the beam propagating against the atomic motion will be larger and the velocity component of the atom along the light propagation direction will be reduced.

By plotting the scattering force (Equation (2.53)) of two counter-propagating beams in Figure 2.4, where the force is given in units of  $[\hbar k\Gamma]$ , we can see that the net force  $F_{net} = F_1 + F_2$  causes any atom to be decelerated towards  $\mathbf{v}\mathbf{k} = 0$ .

Most clearly this effect can be seen by approximating the net force for small velocities via Taylor expansion as:

$$\mathbf{F}_{approx} = \mathbf{v} \frac{\mathbf{k}}{k} 8\hbar k^2 \frac{s\Delta/\Gamma}{(1 + s + (2\Delta/\Gamma)^2)^2} \quad (2.66)$$

If the detuning is negative, this term will be negative for positive velocities and vice versa, thus acting like a force of friction. Upon closer inspection it can be seen however, that the degree to which the atoms can be slowed is limited. As the method relies on random, spontaneous scattering the lowest temperature that can be achieved with a (standard) optical molasses for a two-level atoms is the *Doppler Temperature* [GWO99]:

$$T_D = \frac{\hbar\Gamma}{2k_B} \quad (2.67)$$

### 2.3.2 Zeeman Slowers

Another way to compensate a detuning  $\Delta_L$  is by inducing a detuning through a Zeeman shift. For small magnetic fields, this detuning between two hyperfine states  $|g\rangle$  and  $|e\rangle$  will take the form (see Section 2.2.4)

$$\Delta_{Zem} = \frac{\mu_B |\mathbf{B}|}{\hbar} (g_F^e m_F^e - g_F^g m_F^g) \quad (2.68)$$

This detuning is typically exploited to slow down an atomic jet exiting an oven with a large range of velocities, by using a *Zeeman Slower*. As the velocities within a thermal atomic jet will be Boltzmann distributed, just using a counter-propagating beam at a fixed

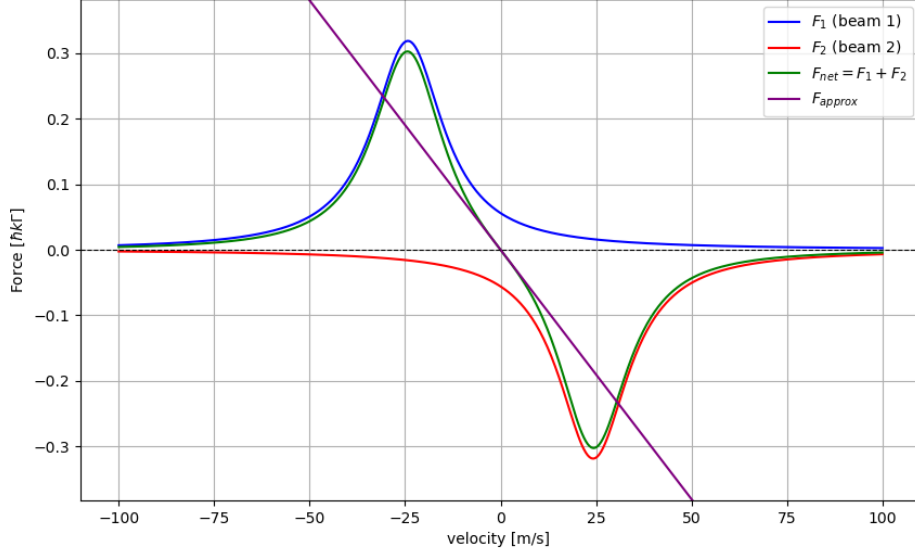


Figure 2.4: Optical Molasses: Two counter-propagating beam causing a ‘friction’ force

detuning would not be very effective. As the atoms are slowed the apparent detuning would change due to the Doppler effect and so would the force they experience.

However by applying a magnetic field gradient along the axis of propagation, atoms of a much larger range of velocities can be slowed down to a certain exit velocity. By having a large Zeeman detuning  $\Delta_{Zem}$  at the beginning of a Zeeman slower, only atoms with a large velocity for which  $\Delta_{Dop}(|\mathbf{v}|) + \Delta_{Zem}(|\mathbf{B}|) + \Delta_L = 0$  will be resonant and decelerated. Atoms of with a slower velocity will, at the entrance of the Zeeman slower, be more or less unaffected. The width of the affected velocity range will be more or less given by the linewidth of the transition  $\Gamma$  (see Equation (2.53)). The atoms that where slowed early on, will remain resonant with the light as the magnetic field and thus  $\Delta_{Zem}$  decreases while atoms of slower velocities will join the process later on. Finally, the Zeeman slower has to be terminated before the atoms are reflected by the slowing beam. This can be done by limiting the magnetic field gradient in the end such that  $\Delta_{Dop}(|\mathbf{v}| = 0) + \Delta_{Zem}(|\mathbf{B}|) + \Delta_L \neq 0$  everywhere in the Zeeman slower.

### 2.3.3 Magneto Optical Traps

While the Zeeman slower and the optical molasses may respectively slow and cool atoms down they do not confine them in space. To get confinement the effect of a optical Molasses can be combined with a magnetic field gradient. To see the working principle of a magneto-optical-trap (MOT) this description will focus on the confinement in one spatial direction.

By applying two counter-propagating beams with some detuning together with a mag-

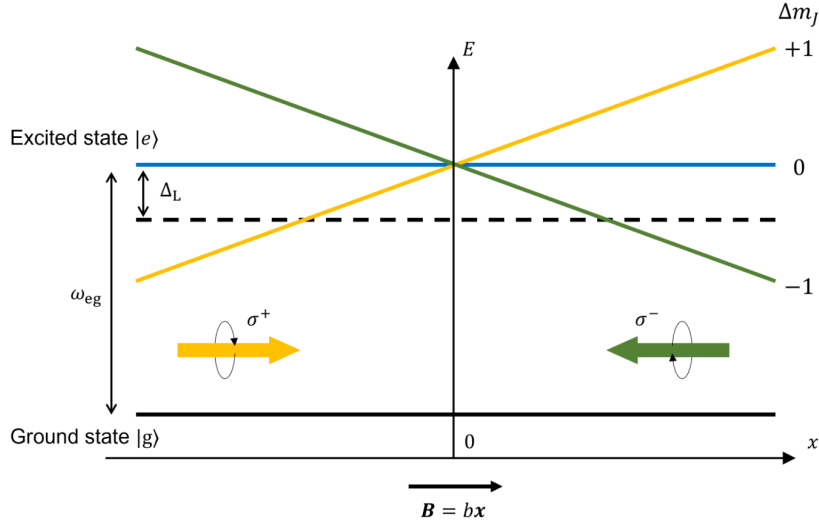


Figure 2.5: Space dependent detuning of Zeeman sublevels in a MOT. Figure taken from [Gao22]

netic field gradient, we can trap atoms at the position of zero magnetic field. Schematically this is shown in Figure 2.5.

If an atom is displaced by some distance  $x$  from the centre of the MOT, it will acquire a Zeeman shift  $\Delta_{Zem}(x)$  which will make it stronger detuned from one beam and less detuned to the other. By choosing the detuning of the beams to be negative (red-detuned) the scattering force of the atom will experience a restoring force towards the centre of the MOT.

Some care has to be taken to the polarisations of the counter-propagating beams. Here different conventions for the quantisation axis can be used. Two common conventions exist: One may keep the quantisation axis either 1) along some fixed axis or 2) along the local magnetic field direction. These two conventions will decide how the  $m_F$  sublevels are labelled. In Figure 2.5 the first convention is used. In this case on one side of the MOT the  $\Delta m_F = -1$  transition has lower energy, while on the other side the  $\Delta m_F = +1$  transition has lower energy. Thus the polarisations of the beams have to be chosen such, that the beam which is resonant with ‘the  $m_F = +1$  side’ of the MOT drives a  $\sigma^+$  transition and vice versa.

Then, atoms that are displaced from the centre of the MOT will experience a force that accelerates them back towards the centre of the MOT. The atoms may also have some velocity. As long as the Doppler shift of this velocity is not too large and can be compensated by the laser and Zeeman detuning, the atoms may be trapped in the MOT.

Here in the DyLab, a first 2DMOT for Dysprosium, that traps atoms from a hot atomic jet without the need for a Zeeman slower, was introduced [Jin+23]. A simulation of this 2DMOT can be seen in Figure 2.6.

One can clearly see two regions of de- and accelerations, that correspond to the two

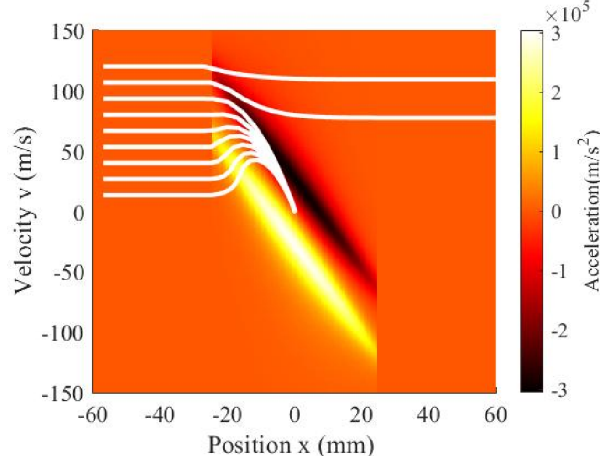


Figure 2.6: Simulation of the trajectories of  $^{164}\text{Dy}$  atoms through the phase space of the DyLab 2DMOT. A capture velocity of around  $100 \frac{\text{m}}{\text{s}}$  can be seen. Figure taken from [Gao22].

counter-propagating beams<sup>3</sup> in Figure 2.5. If the magnitude of the magnetic field gradient gives the slope of these two regions in the plot, while the laser detuning  $\Delta_L$  sets the spacing between the two regions. One can clearly see that atoms with velocities of up to  $100 \frac{\text{m}}{\text{s}}$  are trapped in this 2DMOT.

By choosing one, two or three pairs of counter-propagating beams, the atoms can be confined in one two or three dimensions respectively. To be able to generate a magnetic field gradient in all three spatial directions, coils in anti-Helmholtz configuration can be used. These generate a quadrupole magnetic that has a gradient in all three directions. The temperature that can be reached in a MOT is again fundamentally limited by the Doppler temperature defined in Equation (2.67).

### 2.3.4 Optical Dipole Traps

Another option for spatially confining atoms is an optical dipole trap (ODT). By exploiting the dipole force of Equation (2.54) one can trap atoms as well. By choosing the detuning of the light to be negative ('red detuned') or positive ('blue detuned') one can choose whether the atoms experience a force towards to or away from the intensity maximum.

In the case of a red detuned ODT atoms will 'simply' accumulate in the focus of a laser beam. The detuning  $\Delta$  of the beam has to be chosen large enough, that the scattering force of Equation (2.53) scaling with  $1/\Delta^2$  is smaller than the dipole force of Equation (2.54), scaling with  $1/\Delta$ . In general, this force will be quite small and an ODT will have to be loaded with already quite cold atoms[GWO99] (typically from a

<sup>3</sup>The situation is actually a bit more complicated as this 2DMOT consists of four pair-wise counter-propagating beams that are at an angle of  $45^\circ$  to the atomic jet. For a full description see [Gao22; Jin+23].



3DMOT). However, with an ODT it is possible to reach even lower temperatures than in a MOT. By choosing the trapping force (dynamically) such that the atoms with the largest velocity can escape the trap, the mean velocity in the trap will go down as long as long as the velocity of the atoms within the trap is redistributed among the remaining atoms as they scatter with each other. This continuous elimination of the ‘hot’ tail of the velocity distribution can cool the atoms down to degeneracy and is called *evaporative cooling*.

Dipole traps can come in a varied of shapes and forms including crossed dipole traps [GWO99], optical tweezers & tweezer arrays [Ash70; Blo+23] and static & dynamic optical lattices [Blo05; Wil+08].

# Chapter 3

## Imaging Ultracold Quantum Gases

### 3.1 Imaging Optics

The primary method of measurement in ultracold quantum gas experiments is imaging the ultracold gas with light. From these measurements the density distribution real and momentum space, the overall number of atoms, the temperature and more can be deduced. As the atomic clouds are typically small (few micrometers), fragile (destroyed by a single flash of resonant light for absorption imaging) and inside a vacuum (causing long working distances) imaging can present some difficulties and interesting challenges.

Many experiments use absorption imaging after time of flight (TOF) to measure the momentum distribution of the atoms [You+10; Wen15; Soh+21; Jin+23]. This method is relatively easy to implement, robust and the expansion of the atoms may facilitate the imaging process. The increase in size reduces the need for diffraction limited optics while a reduction of the density during expansion can limit the optical density and enable low intensity absorption imaging.

However, for imaging the density of an atomic sample in-situ, one might have to deal with structures less than a micron in size and with very large densities. This requires both the use of a microscope near the diffraction limit and an imaging scheme that can deal with very large optical densities. Different established imaging scheme will be described in section 3.2. Their analysis and comparison leads to a choice of imaging schemes for the vertical in-situ imaging arm of the BoDy experiment. A high intensity absorption imaging scheme was implemented (Section 3.2.1) while a new design of a phase contrast imaging scheme is described in Section 4.5.

To be able to describe the working principles of different imaging schemes some optics need to be introduced. While many different formalism may be used that simplify the propagation of and interaction with light in various ways, here we will assume light to be a monochromatic (typically plane) wave described by a scalar field, that may pick up a phase and change its amplitude while transmitting through optical media.

When simulating the propagation of a complex light field through an imaging system, Fourier Optics will prove to be most useful. Below, some important concepts of both these formalisms will be introduced.

### 3.1.1 Light Field Propagation through Optical Media

An atomic gas may be considered as a resonant dielectric medium of density  $n(\mathbf{r})$ . While propagating through this medium light will pick up a phase, depending on the refractive index of the gas.

Following the notation of [Soh21], light at some position  $\mathbf{r}$  and time  $t$  inside a dielectric medium may be described as an electromagnetic wave

$$E(\mathbf{r}, t) = E_0 \exp[i(\mathbf{k}'\mathbf{r} - \omega t)] = E_0 \exp[i(\mathbf{k}\mathbf{r} - \omega t)] \exp[i\beta(\mathbf{r})] \quad (3.1)$$

where  $E_0$  is the amplitude of the field,  $\mathbf{k}$  is the wave vector in vacuum,  $\mathbf{k}' = \mathbf{k} + i\beta$  is the wavevector in the medium and  $\omega$  is the frequency of the (monochromatic) light.

Inside a dielectric with complex refractive index

$$n_c = n_r + in_i \quad (3.2)$$

the complex phase

$$\beta = \varphi + \frac{i}{2}\epsilon \quad \text{with} \quad \varphi = (n_r - 1)\mathbf{k}\mathbf{r} \quad \text{and} \quad \epsilon = 2n_i\mathbf{k}\mathbf{r} \quad (3.3)$$

modifies the field propagation.  $\varphi$  is connected to the conventional real refractive index  $n_r$  and is called the *dispersive phase*. The imaginary part  $\epsilon$ , connected to the imaginary part of the refractive index  $n_i$ , which relates to the absorption coefficient and is called *optical depth* (OD) of the medium.

The intensity of this field is given by

$$I(\mathbf{r}, t) = |E(\mathbf{r}, t)|^2 = I_0 e^{-\epsilon} \quad (3.4)$$

where the optical depth causes a reduction of intensity.

For a light field, interacting with an atomic cloud of density  $n(x, y, z)$ , the dispersive phase and the optical density can be connected to the polarisability of the atoms  $\alpha(\omega)$ . An atom, with discrete internal levels, that correspond to possible resonant excitations through light coupling, may here be approximated as a two level system. Within this approximation a ground state and an excited state exist, that are connected via a transition of frequency  $\omega_0$  and linewidth  $\Gamma$ . For light with intensity  $I = s \cdot I_{sat}$  with a detuning  $\Delta = \omega_L - \omega_0$ , the complex phase  $\beta$  can be connected to the polarisability  $\alpha$  under the

rotating wave approximation as follows:

$$\varphi(\mathbf{r}, s, \Delta) = -\sigma_0 \bar{n}_z(x, y) \frac{\Gamma \Delta}{4\Delta^2 + \Gamma^2(1 + s)} \propto \mathcal{R}\{\alpha\} \quad (3.5)$$

$$\epsilon(\mathbf{r}, s, \Delta) = +\sigma_0 \bar{n}_z(x, y) \frac{\Gamma^2}{4\Delta^2 + \Gamma^2(1 + s)} \propto \mathcal{I}\{\alpha\} \quad (3.6)$$

Here, it was assumed, that the light is propagating in  $z$ -direction and traverses the column density

$$\bar{n}_z = \int_0^z n(x, y, z') dz' \quad (3.7)$$

The transition is characterised by a scattering cross section

$$\sigma_0 = \frac{6\pi c^2}{\omega^2} \quad (3.8)$$

and a saturation intensity given by:

$$I_{sat} = \frac{\hbar \Gamma \omega_0^3}{12\pi c^2} \quad (3.9)$$

In this thesis the factor  $\sigma_0 \bar{n}_z(x, y)$  may be called the *bare OD*, as it is the optical depth for resonant light without saturation effects. It will be often referenced as it is directly connected to the atomic density and therefore often a quantity of interest. The phase  $\epsilon$  will just be called the OD as it is the phase that the light *actually* acquires as it propagates through the cloud. Thus it is the only quantity that is actually accessible to the (resonant) light.

From Equation (3.4) it can be seen that keeping the OD between  $\epsilon = 0.1$  and  $\epsilon = 4.6$  (after transmission through the full atomic cloud) the intensity will be reduced between 10% and 90%. By increasing  $\Delta$  and  $s$  the OD can be adjusted to a favourable value. To be able to extract the atomic density from an intensity measurement we will typically try to make either  $\varphi$  or  $\epsilon$  small compared to the other. We will thus either increase work on resonance where  $\varphi(\Delta = 0) = 0$  and increase  $s$  (see Section 3.2.1 or we will increase  $\Delta$  large enough until  $\epsilon \ll \varphi$  and map  $\varphi$  onto the intensity via an interference effect (Section 3.2.2). In both cases  $\Delta$  and  $s$  will be adjusted to keep the intensity in a usable range for a given atomic density.

### 3.1.2 Fourier Optics

After light acquires some space-dependent phase in a (thin) optical element or atomic cloud, it is essential to understand how it will propagate through free space, to know how and where to collect an image of the object in question.

In the context of this thesis, this propagation is well described by Fourier Optics. As

demonstrated by Jean-Baptiste Fourier, any periodic functions can be split into a sum of sinusoids. That means, one may split a periodic function into its frequency components and reconstruct the original function by summing these frequency components, scaled by appropriate weights.

This technique can be extended to a finite sequence of samples, that represents a function, via the Discrete Fourier Transform (DFT). This step is invaluable to computational and experimental physics, as one will only ever be able to measure discretised sequences of finite length.

The Fourier decomposition can readily be applied to the propagation of light and will be briefly explained here. It is important however, that while we will be discussing a decomposition of different frequency components, we will be talking about *spatial frequencies*  $\nu_x$  in the following. The following discussion is limited to a monochromatic beam of light with angular frequency  $\omega$ . To avoid confusion between the temporal frequency  $\nu = c/\lambda$ , the angular frequency  $\omega = 2\pi\nu$  will be used for temporal frequencies, while  $\nu_x, \nu_y, \nu_z$  will be used for spatial frequencies. Due to the linearity of the *Helmholtz equation*, light with a broad spectrum may be treated as a linear combination of monochromatic components.

A one-dimensional function  $f(x)$  may be decomposed as an integral of weighted spatial frequency components as follows:

$$f(x) = \int_{-\infty}^{+\infty} \mathcal{F}(\nu_x) \exp[-i 2\pi \nu_x x] d\nu_x \quad (3.10)$$

This is called the *inverse Fourier transform*. The ‘frequency components’ are the harmonic functions  $\exp(i 2\pi \nu x)$  of spatial frequency  $\nu$  at position  $x$  and they are weighted by the complex amplitudes  $\mathcal{F}(\nu)$ . These complex amplitudes can be computed as:

$$\mathcal{F}(\nu_x) = \int_{-\infty}^{+\infty} f(x) \exp[i 2\pi \nu_x x] dx \quad (3.11)$$

which is called the *Fourier transform* of  $f(x)$ . The functions  $f(x)$  and  $\mathcal{F}(\nu)$  are (inverse) Fourier transforms of each other and both contain the full information of the other. If one is known, the other can be calculated.

The Fourier transform and its inverse have some important properties such as linearity and that translations in space merely corresponds to a phase factor the Fourier transform. A list of these properties can be found in Saleh and Teichs textbook [ST91b], the notation of which will be used here.

In the context of wave optics, some light field may be described by the complex wavefunction

$$E(\mathbf{r}, t) = A(\mathbf{r})e^{i\omega t} \quad (3.12)$$

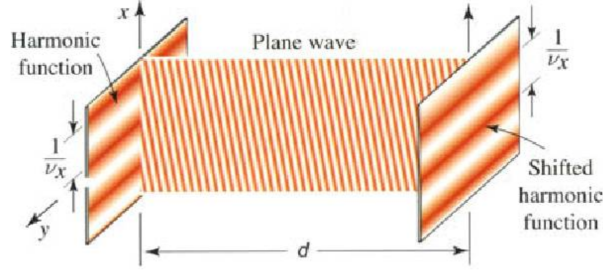


Figure 3.1: Plane Wave, appearing as harmonic functions in the  $z = 0$  and  $z = d$  planes

with angular frequency  $\omega$  and complex amplitude  $A$ . This wave must satisfy the wave equation

$$\nabla^2 E(\mathbf{r}, t) - \frac{1}{c^2} \frac{\partial^2 E(\mathbf{r}, t)}{\partial t^2} = 0 \quad (3.13)$$

Substituting 3.12 into the wave equation above, *Helmholtz Equation* is obtained:

$$\nabla^2 E(\mathbf{r}, t) + k^2 E(\mathbf{r}, t) = 0 \quad (3.14)$$

with

$$k = \frac{\omega}{c} \quad (3.15)$$

being the wavenumber.

Many different wavefunctions may solve the Helmholtz equation, however let us investigate a simple solution, the plane wave with wavenumber  $k = \sqrt{k_x^2 + k_y^2 + k_z^2}$ :

$$E(\mathbf{r}) = A \exp[-i\mathbf{k}\mathbf{r}] = A \exp[-i(k_x x + k_y y + k_z z)] \quad (3.16)$$

Such a plane wave is depicted in figure 3.1, where the plane wave is depicted propagating a distance  $d$ . Before the concept of a Fourier decomposition is introduced to describe the propagation of an *arbitrary* light field let us first look at the simple example of a plane wave. The propagation of a plane wave can be fully described by the above Helmholtz equation. However as we will see that any light field can be described as a combination of plane wave components and that, if propagation of these components is known, the propagation of the whole arbitrary field can be calculated.

The field of the plane wave in figure 3.1 is also depicted in the  $z = 0$  and  $z = d$  planes. Within these planes, the plane wave appears as a harmonic function of spatial frequencies  $\nu_x = k_x/2\pi$  and  $\nu_y = k_y/2\pi$ :

$$f(x, y) = E(x, y, 0) = A \exp[-i2\pi(\nu_x x + \nu_y y)] \quad (3.17)$$

The wave vector  $\mathbf{k}$  is at an angle of  $\theta_x = \sin^{-1}(\lambda\nu_x)$  and  $\theta_y = \sin^{-1}(\lambda\nu_y)$  with the

$x - z$  and  $y - z$  planes. Here we can recognise, that the Fourier transform of  $f(x, y)$  is simply given by

$$\mathcal{F}(\nu_x, \nu_y) = \iint_{-\infty}^{+\infty} f(x, y; \nu_x; \nu_y) \exp[i 2\pi(\nu'_x x + \nu'_y y)] dx dy \quad (3.18)$$

$$= \iint_{-\infty}^{+\infty} A \exp[i 2\pi(\nu_x x + \nu_y y)] \exp[-i 2\pi(\nu'_x x + \nu'_y y)] dx dy \quad (3.19)$$

$$= A \delta(\nu_x - \nu'_x) \delta(\nu_y - \nu'_y) \quad (3.20)$$

where  $\delta(\nu_i - \nu'_i)$  is the *Dirac delta function*.

The Delta function arises because the plane wave only consists of one frequency component with amplitude  $A$ , while the ‘weights’ of all other frequency components are zero.

As expected, we find that the plane wave is described by only one frequency component per spatial direction. Since the wavenumber  $k$  and two of its components in the plane  $z = 0$  are known, the third component can be determined to be:

$$\nu_z = \sqrt{k^2 - k_y^2 - k_x^2}/2\pi \quad (3.21)$$

Therefore, as the phase of the beam evolves with  $\exp[-ik_z z]$  at a distance  $d$ , the field gains an additional phase

$$\mathcal{H}(\nu_x, \nu_y, z = d) = \exp[-ik_z d] \quad (3.22)$$

$$= \exp \left[ -id \sqrt{k^2 - k_y^2 - k_x^2} \right] \quad (3.23)$$

which is called the *transfer function of free space*.

This means that the plane wave appears in the  $z = d$  plane as

$$g(x, y) = \iint_{-\infty}^{+\infty} \mathcal{H}(\nu_x, \nu_y) \mathcal{F}(\nu_x, \nu_y) \exp[-i 2\pi(\nu_x x + \nu_y y)] d\nu_x d\nu_y \quad (3.24)$$

$$= A \exp[-i 2\pi \nu_z z] \exp[-i 2\pi(\nu_x x + \nu_y y)] \quad (3.25)$$

$$= E(x, y, z = d) \quad (3.26)$$

This example was only able to describe the propagation of a plane wave, which was already fully described by Equation (3.16). However due to the linearity of the Fourier transform we can perform this kind of propagation for any arbitrary light field. If only the intensity (and phase<sup>1</sup>) at some input plane is known, the field can be propagated into any direction by the following the same few steps as above.

---

<sup>1</sup>If an image is taken with a laser beam that is collimated in the object plane, we can safely assume the phase of the light field in the object plane to be flat. Thus knowledge of the intensity alone is sufficient to propagate the field. In the case of a lens it is clear however that the intensity may be flat, but the phase actually gives the full information about the propagation of the field.

First the light is split into its spatial frequency components via the Fourier transform, then each frequency component is propagated to the distance  $d$  by multiplying the transfer function of free space. Then all components are recombined into a field at position  $z = d$ , via the inverse Fourier transform. In short, as long as we know the field  $f(x, y)$  at some input plane, the field  $g(x, y)$  at any output plane is given by Equation (3.24).

### Fourier Transformation with a lens

One of the more interesting results of the above propagation through real space is the fact, that a lens can be used to perform a Fourier transform. Put more precisely, within the *Fresnel approximation* the field in the back focal plane of a lens is exactly the Fourier transform of the field in its front focal plane. That means a lens ‘sorts’ the frequency of the light field in space. To see this, one can approximate the transfer function of free space for  $\nu_x^2 + \nu_y^2 \ll 1/\lambda^2$ . Within the Fresnel approximation the transfer function of free space then reads [ST91b]:

$$\mathcal{H}(\nu_x, \nu_y, z = d) = \exp[-i k d] \exp[i \pi \lambda d (\nu_x^2 + \nu_y^2)] \quad (3.27)$$

As we will typically be dealing with laser beams travelling along the axis of a long optical path, this will usually be true within this thesis.

With Equation (3.27), the input beam is propagated from the front focal plane to the lens. The lens is assumed to be thin and to imprint a phase

$$\Delta\varphi_{lens}(x, y) = \exp\left[ik \frac{(x^2 + y^2)}{2} = exp f\right] \quad (3.28)$$

Then the beam is further propagated from the lens to a distance  $d$ , following Equation (3.24). The field is then given by

$$g(x, y) = \mathcal{F}\left(\frac{x}{\lambda f}, \frac{y}{\lambda f}\right) \cdot \frac{i}{\lambda f} \exp[-i k(d + f)] \exp\left[i\pi \frac{(x^2 - y^2)(d - f)}{\lambda f^2}\right] \quad (3.29)$$

Thus in the back focal plane, i.e. at  $d = f$ , the intensity of the beam is given by

$$I(x, y) = \frac{1}{(\lambda f)^2} \left| \mathcal{F}\left(\frac{x}{\lambda f}, \frac{y}{\lambda f}\right) \right|^2 \quad (3.30)$$

which is the Fourier transform of the input field, scaled by  $1/\lambda f$ .

The sorting of frequency components can have interesting implications. By placing an aperture or a beam block in the Fourier plane for example, one can cut out specific frequencies of the image. An aperture will cut the high frequency components and thus limit the resolution of the image. However, a beam block in the centre of the beam will block the low frequency parts and will act as a sort of high-pass filter, where only edges



of the object will show up in the image. These kinds of filters find use in compression and pattern recognition software and neatly showcase the Fourier transforming abilities of a lens. An example of such a high pass filter is depicted in figure 3.2. One can clearly see that blocking a part of the in the focal plane of the first lens in a 4f-setup blocks most of the intensity of the light. But what remains are the high frequency components, that give rise to the edges in the picture.

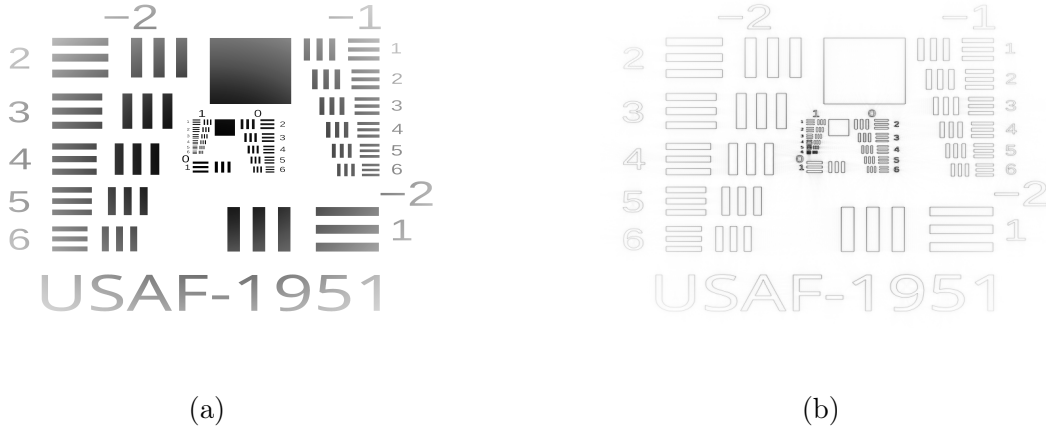


Figure 3.2: Simulation of USAF1951 test image illuminated by a Gaussian  $421nm$  laser beam of  $20mm$  waist. The smallest group (1,6) has a linewidth of  $80\mu m$  in the object plane. The intensity in the image plane of a 4f-setup with  $f_1 = 32.2mm$  &  $f_2 = 75mm$  is shown in (a) without and in (b) with a beam block of  $500\mu m$  radius that was placed in the Fourier plane.

### 3.1.3 Resolution Limit

For any imaging scheme, light that has been emitted, scattered or transmitted at some point in space has to be collected and redirected onto an imaging screen. Imaging small structures can be challenging however. Let us imagine we want to image an infinite grating of structures with a spacing of  $\Lambda$  (see Figure 3.3). Whether the grating is made to be of varying thickness or whether it consists of many slits does not affect the following discussion. The diffraction of the wave will be (to first order) only be affected by the periodicity of the grating  $\Lambda$ .

Let the grating be illuminated with a monochromatic plane wave  $E(x, y, z) = E_0 \exp[-2k_x x]$  at a right angle to the grating ( $\theta_i = 0$ ) where  $k_x = |\mathbf{k}|$  and investigate the field in the  $yz$ -plane. In the far field, the wave will interfere constructively with itself at angles  $\theta$  to the x-axis, where the path length difference  $\Delta l$  introduced by

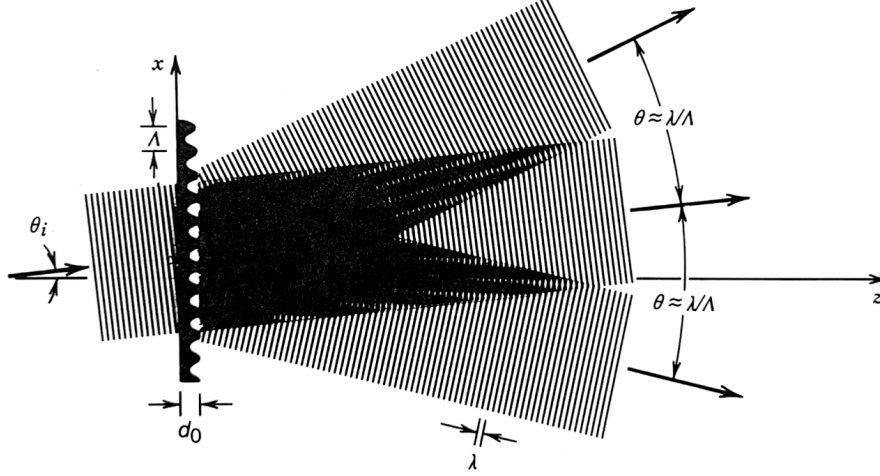


Figure 3.3: A diffraction grating consisting of a thin transparent plate of periodically varying thickness, with a period of  $\Lambda$ . The incident wave with a wavelength  $\lambda$ , angled at  $\theta_i$  to the grating, is split into a zeroth and two first orders, angled at  $\theta \approx \lambda/\Lambda$ . Figure taken from [ST91c].

variations in the plate's thickness is:

$$\Delta l = m\lambda \quad \text{for } m \text{ in } [0,1,2,3\dots] \quad (3.31)$$

$$\Rightarrow \sin(\theta) = m\lambda/\Lambda \quad (3.32)$$

Thus for decreasing slit periodicity  $\Lambda$ , the beam will be diffracted at larger and larger angles  $\theta$ . When  $\Lambda = \lambda$ , even the first order will be diffracted at an angle of  $90^\circ$ . In this case the information on the spatial frequency of the grating is lost and cannot be collected on a screen, even if it is infinitely large.

Similarly, if we are only able to collect a certain part of the light after transmission, for example a light cone at half-angles smaller than  $\Omega$ , only diffracted beams at angles  $\theta \leq \Omega$  can be collected and imaged. This the minimal observable grating size is then given by:

$$\Lambda = \lambda / \sin(\Omega) \quad (3.33)$$

If the system has a refractive index  $n$ , this equation has to be adjusted to

$$d = \frac{\lambda}{n \sin(\Omega)} = \frac{\lambda}{\text{NA}} \quad (3.34)$$

where NA is called the *numerical aperture*.

However, this is only true for coherent light sources like the plane wave chosen in this example. Using fully spacially incoherent light, the resolution may actually be improved by a factor of two [Smi13]. This stems from the fact that a fully incoherent light source illuminates the grating at any angle. Thus the  $m = 0$  order might point at  $90^\circ$  to the

grating, increasing the maximal angle between zeroth and first order to  $180^\circ$ . The same principle can also be exploited by using angled coherent light.

Then, as discussed in Abbe's 1882 paper [Abb82], the resolution limit for periodic structures and incoherent light is thus given by *Abbe's diffraction limit*:

$$\Lambda = \frac{1}{2} \frac{\lambda}{\text{NA}} \quad (3.35)$$

Abbe also notes that, while this limit might only be strictly true for periodic structures, his experience shows that objects of any shape will not be resolved sufficiently below this limit, but 'will look more and more alike (becoming more and more circular or elliptical in form)'[Abb82].

From Equation (3.35) we see that, when imaging small objects, smaller wavelengths are favourable. In practice however using arbitrarily short wavelengths is not possible. Usually due to the availability of light sources at a specific frequency which may cater a certain atomic transition suitable for imaging, the choice is quite restricted. In fields like biology, short wavelengths might also become damaging to the sample, while in atomic physics, one will have to find an atomic transition of matching frequency. Thus, typically rather a certain wavelength will be chosen and the NA of the system will be maximized. If (as in oil submersion microscopes) the refractive index of the system might be increased, one can reach NA values greater than 1.

In the case of cold quantum gas experiments, one cannot (without difficulty) place an objective close to the object, as the atoms sit in vacuum. In the BoDy experiment here in Heidelberg, a  $\text{NA}=0.6$  is achieved by placing a large objective as close to a re-entrant viewport as possible.

### 3.1.4 4f-Imaging

After collecting as much light as possible, to form an image of an object one has to replicate the light field from the object plane as close as possible in the image plane. There are two standard approaches to do so, using lenses to guide and refocus the light in the correct plane:

#### Imaging with a single lens

From both ray and Fourier optics we can find that if an object is placed a distance  $d_1$  from a lens, an image of the object will be formed at a distance  $d_2$  if the focal length of the lens is (see [ST91b]):

$$\frac{1}{f} = \frac{1}{d_1} + \frac{1}{d_2} \quad (3.36)$$

The resulting image will have a magnification of  $M = -d_2/d_1$ .

## Imaging with two lenses

By using two lenses in a so-called 4f-configuration, one might gain some control over the imaging process. To achieve an imaging configuration the first lens with focal length  $f_1$  has to be placed a distance  $f_1$  from the object and the second lens has to be placed a distance  $f_1 + f_2$  from the first lens. As both lenses perform a Fourier transform of the field at the front focal plane to the back focal plane (see section 3.1.2) the Fourier transform of the object plane will be formed in the so-called *Fourier plane* between the lenses. The image of the object plane will then be formed in the back focal plane of the second lens, a distance  $d = 2f_1 + 2f_2$  from the object. This configuration has mostly two advantages. Firstly, one can access the Fourier plane of the image in the focal plane of the first lens. This can be important for phase sensitive imaging schemes such as phase contrast imaging (see Section 3.2.2). Secondly, the magnification of a 4f-imaging system is given by  $M = -f_2/f_1$ . Thus, by adjusting  $f_1$  and  $f_2$  accordingly, an arbitrary magnification might be selected.

Interestingly, if the phase information of the light field in the imaging plane is not important (such as in an absorption imaging scheme 3.2.1) the distance between lenses  $L_1$  and  $L_2$  is irrelevant. One may choose the distance between  $L_1$  and  $L_2$  according to the constraints on the optical table, while being able to control the magnification via the choice of  $f_1$  and  $f_2$ . If the distance between the lenses is chosen to be zero, in fact if the lenses were to be glued together, one recovers the single lens imaging system where  $d_1 = f_1$ ,  $d_2 = f_2$  and the focal length of the combined lens is  $f = \frac{1}{f_1} + \frac{1}{f_2}$  according to the lens-makers-equation.

## 3.2 Overview of Imaging Schemes

Depending on experimental setup, particularly the density of atoms and goal of the measurement different imaging schemes may be appropriate. In time-of-flight (ToF) measurements, the atomic density is typically low enough that a linear relationship between the recorded intensity and the atomic density can be assumed. However, when imaging dense atomic clouds in-situ, some additional care is required. As the atomic cloud may become opaque to the imaging beam and due to the closely spaced atoms () a resonant van der Waals interaction can be induced [Cho+12]. However, these issues can be reduced by imaging at intensities far above the saturation intensity.

In the following the most common imaging methods and their applications to in-situ imaging of dense atomic clouds will be described.

### 3.2.1 Absorption Imaging at Low and High Intensity

#### Absorption at Low Intensity

For low atomic densities, especially after ToF, absorption imaging at low intensity is a common [You+10; Wen15; Soh+21; Jin+23], easily implemented imaging scheme. Here, a resonant laser beam is shot at the atoms and a camera behind the atoms records their ‘shadow’ caused by absorption [KDS99].

Equation (3.4) can be applied to calculate the OD from the transmitted intensity. In the low intensity regime ( $s \ll 1$ ) and on resonance ( $\Delta \approx 0$ ) Equations 3.5 and 3.6 become:

$$\varphi(\mathbf{r}, \Delta) = -\sigma_0 \bar{n}_z(x, y) \frac{\Gamma \Delta}{4\Delta^2 + \Gamma^2(1 + s)} \approx 0 \quad (3.37)$$

$$\epsilon(\mathbf{r}, \Delta) = +\sigma_0 \bar{n}_z(x, y) \frac{\Gamma^2}{4\Delta^2 + \Gamma^2(1 + s)} \approx \sigma_0 \bar{n}_z(x, y) \quad (3.38)$$

The density of the atoms can then in principle be calculated, by comparing the initial intensity  $I_{probe}$  and the transmitted intensity after absorption  $I_{abs}$ , retrieving *Lambert-Beers law*:

$$\ln(I_{probe}/I_{abs}) = -\epsilon \quad \Rightarrow \quad \bar{n}_z(x, y) = -\frac{\ln(I_{probe}/I_{abs})}{\sigma_0} \quad (3.39)$$

In practice however, merely imaging the distribution of  $I_{abs}$  in a single absorption picture is not really useful as the intensity distribution  $I_{probe}$  will not be well known.

But by simply measuring a *flat field* reference image with the same intensity and exposure time, but without the atoms, the received intensity distribution at the detector can be measured and Equation (3.39) can be applied. That is to say, by just measuring *both*  $I_{probe}$  and  $I_{abs}$  the OD can be computed.

The output of the camera sensor always includes some noise that consists of different contributions, each with a different scaling with intensity (see Section 3.3). To be able to eliminate some of these contributions, that would otherwise artificially increase the measured intensity a third picture should be taken. This will be called a *dark field* reference image as it will be taken without any probe light. As some of the processes contributing to the noise can be time dependent, both the dark field and the flat field should be taken at the same exposure time as the absorption image. Also, many dark and many flat field images can be taken and averaged to reduce shot noise in these reference images.

In digital counts the absorption image at pixel  $(i, j)$  is given by:

$$C_{abs}(i, j) = I_{abs} \cdot \eta \cdot \frac{1}{F} + C_{dark}(i, j) \quad (3.40)$$

where  $\eta$  is the *quantum yield gain* given in [electrons/photon] and  $\frac{1}{F}$  is the Analogue-to-Digital (ADC) conversion factor in [counts/electron].

The flat field reference in digital counts at pixel  $(i, j)$  is then:

$$C_{probe}(i, j) = I_{probe} \cdot \eta \cdot \frac{1}{F} + C_{dark}(i, j) \quad (3.41)$$

And the dark field reference in digital counts at pixel  $(i, j)$  is simply  $C_{dark}(i, j)$ .

From this the column density **at low intensity** can be calculated as [Wen15]:

$$\epsilon \approx \sigma_0 \bar{n}_z(x, y) = -\ln \left( \frac{C_{abs} - C_{dark}}{C_{probe} - C_{dark}} \right) \quad (3.42)$$

$$= -\ln \left( \frac{C_{out}}{C_{in}} \right) \quad (3.43)$$

where  $C_{in} = C_{probe} - C_{dark}$  and  $C_{out} = C_{abs} - C_{dark}$ .

As low intensity absorption is only useful for low OD, it will often be used for imaging atoms after they are released from a trap and expand during a few (tens of) millisecond long ToF. During ToF the atomic cloud will expand and typically reach an OD below one where low intensity absorption may be applicable.

## Absorption at High Intensity

If the *bare OD* is too large to be resolved by the low intensity absorption imaging system, (according to Equation (3.6)) increasing the intensity of a near-resonant beam may reduce the OD again to measurable values [Hor+17; Hue+17; Wen15; Rei+07].

In the resonant, high saturation case the optical depth  $\epsilon$  is given by

$$\epsilon(\mathbf{r}, \Delta = 0) = \sigma_0 \bar{n}_z \frac{1}{1 + s} \quad (3.44)$$

In this case the Lambert-Beer law is modified to:

$$\frac{dI(\mathbf{r})}{dz} = -\sigma_0 n \frac{1}{1 + I(\mathbf{r})/I_{sat}} I(\mathbf{r}) \quad (3.45)$$

integrating along  $z$  an expression for the bare OD can be obtained [Hue+17]:

$$\sigma_0 \bar{n}_z(x, y) = -\ln \left( \frac{I_{abs}(\mathbf{r})}{I_{probe}(\mathbf{r})} \right) + \frac{I_{probe}(\mathbf{r}) - I_{abs}(\mathbf{r})}{I_{sat}^{eff}} \quad (3.46)$$

where  $I_{sat}^{eff} = \alpha I_{sat}$  is the effective saturation intensity, where  $0 < \alpha < 1$  accounts for non-perfect polarisation and magnetic field orientation that might reduce the actual saturation intensity.

In digital counts Equation (3.46) reads:

$$\sigma_0 \bar{n}_z(i, j) = -\ln \left( \frac{C_{abs}(i, j) - C_{dark}(i, j)}{C_{probe}(i, j) - C_{dark}(i, j)} \right) + \frac{C_{probe}(i, j) - C_{abs}(i, j)}{C_{sat}^{eff}} \quad (3.47)$$

$$= -\ln \left( \frac{C_{out}(i, j)}{C_{in}(i, j)} \right) + \frac{C_{in}(i, j) - C_{out}(i, j)}{C_{sat}^{eff}} \quad (3.48)$$

The only remaining problem now is that the count  $C_{sat}^{eff}$  has to be calibrated. Horikoshi et al.[Hor+17] propose to measure the bare OD at different intensities put keeping the atomic density constant. By rewriting Equation (3.48) as:

$$-\ln \left( \frac{C_{out}(i, j)}{C_{in}(i, j)} \right) = \sigma_0 \bar{n}_z(i, j) - \frac{C_{in}(i, j) - C_{out}(i, j)}{C_{sat}^{eff}} \quad (3.49)$$

They identify  $-\ln \left( \frac{C_{out}(i, j)}{C_{in}(i, j)} \right)$  as a linear function of  $C_{in}(i, j) - C_{out}(i, j)$ , scaled by  $C_{sat}^{eff}$ . Thus, by taking many pictures at different intensities, they can determine  $C_{sat}^{eff}$  as the slope of this linear function. This method is however limited to the accuracy with which the atom density can be kept constant between different experimental runs. Also, the parameter  $\alpha = I_{sat}^{eff}/I_{sat}$  remains elusive. Reinaudi et al. [Rei+07] present a method to determine  $\alpha$  directly for high intensity absorption imaging. However their method again relies on extracting the parameter from many measurements at the same atomic density.

Another way to calibrate the absorption imaging system however, is presented by Hueck et al.[Hue+17]. They measure the scattering rate directly by measuring the momentum transferred from the imaging beam to the atomic cloud after ToF with an second imaging system. Thus, by measuring the scattering rate  $\gamma(s) = \frac{\Gamma}{2} \frac{s}{1+s}$  for different Intensities, they can determine  $I_{sat} = I_{probe}/s$  directly.

### 3.2.2 Phase Contrast Imaging

Instead of reducing the OD by increasing  $s$  and using light on resonance, one might decrease the OD by increasing  $\Delta$  and use the dispersive phase  $\varphi$  to image the atomic density [KDS99]. First, considering equations 3.5 and 3.6, it can be recognised that  $\epsilon$  is proportional to  $1/\Delta^2$  while  $\phi$  is proportional to  $1/\Delta$ . Thus by increasing  $\Delta$  to above  $10\Gamma$ , the effect of  $\epsilon$  on the overall phase  $\beta$  can be kept small (below 1%) compared to the effect of  $\varphi$ .

As imaging sensors are only sensitive to the intensity but not the phase of light, the remaining issue is to map the phase  $\beta \approx \varphi$  onto intensity. In a absorption imaging setup,

the intensity of the transmitted beam is measured, given by:

$$I(\mathbf{r}) = |E(\mathbf{r})|^2 = |E_{probe} \exp[i\beta]|^2 \quad (3.50)$$

$$= |I_{probe} \exp[i\varphi - \epsilon/2]|^2 \quad (3.51)$$

$$= I_{probe} \exp[-\epsilon] \quad (3.52)$$

where the dispersive phase  $\varphi$  just cancels out. However, a variety of different methods to extract the phase  $\varphi$  from an intensity image. Similar to methods of x-ray tomography [Lan+08],  $\varphi$  may be reconstructed from the diffraction pattern of a far detuned beam of light via the transport of intensity equation (TIE) [Wig+16]. More commonly for cold quantum experiments, the phase will be mapped to intensity by letting the beam interfere with itself. This may be done, employing off-axis holography [SMS20], where the probe beam is split into an arm the interacts with the atoms and a separate non-interacting arm, which interfere on a camera sensor. The two separate arms may add some complexity to the experimental setup however, as their divergence, angle on the camera and polarisation have to be matched.

Another option, adding very little experimental complexity is Faraday imaging. Here, an atomic cloud in an external magnetic field is illuminated by an far detuned beam, linearly polarised perpendicular to the magnetic field. The linear polarisation is a superposition of left- and right-handed circular polarised light. Depending on the direction of the magnetic field, the transition probability of light of one handedness will be much greater than the other. Due to the Faraday effect, the polarisation of the light is rotated while passing through the atomic, by a degree proportional to the density of the atomic cloud. This method, often called *Faraday imaging*, exploits this birefringence of a spin polarised atomic cloud to map the phase  $\varphi$  to the intensity of the beam. By simply placing polarisation filter in front of the camera, the beam can be made to interfere with itself resulting in  $\varphi$ -dependent intensity variations on a screen [Soh21; BSH97; Cab+18; Kad+16; Gaj+13]. This method required a specific magnetic offset field and a light of linear polarisation which again limits the usability of this method.

Circumventing these limitations, an experimentally even simpler method can be used. The interference between two parts of the imaging beam, where one interacts with the atoms and the other does not can be achieved by ‘manually’ imparting a relative phase shift between these two parts of the beam. By focussing the imaging beam after the atoms and placing either a small beam block [And+96] or a phase plate [And+97; Mep+10; Joo13; Sad06] in the Fourier plane of the beam, the two parts of the beam can be made to interfere regardless of polarisation or external magnetic fields. This again causes the phase  $\varphi$  to be mapped onto the intensity which can then just be measured by a camera. These so-called *phase contrast imaging* schemes yield signal to noise ratios similar to Faraday imaging schemes[Gaj+13] and as it presents an easily implemented, versatile and



non-destructive imaging method, it was decided to be implemented for high density in-situ imaging in the BoDy experiment. Specifically, here the focus will be of implementing such a scheme with a phase plate.

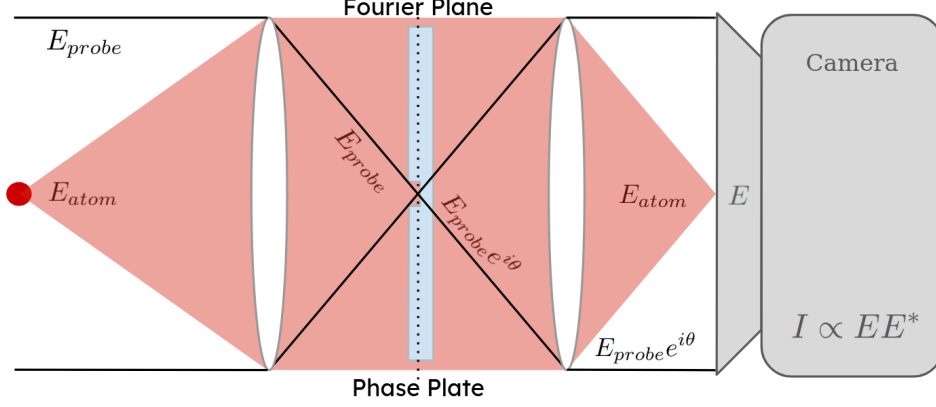


Figure 3.4: 4f Imaging Setup including a phase plate in the Fourier plane, the (mostly) shifts the phase of the focussed  $E_{probe}$  field, while the  $E_{atom}$  field remains (mostly) unaffected.

As visualized in figure 3.4, a phase plate is transmissive plate, containing a small phase spot that is used to imprint an additional phase to a part of the beam. Specifically, the part of the beam that did not ‘see’ the atoms ( $E_{probe}$ ) is to be shifted by a small phase compared to the rest of the beam, that did collect a phase at the atoms ( $E_{atom}$ ). Separating these to parts of the beam in space to manipulate them separately can be achieved in a 4f imaging setup, where  $E_{probe}$  will be focussed in the focal point of the first lens, i.e. in the Fourier plane of the 4f setup. As  $E_{atom}$  gains an additional phase and is diffracted at the atoms, it is no longer collimated before the first lens. Thus the beam will not be focussed down to the same focal point.

By placing a small<sup>2</sup> optical element into the Fourier plane that shifts the intensity of a large part of the probe beam<sup>3</sup> can acquire a phase shift, while the other part of the beam is nearly untouched. In practice this can be done with a glass plate that is polished very flat and that has only one small indentation or a small protrusion. Due to the refractive index of glass being larger than 1, the two parts of the beam pick up a relative phase  $\theta$ . The glass plate is positioned at the Fourier plane, such that only the focal point of  $E_{probe}$  coincides with the so-called spot.

This simple method allows us to imprint the dispersive phase  $\varphi$  into the measured intensity. Following the Meppelink et al.[Mep+10], the beam may be split into two parts (where the dependence on  $\mathbf{r}$  is omitted for readability):

$$E = E_{probe} + E_{atom} = E_{probe} + (E_{probe} \exp[i\beta] - 1) \quad (3.53)$$

<sup>2</sup>on the order of the beam waist

<sup>3</sup>remember, that 99.97% of the power of a beam is transmitted within a circle of twice its waist

By using far detuned light  $\beta \approx \varphi$  can be assumed. By adding a phase shift between these to parts of the beam, the intensity becomes:

$$I(\theta, \varphi) = |E_{probe} \exp[i\theta] + E_{atom}|^2 = |E_{probe} \exp[i\theta] + E_{probe}(\exp[i\varphi] - 1)|^2 \quad (3.54)$$

$$= I_{probe} |\exp[i\theta] + \exp[i\varphi] - 1|^2 \quad (3.55)$$

$$= I_{probe} (3 - 2 \cos(\theta) + 2 \cos(\theta - \varphi) - 2 \cos(\varphi)) \quad (3.56)$$

With the choice of different relative phases  $\theta$ , the contrast of the interference of these two beams can be adjusted. Figure 3.5 illustrates the phase dependent intensity in the image plane is plotted for different choices of  $\theta$ .

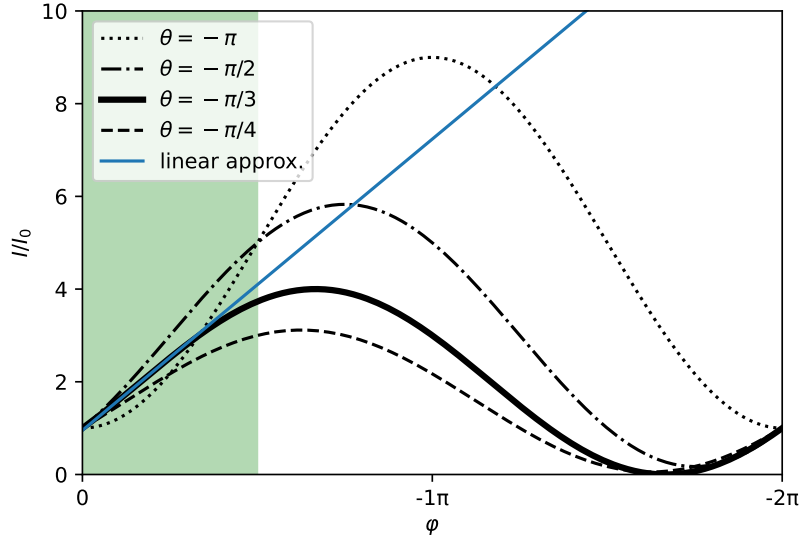


Figure 3.5: Intensity in the phase contrast image in dependence of  $\varphi$  for different choices of  $\theta$ . The green region marks a region of approximate linearity (where the difference between approximated and precise result is smaller than 10%) for  $\theta = -\pi/3$ .

In this thesis, following [Mep+10], a choice of  $\theta = -\frac{\pi}{3}$  will be made (see Section 4.5). In this case Equation (3.56) can be simplified. By referencing ones favourite collection of trigonometric relations [Brü06] one can recognise that

$$I(\theta = -\pi/3, \varphi) = 2I_{probe} \left( 1 + \sin \left( -\frac{\pi}{6} - \varphi \right) \right) \quad (3.57)$$

$$\approx 2I_{probe} \left( \frac{6 - \pi}{6} - \varphi \right) \quad (3.58)$$

Thus for low small  $\varphi$  this equation will be reasonably linear and the bare OD may be extracted form a set of three images similar to Equation (3.48) as

$$\varphi = \frac{6 - \pi}{6} \frac{C_{out} - C_{in}}{C_{in}} \quad (3.59)$$

where  $C_{in}$  and  $C_{out}$  are defined as in equations 3.40-3.43.

Remembering Equation (3.5), for  $\Delta > 10\Gamma$  and  $s < 1$ , the bare OD can be connected to  $\varphi$  as:

$$\sigma_0 \bar{n}_z(x, y) = -\varphi \frac{4\Delta}{\Gamma} \quad (3.60)$$

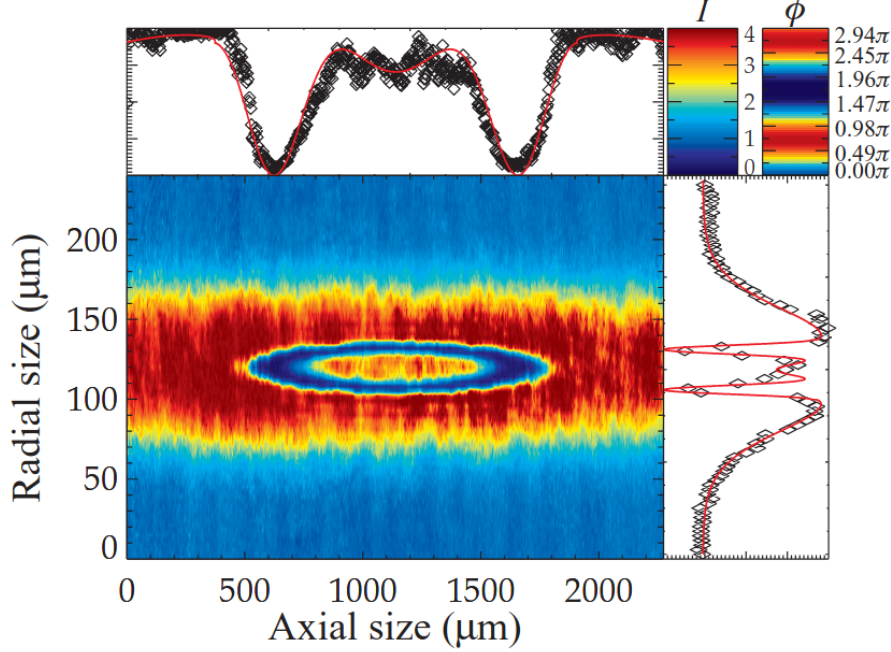


Figure 3.6: Phase contrast image of dense atomic cloud. As the light acquires a phase of up to  $3\pi$ , the interference pattern shows both minima and maxima. As long as the phase varies smoothly enough, the atomic density distribution can be extracted, following Equation (3.57). Figure taken from [Mep+10].

Meppelink et al. [Mep+10] have demonstrated however, that one can make use of the periodicity of the acquired phase. By allowing  $\varphi$  to reach values of multiple  $\pi$  and using the periodicity of the resulting intensity signal, they are able to increase the dynamic range of this imaging scheme significantly. As the density of the atomic cloud in figure 3.6 increases toward the center,  $\varphi$  increases. However, once  $\varphi > \frac{2\pi}{3}$ , the intensity in the image *decreases* until  $\varphi > \frac{6\pi}{3}$ . Following Equation (3.57) and figure 3.5 the intensity is periodic in  $\varphi$ . Using a suitable fitting algorithm the overall phase in a continuous image, and thus the bare OD, can be determined.

### 3.2.3 Fluorescence Imaging

Fluorescence imaging is used for imaging either pinned single atoms [Su+25; Ber+18] or entire atomic clouds [Büc+11; DeP+00] with up to single atom number resolution.

In fluorescence imaging, atoms are illuminated with near-resonant light. Each atom may absorb and re-emit many photons, are collected off-axis from the exciting beam.

This way, only the fluorescence photons are counted, while (ideally) no background light from the exciting beam reaches the detector. So in principle arbitrarily high intensities can be used to detect arbitrarily low densities (or single atoms). However, imaging freely expanding atomic clouds, the exposure time and intensity are limited as not to disperse the atomic cloud. Together with possible multiple scattering events within optically thick atomic clouds and saturation effect, fluorescence imaging suffers similar limitations as resonant absorption imaging. Albeit potentially at a larger signal to noise ratio, due to a lack of background light.

There are however some drawbacks. As there is no ‘bright background’ that could be used to calibrate the intensity of the beam, the actual calibration is more difficult. While a calibration can be done following [Hue+17], it will typically rely on the reproducibility of specific atomic densities in experiment, which can limit the accuracy of the calibration.

Compared to absorption imaging, far greater laser intensities are needed to reach the high intensity regime necessary to reliably image dense clouds [Rei+07]. This means that a large momentum can be imparted on the atoms. Stringently limiting the usable exposure times. To prevent excessive displacement of the atoms during the measurement one might use pulsed, counter propagating beams [Su+25]. This however, adds quite a bit of experimental complexity. And finally, a priori it is difficult to estimate how large the effect of stray light will be on the background intensity. While this is not necessarily a drawback on the method itself, it makes calculating the expected performance of such a system, before embarking on building a more involved optical setup, more challenging and less precise.

As a combination of phase contrast imaging and high intensity absorption imaging can be implemented into the current experimental setup while adding little experimental complexity, and as these are expected to be suitable for high density in-situ imaging at a good SNR, fluorescence imaging was not prioritised.

### 3.3 Noise and the Photon Transfer Curve

In any imaging system there are many different sources of noise. Some might stem from non-ideal experimental setups such as the pixel dependent sensitivity of a sensor, dirt, stray light etc., while others are of fundamental nature such as shot noise. A detailed discussion of different noise sources in photon detection processes is given in [Jan07], including methods to quantify the different noise components in any system.

A brief overview on different noise components including an explanation of the *Photon Transfer Curve* (PTC) will be given here, to later be able to characterise the noise contributions within an existing imaging setup in Section 4.1 and to estimate signal to noise ratios for different imaging schemes in Section 4.3.

### 3.3.1 Shot Noise

When a detector is illuminated by a (perfectly) homogeneous field of light, each pixel will not measure exactly the same number of photons. This is obvious when the field intensity is so weak and the measurement duration so short, that the number of incoming photons is smaller than the number of pixels on the detector. As a pixel can only detect whole numbers of photons, but never half a photon, the photons will have to spread randomly over the whole detector, governed by Bose-Einstein Statistics. The variance of events per pixel (or per time period) is called *shot noise*.

If the photons don't couple to phonons in the detector (in silicon, for  $\lambda < 1000nm$ ) the variance in the number of photons incident per pixel  $N^{pho}$ , is given by:

$$\sigma_{Shot}[photons] = \sqrt{N^{pho}} \quad (3.61)$$

where the bracket is to indicate that  $\sigma_{Shot}$  is measured in number of photons (per pixel) here. As we will talk about numbers of photons, photoelectrons and counts in very similar contexts, this distinction will be made wherever necessary.

As the variance of the number of photons increases, the Signal to Noise Ratio (SNR) for a purely Shot Noise limited process goes as:

$$SNR_{Shot}[N^{pho}] = \frac{N^{pho}}{\sqrt{N^{pho}}} = \sqrt{N^{pho}} \quad (3.62)$$

That means, the SNR improves with the number of photons and is worst for low intensity, which is the reason why photographs and film in dark lighting conditions can look 'grainy'. If a large gain is applied in digital photography (or high ISO film is used), the number of photoelectrons (area of reduced silver halide crystal) can be increased. But this will amplify the signal and the noise equally. Therefore to increase the signal to noise ratio, one can only increase the exposure time, at a lower gain (lower ISO) to increase the actual number of photoelectric events, instead of amplifying their effects.

The digital readout of a camera however will know nothing about the actual number of incident photons that were incident on a pixel. Rather only some part of the incident photons will be converted to photoelectrons. The number of photoelectrons per photon is given by the *Quantum Efficiency* and is given by:

$$Q_e = \frac{N}{N^{pho}} \quad (3.63)$$

where  $N$  is the number of photoelectrons on a pixel. The photoelectrons will then be converted into a certain number of digital counts  $C$  in a analogue to digital converter.

The number of digital counts is finally given by:

$$C = N^{pho} Q_e \frac{1}{F} = \frac{N}{F} \quad (3.64)$$

With this conversion in mind we can rewrite the shot noise in number of counts as:

$$\sigma_{Shot} = \frac{1}{F} \sqrt{Q_e N^{pho}} = \frac{1}{F} \sqrt{N} \quad (3.65)$$

The quantum efficiency  $Q_e$  is usually determined by the architecture of the sensor itself. To artificially increase the number of counts in a picture, one might increase the factor  $1/F$ , but as can be seen above, this will not change the Signal to noise ratio.

### 3.3.2 Fixed Pattern Noise

*Fixed pattern noise* (FPN) describes the variance of counts per pixel between different pixels, while they are illuminated homogenously. Differences in pixel counts can stem from (small) differences in pixel sensitivity, that originate in the manufacturing process of the detector, but they can also be the result of dirt on the detector or even unwanted interference patterns in the optical path.

As these fixed patterns just scale with intensity and thus the number of photoelectrons itself, the FPN is given by:

$$\sigma_{FPN} = Q_{FPN} N \quad (3.66)$$

where  $Q_{FPN}$  is the quality factor of the detector and  $N$  is again the number of photoelectrons.

As  $\sigma_{FPN}$  scales with  $N$  rather than  $\sqrt{N}$ , fixed pattern noise will usually dominate at large intensities. In any reasonable detector, the variance between pixel sensitivity will be rather small and often dust and other dirt will dominate the value of  $P_N$ . Luckily, through flat fielding, most of the FPN can be removed. To do so, one has to illuminate the detector with a field of constant/flat intensity over all pixels and measure the intensity per pixel. By averaging, shot noise can be eliminated. The (normalised) averaged picture of intensity per pixel can be used as mask remove FPN from other images.

### 3.3.3 Read Noise

Finally, read noise  $\sigma_{Read}$  captures all noise in the photon detection process that does not depend on the number of photoelectrons and thus on the incoming intensity. Electrons might be lost in the read-out process, dark currents might alter the electron count; all of these sources may be reduced but ultimately all detectors and sensors have a small but non-zero read noise.

### 3.3.4 Total Noise and Photon Transfer Curve

Including all sources above, the total noise in the digital counts of a sensor can be written as:

$$\sigma_{Total}^2 = \frac{1}{F} \sqrt{Q_e N^{pho}} + \sigma_{Shot}^2 + \sigma_{FPN}^2 \quad (3.67)$$

$$= \sigma_{Read}^2 + \frac{1}{F} N + (Q_{FPN} N)^2 \quad (3.68)$$

As the different noise contributions are independent from each other they add quadratically and  $\sigma_{Total}^2$  becomes a 2nd order polynomial in  $N$ . This allows us to extract the different noise contributions in experimental data, by measuring a *photon transfer curve*. This is done by illuminating the sensor in question homogeneously at different intensities and recording the variance of the observed counts per pixel for each intensity.

By plotting the variance against intensity, and fitting a second order polynomial, we will be able to retrieve the contributions of read noise, shot noise and FPN noise separately. This can allow a more detailed and realistic estimation of expected signal to noise ratios in the system.

# Chapter 4

## Design and Implementation of In-Situ Imaging Schemes for high OD in BoDy Experiment

### 4.1 Characterisation of Imaging System

To be able to choose and design a suitable imaging scheme for the vertical in-situ imaging arm of the BoDy experiment, knowledge of its characteristics is necessary.

The experiment features a custom high resolution objective (see [Phi23]) with a working distance of 22.5mm away from the atoms, an NA of 0.6 and a focal length of 32.2mm. The average resolution over the whole field of view of this objective was measured to be  $(0.6 \pm 1.8)\mu\text{m}$  at depth of field of only  $0.3\mu\text{m}$ . The objective is positioned vertically over the atoms and is intended to be used for the main imaging system.

The camera intended for the main imaging is an ORCA Quest quantitative CMOS camera build by Hamamatsu [KK22], that is able to count the actual number of photons detected by the sensor. Together with a large number of  $4096 \times 2304$  pixels, this makes it an attractive choice for high resolution, high dynamic range imaging. But even a low noise camera like this, has non-zero noise in detection and readout, which will have to be determined to enable a quantitative estimate of the signal to noise ratio (SNR) for different imaging system designs.

Following previous efforts [Bad23] and as described in Section 3.3.4, a photon transfer curve (PTC) was recorded to decompose and quantify different noise contributions. As the read noise  $\sigma_{read}$ , the shot noise  $\sigma_{shot}$  and the fixed pattern noise  $\sigma_{FPN}$  scale differently with intensity (see Equations 3.67), their individual contributions to the overall noise can be determined, by measuring the total variance in a subset of pixels at different intensities and fitting the resulting curve with a second order polynomial. The resulting PTC is depicted in Figure 4.1.



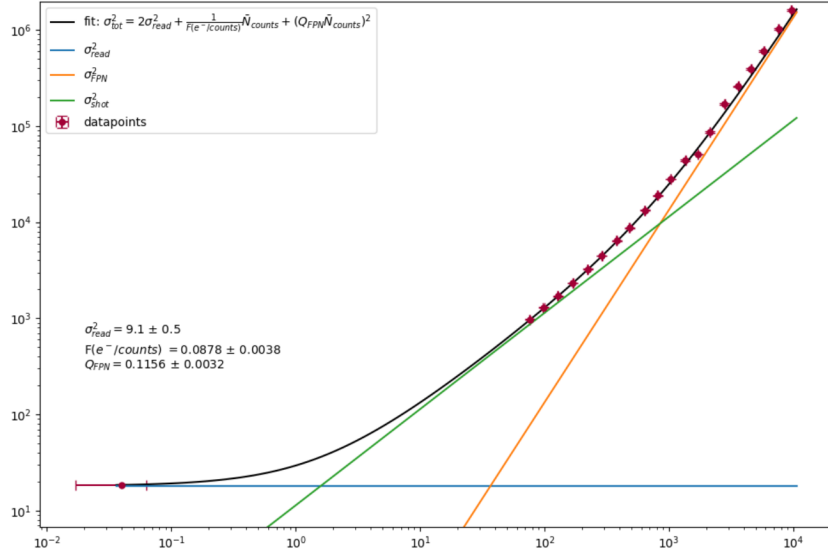


Figure 4.1: Photon Transfer Curve for the vertical imaging arm over a region of 100x100 pixels on the Orca Quest camera. The 421nm imaging beam was modulated to different intensities with an AOM.

The data in for this PTC was taken by modulating the intensity of the imaging beam that was used at that time with an AOM. However, an AOM has a limited modulation range, such that the intensity cannot be reduced down to arbitrarily low levels. (Notice the log scale in the graph that indicates an intensity modulation over three orders of magnitude.) The extra data point at very low intensity, was taken without any imaging light. This data point was taken from a dark image and only contains read noise. As a rather narrow bandpass filter for 421nm light is placed in front of the camera sensor and because the experiment is shielded from external light sources, stray light should have little to no effect.

A read noise in digital counts of  $\sigma_{read}^2[counts] = 9.1 \pm 0.5$  can be extracted with reasonable confidence. However, the image is largely dominated by FPN with quality factor  $Q_{FPN} = 0.116 \pm 0.003$  and there are very few data points that can contribute to the fitting of the factor  $F = 0.088 \pm 0.004$ , which is proportional to the shot noise.

In principle, the FPN can be reduced to an arbitrarily low level by flat fielding (see chapter 3.6 in [Bad23]). By doing so and then repeating the PTC analysis with a corrected image, a better estimate of  $1/F$  may be gained.

However, due to the photon counting capabilities of the camera, a simpler and more precise method was chosen. The factor  $1/F$  can be calibrated by merely plotting a histogram of digital counts per pixel for a very low intensity image. As can be seen in Figure 4.2, the histogram follows roughly a binomial distribution with a peak around 420 counts, where the width of the distribution is given by shot and FPN noise.

But more interestingly, periodic peaks modulate the binomial distribution, each of which connects to a distinct photon number that was detected. By removing the overall

trend of the binomial by a simple quadratic regression the peaks in the remaining distribution can be found numerically (see Figure 4.2). This was done by fitting a Savitzky-Golay filter [SG64] to the discrete bins in the histogram and detecting the peaks in the resulting curve.

A mean distance between two peaks of

$$8.9 \pm 0.4 \text{ [counts/e}^-] = 1/F$$

was found. With this conversion factor the read noise in photoelectrons may be calculated:

$$\sigma_{read} = F\sigma_{read}[\text{counts}] = 0.308 \pm 0.008$$

This result deviates significantly from the manual, where a noise of  $\sigma_{read}^{spec} = 0.27$  is specified, but this might simply be due to an underestimated uncertainty.

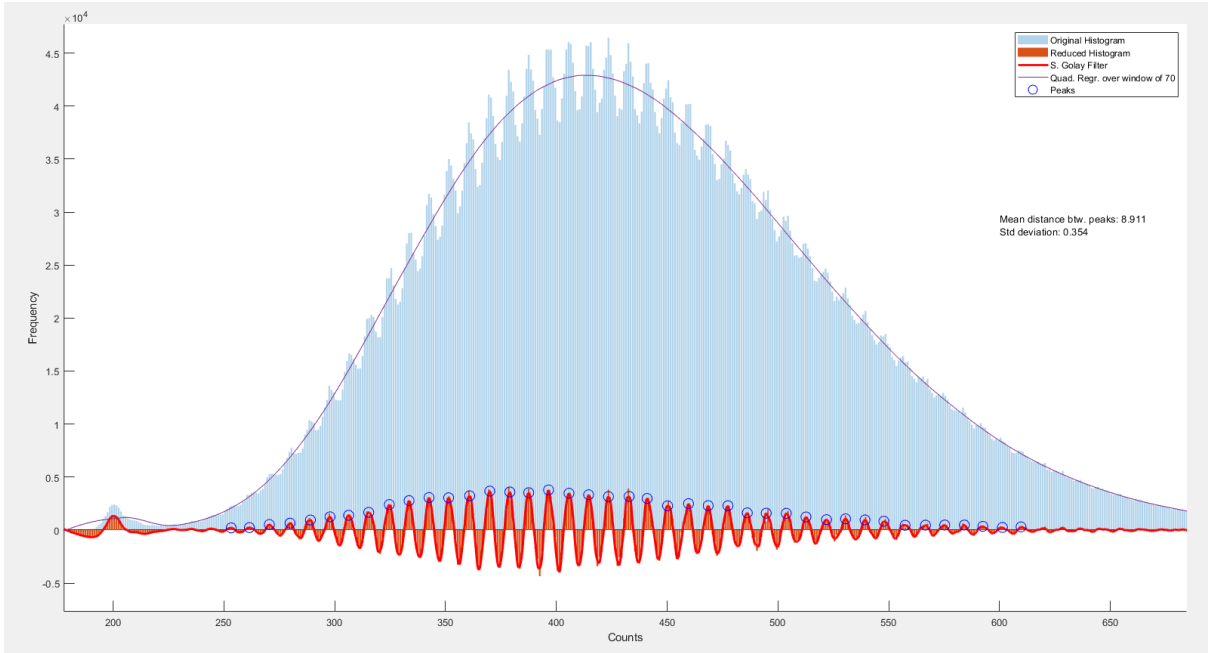


Figure 4.2: Histogram of digital counts per pixel on the Orca Quest camera at an exposure time of 5.3  $\mu$ s

In principle, the read noise may be determined from the histogram as well. As read noise gives rise to the width of the individual peaks in the histogram, the peak-valley modulation may be used to measure  $\sigma_{read}$  [SF16].

In the following calculations however, (see Section 4.3) the read noise determined from the PTC and the conversion factor determined from the histogram were used.

## 4.2 Appropriate Probe Conditions

In equations 3.5 and 3.6 it is assumed that the atomic cloud retains its density and that the detuning does not change during measurement. To be able to extract the OD of the atomic cloud with reasonable precision it is crucial therefore, to find probe conditions under which neither the density distribution of the cloud nor the detuning changes.

During a high intensity pulse, an atom may scatter many photons, and quite a significant impulse may be transferred to an atom, causing it to gain some velocity which, affects both the detuning (due to the Doppler shift) and the local density (as the atoms are dispersed).

This constrains the allowable intensity and duration of the imaging beam. Following Horikoshi et al. [Hor+17], the corresponding limits will be determined below.

### 4.2.1 Doppler Limit

With each absorbed photon, an atom gains a momentum of  $\hbar k$  along the propagation direction of the beam. Upon re-emitting a photon a momentum of the same magnitude will be gained in a random direction. After many scattered photons the mean momentum transferred to the atom is simply given by  $\hbar k$  as the random spontaneous emission cancels out. Thus the (net) velocity gained along the beam direction is  $v_{recoil} = \hbar k/m$  per scattered photon.

This causes a Doppler shift per photon of

$$kv_{recoil} = \frac{\hbar k^2}{m} \quad (4.1)$$

After a time  $t$  the atom will acquire a Doppler shift of

$$\Delta_{Doppler} = R_{sct} \frac{\hbar k^2}{m} \cdot t \quad (4.2)$$

where  $R_{sct} = \frac{\Gamma}{2} \frac{s}{1+s}$  is the scattering rate.

As a reasonable restriction we will simply impose that the Doppler shift be smaller than half the effective linewidth, that is:

$$\Delta_{Doppler} < \frac{\Gamma_{eff}}{2} = \frac{\Gamma}{2} \sqrt{1+s} \quad (4.3)$$

In this case, the influence of the Doppler effect on the OD will be small (compare Equation (3.6)). Thus, explicitly the exposure time cannot exceed

$$t_{doppler}(s) < \frac{\sqrt{1+s}^3}{s} \frac{m\lambda^2}{2\pi\hbar} \quad (4.4)$$

### 4.2.2 Random Walk Limit

We will also impose the limit, that (on average) an atom should not be displaced by more than one pixel on the camera during the imaging pulse. During the imaging pulse the atoms will not only acquire a velocity of  $v = v_{recoil} R_{sct} t$  along the beam direction, but the atom will also perform a random walk on the plane perpendicular to the imaging beam. This causes an RMS velocity increasing with exposure time as  $\langle v^2 \rangle(s, t) = R_{sct} v_{recoil} \cdot t / \sqrt{3}$  [Foo05c] where the factor  $1/\sqrt{3}$  gives the velocity in *one* axis in a 3D random walk. This leads to an average displacement

$$r_{recoil}(t, s) = \int_0^t \sqrt{\frac{1}{\sqrt{3}} R_{sct} v_{recoil} \cdot t} \quad (4.5)$$

Therefore, imposing that this distance shall not surpass the length of one pixel in the object plane  $L_{pix}$  we get the exposure the time limit [Hor+17]:

$$t_{dipl} < \frac{3}{2^{2/3}} \left( L_{pix} \frac{m\lambda}{h} \sqrt{\frac{1}{\Gamma} \frac{1+s}{s}} \right)^{2/3} \quad (4.6)$$

### 4.2.3 Pixel Saturation Limit

Finally, the camera itself imposes a limit on the maximum intensity of an image. It can only read out each pixel with a limited amount of bits, in our case 16bits. Thus there is a maximum number of photoelectrons per pixel that can be processed by the camera, before the pixel saturates. The maximum number of photoelectrons before a pixel saturates is given by

$$N_{max} = (2^{16} - C_{back}) F \quad (4.7)$$

where  $N_{back} = FC_{back}$  is the number of per photoelectrons per pixel that belong to the read noise.

The number of photons that illuminate one effective pixel in the object plane, corresponds to the number of photoelectrons:

$$N = \frac{IL_{pix}^2 t}{E^{ph}} = \frac{IL_{pix}^2 \lambda t}{hc} T_p Q_e \quad (4.8)$$

where  $I$  is the intensity of the beam,  $T_p$  the fraction of photons transmitted from the object plane to the camera and  $Q_e$  is the quantum efficiency of the camera. The exposure time limit due to the saturation of a pixel is then given by:

$$t_{sat}(s, t) < N_{max} \frac{hc}{s \cdot I_{sat} L_{pix}^2 \lambda Q_e T_p} \quad (4.9)$$

As long as the exposure time and the saturation parameter are chosen such that these limit given in Equations (4.4), (4.6) and (4.9) are not exceeded, Equations (3.5) and 3.5 remain valid and a reasonable estimate of the atomic density can be made. What remains to be estimated (in the following section), is the SNR that can be expected for a certain set of parameters in a given imaging scheme.

### 4.3 Estimation of Signal to Noise Ratios for Different Imaging Schemes

With the above values of  $\sigma_{read}$  and  $1/F$  and with knowledge on the constraints for the exposure time in dependence of the intensity, the SNR for different imaging schemes and different parameters can be estimated. Importantly however, the SNR of course depends on the OD that is to be imaged.

From [Soh+21], an experiment with roughly similar experimental conditions, an estimate of the maximum atomic column density  $\bar{n}_z$  can be made. From Equation (3.6) we can estimate the following bare ODs for the available light:

	In-Situ	after ToF
421nm	254	2.5
626nm	561	5.6

Table 4.1: Expected bare ODs for both in-situ and after ToF imaging for 421nm and 626nm light

These estimates will be used to find a scheme, able to image atoms at these bare OD values.

#### 4.3.1 Signal to Noise Ratio for High Intensity Absorption Imaging

We will first focus on a high-intensity imaging scheme, that would allow the detection of the OD given in Table 4.1. The SNR itself is calculated as:

$$SNR(s, t; OD) = \frac{OD}{\sigma_{OD}(s, t; OD)} \quad (4.10)$$

where the  $OD$  is calculated by Equation (3.46) (or equations 3.48 in digital Counts) and  $\sigma_{OD}(s, t; OD)$  is the standard variation of that value. The variance  $\sigma_{OD}^2$  can be calculated

with a Gaussian error propagation to be [Hor+17]:

$$\sigma_{OD}^2(s, t; OD) = \left( \frac{\partial OD}{\partial C_{in}} \right)^2 \sigma_{C_{in}}^2 + \left( \frac{\partial OD}{\partial C_{out}} \right)^2 \sigma_{C_{out}}^2 \quad (4.11)$$

$$= (1 + s)^2 \left( \frac{\sigma_{C_{in}}}{C_{in}} \right)^2 + (1 + sT_{abs})^2 \left( \frac{\sigma_{C_{out}}}{C_{out}} \right)^2 \quad (4.12)$$

Where  $C_{in}$  and  $C_{out}$  are defined below Equation (3.43) and  $\sigma_{C_{in}}^2$  &  $\sigma_{C_{out}}^2$  are their respective variances. Here  $s$  and  $T_{abs}$  are defined as:

$$s(i, j) = \frac{C_{in}(i, j)}{C_{sat}} \quad (4.13)$$

$$T_{abs}(i, j) = \frac{C_{out}(i, j)}{C_{in}(i, j)} \quad (4.14)$$

where  $C_{sat}$  is the number of digital counts  $C$  at the saturation intensity  $I_{sat}$  which can be estimated to be:

$$C_{sat}(t) = \frac{t I_{sat} L_{pix}^2 \lambda Q_e}{hc F} \quad (4.15)$$

Where the first term describes the number of photons with a wavelength  $\lambda$  that arrive on the area of a pixel  $L_{pix}$  at an intensity  $I_{sat}$  over a time  $t$ . The second term determines how the number of incoming photons is converted to a number of counts due to quantum efficiency  $Q_e$  and the conversion factor  $F$  (see Equation (3.64)).

We can write the number of counts as

$$C_{in}(s, t) = s C_{sat}(t) \quad (4.16)$$

$$C_{out}(s, t) = s C_{sat}(t) T_{abs}(s, OD) \quad (4.17)$$

From the PTC analysis (see Section 4.1) we found that:

$$\sigma_{tot}^2 = \sigma_{read}^2 + \frac{1}{F} C_i + (Q_{FPN} C_i)^2 \quad (4.18)$$

Where  $C_i$  was the number of counts in an image, which allowed us to extract the read noise  $\sigma_{read}$ , the fixed pattern noise factor  $Q_{FPN}$  and the camera gain  $F[e^-/count]$  that will be used here. With this we can write the respective variances as:

$$\sigma_{C_{in}}^2(s, t) = (2\sigma_{read}^2 + s C_{sat} + Q_{FPN}^2 s^2 C_{sat}^2) \quad (4.19)$$

$$\sigma_{C_{out}}^2(s, t) = (2\sigma_{read}^2 + T_{abs} s C_{sat} + T_{abs}^2 Q_{FPN}^2 s^2 C_{sat}^2) \quad (4.20)$$

Where the factor 2 on the read noise comes from the fact that  $C_{in} = C_{probe} - C_{dark}$  and that the only noise contribution in the dark background picture is the read noise.

Finally, the variance of the OD can be identified from Equation (4.12) to be:

$$\sigma_{OD}^2(s, t; OD) = \frac{(1+s)^2}{s^2 C_{sat}^2(t)} (2\sigma_{read}^2 + sC_{sat}(t) + Q_{FPN}^2 s^2 C_{sat}^2(t)) \quad (4.21)$$

$$+ \frac{(1+sT_{abs})^2}{s^2 C_{sat}^2(t) T_{abs}^2} (2\sigma_{read}^2 + T_{abs}sC_{sat}(t) + T_{abs}^2 Q_{FPN}^2 s^2 C_{sat}^2(t)) \quad (4.22)$$

With this, the SNR can be calculated at some OD, following Equation (4.10) in dependence of the intensity  $s$  and the exposure time  $t$ .

For the vertical absorption imaging scheme, light of 421nm and 626nm is available. At the above determined expected bare ODs and the two wavelengths, the calculated SNRs are shown in Figure 4.3.

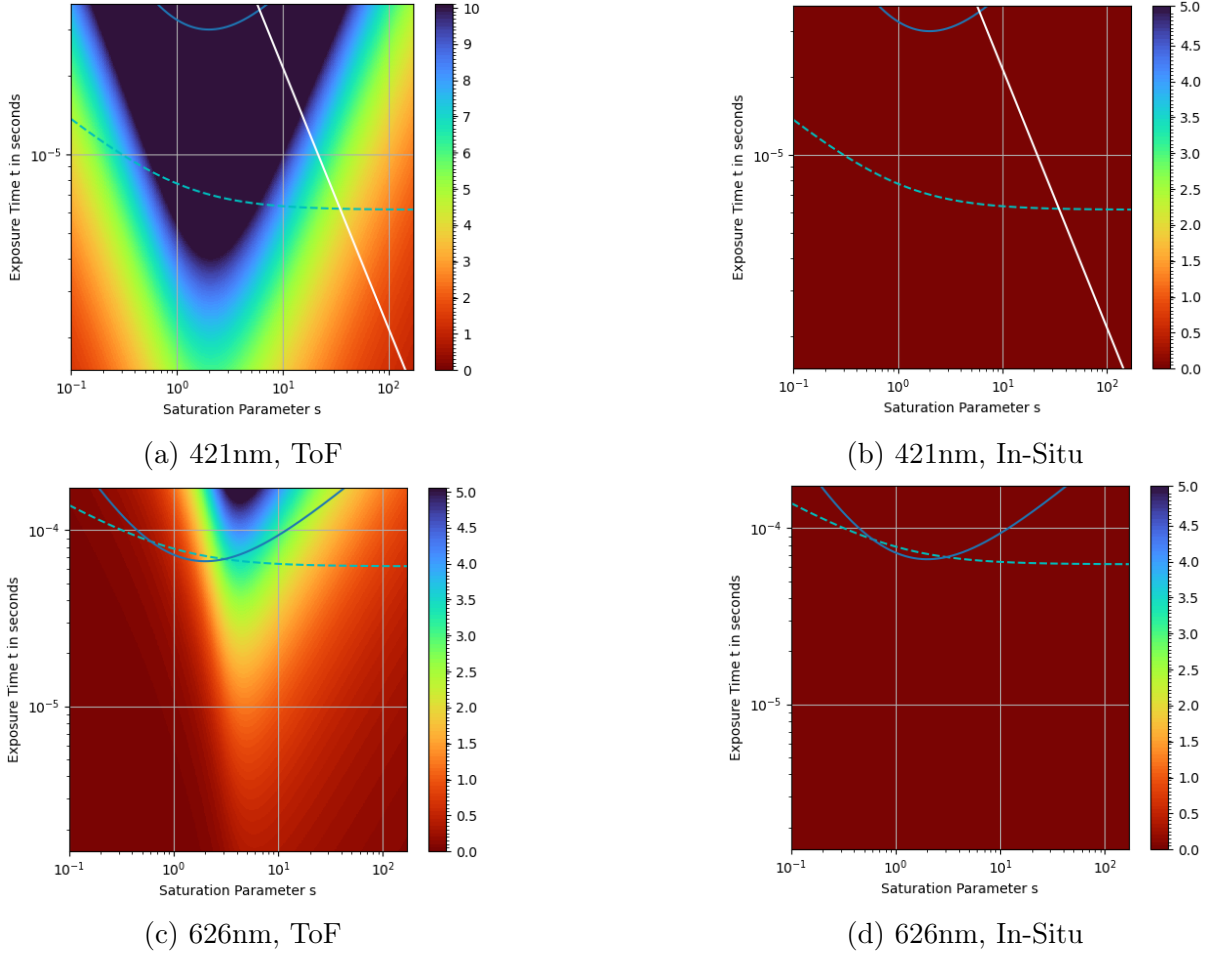


Figure 4.3: Calculated Signal to Noise Ratios (SNRs) for absorption imaging with 421nm and 626nm light. For both available wavelengths, the SNRs were calculated for the expected bare ODs in-situ and after ToF (see Table 4.1). The exposure time limits due to the displacement of the atoms, the Doppler shift and the saturation of the pixels are given by a cyan dashed line, a blue continuous line and a white continuous line respectively. The colourbar indicates the calculated SNR at each parameter set. Notice the change of colourbar scale between (a) and (b),(c),(d). Within the numerical precision used here, the calculated SNR in-situ is zero.

According to these calculations, absorption imaging will give a usable SNR for the expected bare OD in-situ, both for 421nm and 626nm light. For the images in ToF at lower bare OD, 421nm light can give a good SNR at moderate saturation and within the appropriate probe conditions found above. However, the 626nm light with a much smaller linewidth does not to be suitable for absorption imaging within the available parameter range. In the following (Section 4.6), the existing vertical absorption imaging arm will be improved to make full use of the intensity regime available.

### 4.3.2 Signal to Noise Ratio of Bright Background Dispersive Imaging

For a phase contrast imaging scheme as described in Section 3.2.2, we can carry out a similar kind of calculation. However a few differences arise due to the way, the OD is calculated from the images (see Equation (3.56)). Depending on the exact choice of imaging scheme this can change to some degree. In Faraday imaging schemes, different choices of the orientation of the polarisation filter result in imaging system with a dark or a bright background or something in between. Similarly, in a phase contrast imaging, the exact choice of the relative phase difference  $\theta$  will influence how the phase is mapped to intensity. All these choices will affect the SNR in the final imaging system. Gajdacz et al. have demonstrated however that all theses choices yield comparable SNRs leaving the choice of the exact scheme to experimental convenience [Gaj+13]. Here the SNR ratio will be estimated for a bright background Faraday imaging scheme similar to [Soh21; Soh+21]. This choice was simply made before it was decided to implement a phase contrast imaging scheme, but the results will only differ by a factor on the order of one.

For the Faraday scheme, at small dispersive phases  $\varphi$  (see Equation (3.5)), the intensity is given by [Soh21]:

$$I_{atom}/I_{probe} \approx \frac{1 + \varphi}{2} \quad (4.23)$$

Within this approximation, we can again find the phase from a set of three different pictures.  $C_{probe}$  and  $C_{back}$  will again be the digital count without atoms and without light, while  $C_{atom}$  will be the count of the interference pattern caused by the phase  $\varphi$ . We will again define  $C_{in} = C_{probe} - C_{back}$  and  $C_{out} = C_{atom} - C_{back}$

We can also again define a transmittance

$$T_{disp} = I(\varphi)/I(\varphi = 0) = 1 + \varphi \quad (4.24)$$

however as the intensity is now given by an interference effect, rather than by absorption, this transmittance must not necessarily be smaller than one.



With this definition we can recognise, that

$$\varphi = \frac{C_{out} - C_{in}}{C_{in}} \quad (4.25)$$

which allows us to find the SNR

$$SNR_{OD} = \frac{OD}{\sqrt{\sigma_{OD}^2}} \quad (4.26)$$

with

$$\sigma_{OD}^2 = \left( \frac{\partial OD}{\partial C_{in}} \right)^2 \sigma_{C_{in}}^2 + \left( \frac{\partial OD}{\partial C_{out}} \right)^2 \sigma_{C_{out}}^2 \quad (4.27)$$

$$= \left( \frac{4\Delta}{\Gamma} \frac{T_{disp}}{C_{in}} \right)^2 \sigma_{C_{in}}^2 + \left( \frac{4\Delta}{\Gamma} \frac{1}{C_{in}} \right)^2 \sigma_{C_{out}}^2. \quad (4.28)$$

Where  $\Delta$  is the detuning and  $\Gamma$  the linewidth. Thus with the results from the PTC analysis, we can again write the total noise in  $C_{in}$  and  $C_{out}$  in units of digital counts as:

$$\sigma_{C_{in}}^2(s, t) = (2\sigma_{read}^2 + sC_{sat} + Q_{FPN}^2 s^2 C_{sat}^2) \quad (4.29)$$

$$\sigma_{C_{out}}^2(s, t) = (2\sigma_{read}^2 + T_{disp}sC_{sat} + T_{disp}^2 Q_{FPN}^2 s^2 C_{sat}^2) \quad (4.30)$$

And the variance is then given by:

$$\begin{aligned} \sigma_{OD}^2(\Delta, s, t) &= \left( \frac{4\Delta}{\Gamma} \frac{T_{disp}}{sC_{sat}} \right)^2 (2\sigma_{read}^2 + sC_{sat} + Q_{FPN}^2 s^2 C_{sat}^2) \\ &+ \left( \frac{4\Delta}{\Gamma} \frac{1}{sC_{sat}} \right)^2 (2\sigma_{read}^2 + T_{disp}sC_{sat} + T_{disp}^2 Q_{FPN}^2 s^2 C_{sat}^2). \end{aligned} \quad (4.31)$$

And the SNR of a bright background dispersive imaging scheme at small  $\varphi$  may be estimated to via Equations (4.26) and (4.31). To keep the dispersive phase small enough to have an approximately linear relationship with the intensity, detunings (in units of  $\Gamma$ ) of about half the bare OD are needed (see Equation (3.5)). Due to the large linewidth of the 421nm transition, reaching these large detunings is not easily possible for expected bare ODs around 100. For the 626nm transition, reaching detunings of hundreds of linewidth is easily done with a single AOM. The following calculations will therefore only consider the 626nm light as it is much better suited for far off resonance imaging and they are shown in Figure 4.4.

For these calculations, the detuning is kept above  $\Delta > 10\Gamma$ , to keep the effect of the phase  $\epsilon$  small compared to  $\varphi$  (see Equations 3.5,3.6). For bare ODs in the single digits, phase contrast imaging then results in limited SNRs. At very large OD however very high SNRs can be reached.

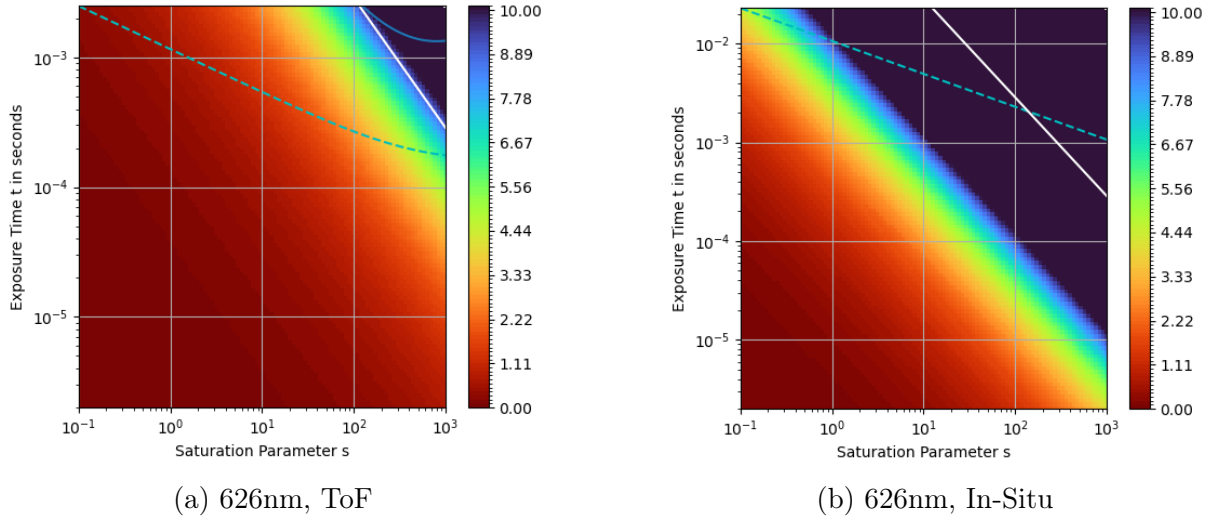


Figure 4.4: Calculated Signal to Noise Ratios (SNRs) for dispersive imaging at 626nm light. The SNRs were calculated for the expected bare ODs in-situ and after ToF (see Table 4.1). The exposure time limits due to the displacement of the atoms, the Doppler shift and the saturation of the pixels is given by a cyan dashed line, a blue continuous line and a white continuous line respectively. The colourbars indicate the SNR at a parameter set.

### 4.3.3 Choice of Suitable Imaging Scheme

From the above results it was decided to keep and improve the vertical absorption imaging arm at 421nm. By increasing the intensity of the imaging beam, high SNR absorption imaging within the appropriate probe conditions can be expected as long enough intensity is available (up to  $s = 100$ ) and as long as the bare OD is not too large (below  $\sigma_0 \bar{n}_z = 100$ ).

At the same time, for imaging very large atomic densities a dispersive imaging scheme for 626nm light was designed. Dispersive imaging will also have the advantage of being non-destructive so that many pictures of the same atomic cloud may be taken in succession. The ability to tune the detuning over a large range should make this an attractive, versatile imaging scheme. Both the design of a dispersive imaging scheme (Section 4.5) and the improvements to the absorption imaging scheme (Section 4.6) will be described below. A simulation that was written to aid the design of a phase contrast imaging scheme, will be introduced in the following section.

## 4.4 Simulating Phase Contrast Imaging

In order to be able to explore different imaging techniques, especially phase-contrast imaging, the propagation of an arbitrary beam through a system of optical components was simulated. This was used to verify the functionality of a phase spot in general and to aid the design of a specific phase spot. Although calculating the waist of a Gaussian

beam after a lens or during free space expansion may even be done by hand using rather simple formulas [ST91a], calculating the evolution of a complex light field of arbitrary shape through different optical elements requires rather more computational power and some more thought.

The simulation written for this thesis is based on Fourier optics and is able to take a beam/ light field of arbitrary (space-dependent) intensity and phase and to simulate (among others) the following :

1. free space propagation
2. effect of an aperture
3. effect of a (thin) lens
4. effect of a phase spot

Thus, the simulation allows one to define an input field of arbitrary intensity and phase and let it propagate through the desired optical system. The ability to let the field acquire space-dependent phases and magnitudes allows one to simulate absorption imaging and phase contrast imaging.

### **Simulating free space propagation**

The propagation in free space is simulated as described in Section 3.1.2. By taking the Fourier transform of an arbitrary light field in the input plane, multiplying it with the transfer function of free space and calculating the inverse Fourier transform of that product, the propagation of any light field to some output plane can be simulated. It was verified, that the propagation yields expected results such as Fraunhofer diffraction and the evolution of a Gaussian beam.

### **Simulating an aperture**

An aperture can simply be implemented by setting the value of the complex field to zero in certain regions of the simulated space. The simulation verifies that effects such as airy rings etc. follow directly from a subsequent free space propagation as described above.

Similarly one might simulate absorption in an atomic cloud, by reducing the intensity of the field according to the Lambert-Beer law for the local density of the atomic cloud.

### **Simulating a lens as an imprinted phase**

This paragraph and the next cover two different possibilities of doing so, each with their (dis-)advantages.

One way to approach this problem may be to imprint a space-dependent phase factor onto the beam just as a real lens would. The phase shift  $\Delta\varphi$  caused by a thin lens centred in the  $x,y$  plane around  $(x,y)=(0,0)$  on a monochromatic beam may be described as [ST91d]:

$$\Delta\varphi(x, y) \approx \exp \left[ i k_0 \frac{x^2 + y^2}{2f} \right] \quad (4.32)$$

where  $i$  is the imaginary unit,  $k_0$  the (free space) wavenumber,  $f$  the focal length of the lens and  $x, y$  are the spacial coordinates.

To simulate a field propagating through a lens at  $z = z_{lens}$  (where  $z$  is the direction of beam propagation), one only has to multiply the incoming field with this (imaginary) factor at each position  $(z_{lens}, x, y)$  of the wave and let the wave propagate through the free space after the lens.

This method has the **advantage** that one may propagate the field to any distance such that it allows one to place arbitrary apertures at arbitrary positions like directly before or after the lens and it may work quite well if the focal length of the lens is not too short, i.e. if the imprinted phases aren't too big. However it has the **disadvantage**, that one might have to define a very large grid with a very small grid size to be able to use 'short' focal lengths and/or large magnifications.

For lenses as will be used here, with a 2 inch aperture and focal lengths around 10cm, the gradients of imprinted phases become quite large, and one has to choose an extremely small step size in the simulation to achieve smooth phase shifts in the field. If the grid size in the simulation is too small and the step size too large the difference in phase between two adjacent pixels becomes large, the field becomes strongly pixelated and the simulation breaks down. Taking a Fourier transform of a field, which has a (strongly varying and) strongly pixelated phases, results only in nonsensical outputs that have some kind of square symmetry, representing the pixels in the grid. From experience, it seems that using a simulation grid, that is 3 times longer than the largest waist a Gaussian beam will acquire while propagating the system is usually sufficient not to get noticeable aberrations from the non-infinite grid size. Then the step size has to be adjusted that both intensity and phase varies smoothly over the whole grid.

If one wants to work with large magnifications, this can become problematic, as during part of the propagation most of the grid will be empty, while nearly all of the beam (and thus most of the phase information) will be squeezed into a few pixels. This strongly limits the accuracy and dictates the use of very small step sizes. Ultimately, the performance of the computer sets the limit to the usability of this method.

## Simulating a lens via its Fourier Transform Properties

Another method to simulate the transmission through a lens is to exploit the property that the field in the back focal plane of a lens is exactly the Fourier transform of the front

focal plane of that lens (see discussion in 3.1.2). Thus, simulating the propagation through a lens is as easy (and computationally efficient) as taking a single Fourier transform of the input field. The only care has to be taken when transforming the output coordinates accordingly. As can be seen in Equation (3.29), the output field is proportional to the Fourier transform  $\mathcal{F}(x/\lambda f, y/\lambda f)$ . Thus after taking the Fourier transform of the field in the front focal plane, the coordinates in the back focal plane are rescaled. This scaling can be compensated by rescaling the step size  $\Delta x$ . The new step size is:

$$\Delta x' = \frac{\Delta k_x}{\lambda f} \quad (4.33)$$

where  $\Delta k_x$  is the step size of frequencies in the Fourier transform. As symmetrical grids were used in this simulation, where  $\Delta x = \Delta y$  the same scaling applies to both axes.

The **disadvantage** of this method is, that the beam propagation can only be simulated from exactly the front focal plane to exactly the back focal plane. To simulate optics that are a short distance out of focus, one may do a subsequent free space propagation (forward or backwards of the light propagation direction). Simulating optics far out of focus (like an aperture at the position of the lens however, is not practical with this method.

### Simulating the effect of a phase spot

To simulate a phase spot, an additional phase was simply added within the radius of the phase spot. To understand the importance of homogeneity of the phase spot, a degree of random noise could be added to the phase imprinted by the spot.

Also, showcasing the functionality of a phase contrast imaging scheme, the Figure 3.6 taken from Meppelink et al. [Mep+10] could be replicated (see Figure 4.5). The simulation was used through the design of the phase contrast imaging scheme, to determine appropriate parameters.

## 4.5 Design of new Phase Contrast Imaging Setup

The specific design of a phase spot for phase contrast imaging depends on the specific requirements and characteristics of the imaging system in which it will be employed. Specifically, the depth of the phase spot will of course depend on the required phase shift and on the wavelength, that is to be shifted. The size of the spot will depend on the waist of the beam in the Fourier plane. Here, the chosen geometry depicted in Figure 4.6.

For the implementation of a phase contrast scheme it is not relevant whether the ‘spot’ itself is a small indent into or an extrusion out of a substrate. If a spot is chosen

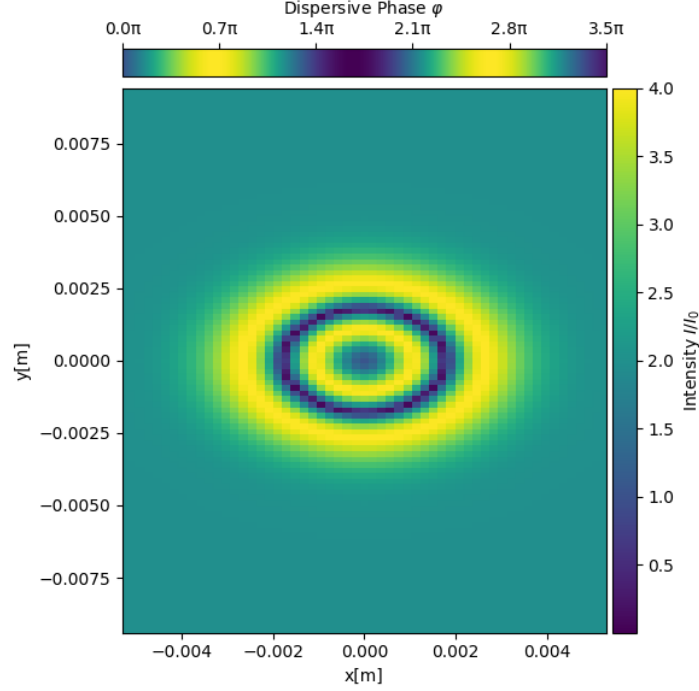


Figure 4.5: Simulation of a phase contrast image using a phase spot. The phase spot causes a  $\pi/3$  phase shift between atom beam and probe beam. An atomic cloud was approximated to having a Gaussian distributed surface density. In the center, this cloud imprints the dispersive phase  $\varphi = 3.5\pi$ . The oscillating intensity pattern is due to the intensity dependence given by Equation (3.57)

to be a small extrusion from the substrate, the phase of the ‘probe beam’ ( $E_{probe}$ ) will be advanced compared to the rest of the beam ( $\theta > 0$ ). In this case a negative detuning of the imaging light will cause the atomic density to imprint positive phases  $\varphi$  on the light (see Equation (3.5)) and the intensity will be roughly linear with  $\varphi$  for small  $\varphi$ . For technical reasons, etching a small recess into a substrate was found to be more precise. In this case the phase of the probe beam will be retarded compared to the rest of the beam ( $\theta < 0$ ) and a positive detuning of the imaging beam should be chosen. The intensity of the light in the imaging plane is then given by Equation (3.57) and depicted in Figure 3.5. It will again be linear with intensity for small phases, but in this case  $I \propto -\varphi$ .

The substrate that will contain the phase spot is a 2” fused silica window [Cor25]. A surface finish of  $\lambda/20$  was chosen after the surface flatness was determined to be sufficient in a simulation. At a wavelength of 626nm fused silica has a refractive index of  $n = 1.45724$ . Thus, to reach a phase retardation of  $\theta = -\pi/3$  a 228nm deep recess has to be etched into the substrate. Different manufacturers were contacted and finally (only) *HOLOEYE Photonics AG* agreed to manufacture such a spot, who had previously manufactured a very similar phase spot for the group Oberthaler group in Heidelberg (see [Joo13]). The manufacturer estimated that the depth of the spot can be manufactured to a precision of  $\pm 10\text{nm}$ , while the transition zone (see Figure 4.6) was estimated to be

at an angle of below  $10^\circ$ , which may reduce the radius of the spot by 40nm.

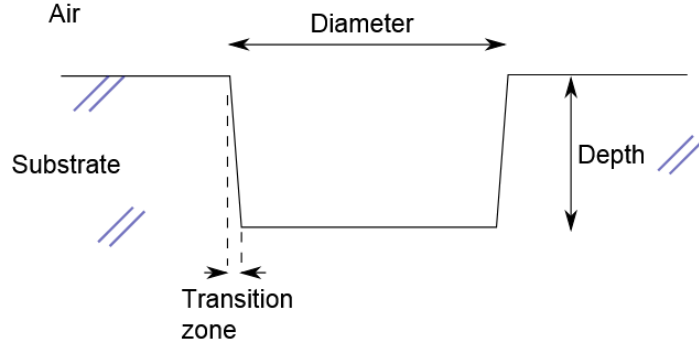


Figure 4.6: Schematic of a phase spot consisting of a small recess or ‘dip’ in a larger substrate. The left side shows a side view, cut through the center of the phase spot itself. The etching process results in a certain ‘transition zone’ around the spot. The right side shows the position of the recess on the substrate. Figure adapted, taken from [Joo13]

The radius of the phase spot should of course be sufficiently larger than the waist of the focussed probe beam ( $E_{probe}$  in Figure 4.7), such that ‘all’ of the probe beam is phase shifted against the diffracted part of the beam, also called atom beam ( $E_{atom}$  in Figure 4.7). At the same time the phase spot should be small enough as not to disturb the atom beam and to allow for some margin of error in the alignment of the phase spot to the beam. The waist of a beam depends on the focal length of the lens, that focusses the beam. In the vertical absorption imaging setup of BoDy, the first Fourier plane is not accessible, as the focal plane of the objective is mere millimetres behind the objective optics [Phi23]. To get access to a second Fourier plane, where a phase spot may be employed, a second 4f-setup can be build behind the first and the phase plate containing the phase spot may be placed in the Fourier plane of the second 4f-setup (see Figure 4.7). The focal lengths of the lenses were chosen due to the constraints of the optical table to be  $f_2=400\text{mm}$ ,  $f_3=300\text{mm}$  and  $f_4=500\text{mm}$ . This results in an overall magnification of  $M=20.7$ .

To determine an optimal radius the formation of an image was simulated for phase spots of different radii. The image of a test object contains sharp features with sizes similar to the atomic cloud that is to be imaged in experiment. The prominence of these peaks (given by the difference in local background intensity and peak intensity) may thus give an indication on the expected contrast in the atomic images. The prominences are plotted for a range of different phase spot radii in Figure 4.8.

The prominence for a spot radius of  $4\mu\text{m}$  is significantly below that of an  $8\mu\text{m}$  spot. This reduction in contrast is expected to happen when the size of the phase spot becomes smaller than the waist of the focussed beam and no phase shift is applied to a significant part of the probe beam. For larger radii the contrast remains more or less constant, while at phase spot sizes larger than  $36\mu\text{m}$  the atom beam  $E_{atom}$  begins to be affected,

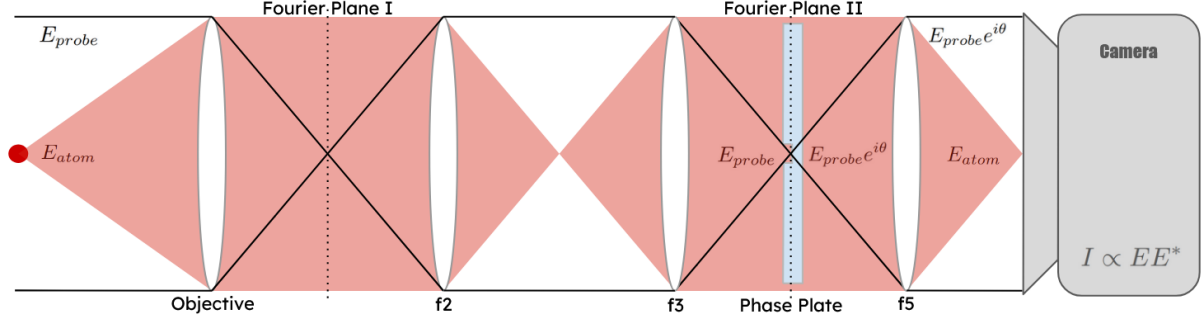


Figure 4.7: Position of the phase in a second 4f setup. The Fourier plane of the objective is not accessible due to the actual size of the objective (not shown here, see Figure 4.10). The objective and lens f1 make up one 4f-setup, while the lenses f2 and f3 make up the second 4f-setup. Imaging beam illuminating the atoms is depicted with black outlines ( $E_{probe}$ ) while the part of the beam that is diffracted at the atoms is depicted in red ( $E_{atom}$ ). The phase spot is expected to only introduce a phase shift  $\exp[i\theta]$  to the probe beam. The image is formed by interference of the two beams where the total field is given by  $E = E_{probe} + E_{atom}$ .

distorting the image. These distortions can be seen in Figure 4.8, where the intensity varies over the peaks. In conclusion, the actual size of the phase spot seems not to be very critical as long as the focussed probe beam is not cut too much. The more stringent constraint on the phase spot size will be one's own ability to position the focal point of a beam with a waist of a few microns onto an equally small phase spot. Comparing to other phase spot designs [Joo13; Mep+10; Sad06; And+97] in which spot radii ranging from 25 $\mu\text{m}$  to 250 $\mu\text{m}$  were used it was decided to order two phase plates, one with a spot radius of  $r_{spot} = 25\mu\text{m}$ , one with a spot radius of  $r_{spot} = 50\mu\text{m}$ , both on a 2" fused silica substrate.

Unfortunately, due to a combination of a process deviation and a handling error, the manufacturing of the smaller spot was delayed. The larger spot was successfully manufactured and the depth of the spot was measured by *HOLOEYE* using white light interferometry to be 229 $\mu\text{m}$  (see Figure 4.9). This results in an only 0.4% larger phase  $\theta$ , which should have no significant effect.

As an anti-reflection coating needs to be applied to both phase plates, it was decided to wait until the smaller spot was remade so that both can be coated and afterwards delivered together. As the phase plates were not received to this day, the implementation of the phase contrast imaging system did not yet proceed.

## 4.6 High Intensity Setup and Beam Shaping

Instead, the existing absorption imaging setup was upgraded to improve both the resolution and to enable the imaging of dense atomic clouds in-situ. The resolution was improved by properly aligning the absorption imaging system, which consists of a custom



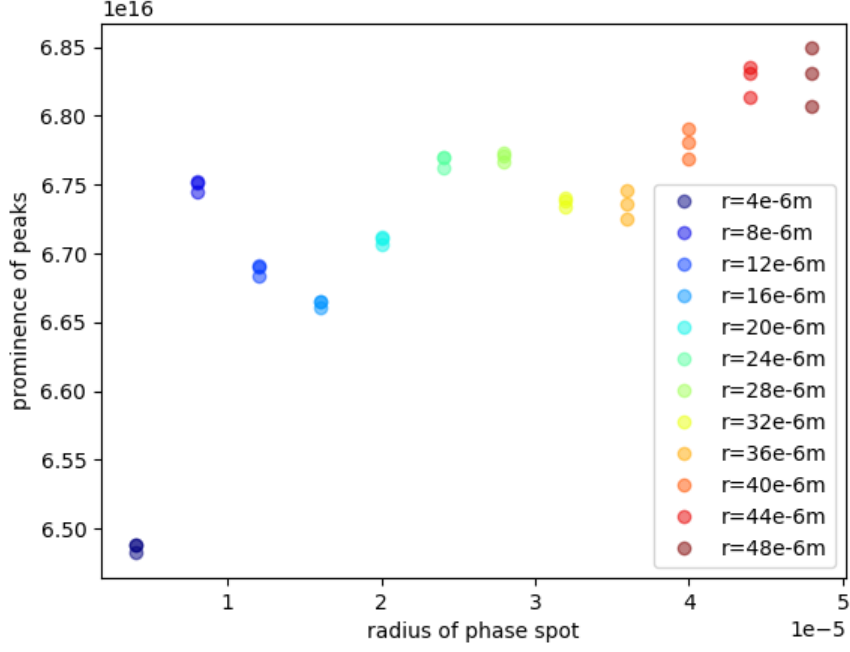


Figure 4.8: Simulated prominence of intensity peaks for different phase spot sizes. Multiple points at one radius correspond to multiple intensity peaks within one image. The radii are given in meters, the prominences in arbitrary units.

high resolution objective and a tube lens in a 4f-configuration. The alignment procedure is described in the next section.

Before aligning the imaging arm, a new smaller beam waist was chosen for this arm to increase the intensity on in the object plane. From the results of sec.4.3, an intensity range of  $s = 0.5I_{sat} \rightarrow 50I_{sat}$  in the object plane was thought to be optimal. By setting the maximum intensity to be around  $s = 50I_{sat}$  the saturation of bright background pixels can be avoided, while a single AOM enables the imaging parameters to be tuned, providing a versatile high SNR imaging system for ODs in the single digits and below.

The available optical power of the 421nm laser in the imaging arm was measured to

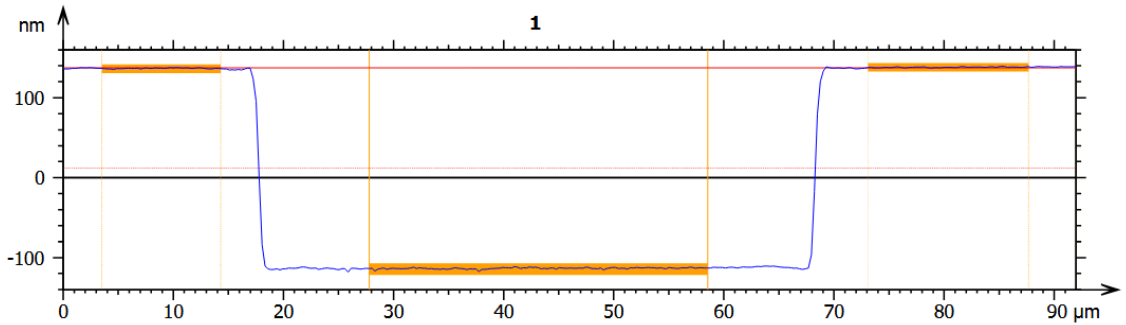


Figure 4.9: White light interferometry measurement of the depth of the  $r_{spot} = 50\mu\text{m}$  phase spot. The mean depth within the coloured section in the spot itself is 229nm. Measured by *HOLOEYE Photonics AG*

be  $P_{img} = 2.5\text{mW}$ . To reach a saturation of  $s = I/I_{sat} = 50$  with this little power, a beam width of around  $240\mu\text{m}$  would be needed in the object plane. To achieve a simple imaging system with a small beam waist on the order of a few hundred  $\mu\text{m}$  different available collimators in the 60FC and 60FC-SF series from Schäfter+Kirchhoff [Oec25] where tested. The tested collimators featured focal length from 6.2mm down to the shortest focal length available of 4.0mm, where a shorter focal length corresponds to a smaller waist of the collimated beam.

The 60FC-SF series feature a ‘super-fine’ adjustment screw that allows for a more precise setting of the focus. Without this 0.35mm thread pitch adjustment screw a precise setting of the focus was experienced to be highly challenging and not well reproducible and the collimators of the 60FC series where ruled out.

Within the 60FC-SF series, the collimator with the shortest focal length of 4.5mm was chosen to be installed into the imaging arm. The beam was focused onto the position of the atoms, around 250mm away from the collimator, which yields a waist of around  $w_0 = 300\mu\text{m}$ .

In a test setup, the width of a beam was measured at various positions after the collimator of 4.5mm focal length. The beam was collimated by using a shear plate positioned about 250mm away from the collimator and the resulting expansion can be seen in Figure 4.10 (bottom). With the thus found values for the waist and focal point of the beam, the expansion in the imaging arm was calculated following Gaussian optics (see [ST91a]). In Figure 4.10 (top) the evolution of the width of the beam through the optical system can be seen, where the shaded colours indicate the radius of  $1w$ ,  $2w$  &  $3w$  where  $w$  indicates the width of the beam where the intensity has fallen off by  $1/e^2$ . Evidently, even such a small beam expands quite significantly after the objective. The  $2''$  lens 782.2mm away from the objective is just large enough not to cut the beam below  $3w$ .

With a beam of waist  $w_0 = (305 \pm 2)\mu\text{m}$  a saturation of  $s = 30$  can be expected. This is still large enough to enable a versatile vertical absorption imaging arm. To increase  $s$  further, a little more power will have to be distributed to the imaging arm or the loss of power in the arm itself, due to beam splitting and dichroic optics, would have to be reduced.

## 4.7 Alignment of a 4f Setup

During the adjustment of the high intensity absorption imaging system, the whole 4f setup needed to be aligned to bring the atoms and the camera into focus. This proved to be challenging, as the microscope objective has a depth of field of only  $0.3\mu\text{m}$  [Phi23] and the alignment of objective, tube lens and camera is coupled. Misalignment of either one may be somewhat compensated by any other element, however the lowest optical aberration may only be found in the optimal setup. The process can be improved, by

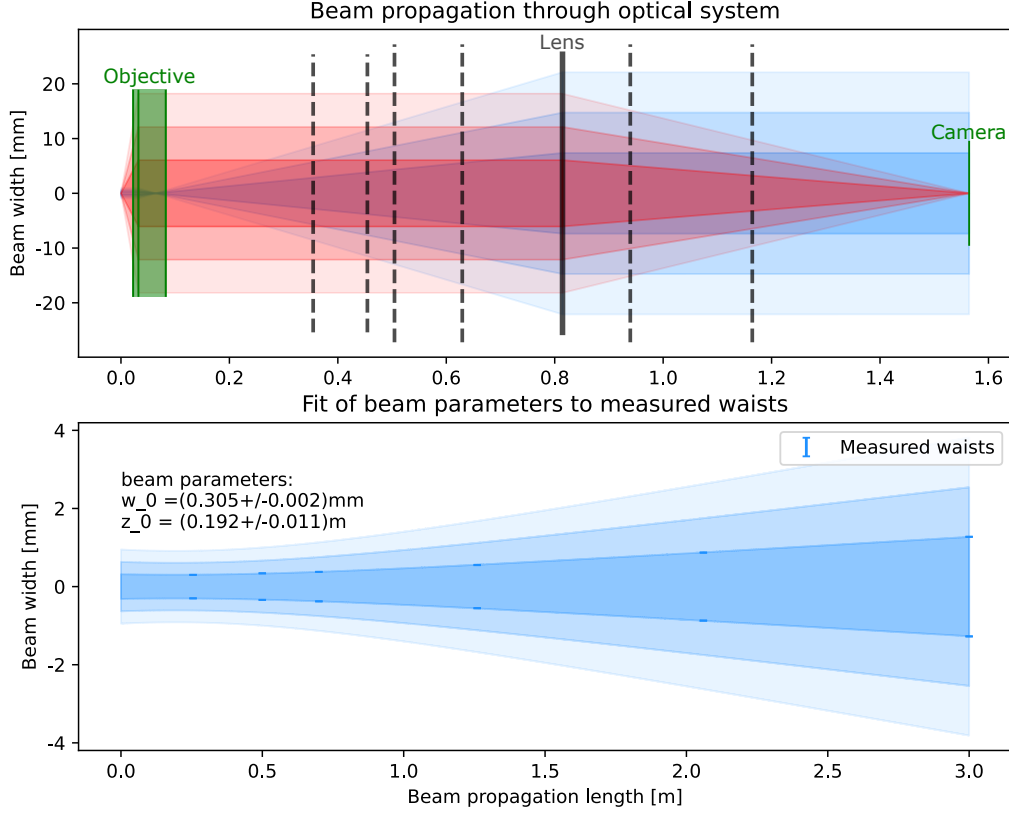


Figure 4.10: Bottom: Least squares fit to measured beam widths. A beam waist of  $w_0 = (305 \pm 2)\mu\text{m}$  and a focal point at  $(192 \pm 11)\mu\text{m}$  were found. Top: Evolution of the width  $\omega(z)$  for a Gaussian beam of these parameters (blue) through the vertical imaging system of BoDy. In red, light that scatters in the object plane and that can be collected by the objective is indicated. The dashed lines indicate the sizes and positions of different mirrors in the imaging arm. Both: Three different intensity shades indicate the radius of  $1w, 2w$  and  $3w$ .

decoupling the alignment of the tube lens and the alignment of the objective.

First of all, we note (as explained in Section 3.1.4) that the distance between objective and tube lens does not actually matter in an absorption imaging system. Thus one ‘only’ has to align the objective to the atoms and the tube lens to the camera. The distance between objective and tube lens can then be chosen more or less freely, according to the experimental constraints, without the need for precise alignment.

In our case, where the objective of 32.2mm focal length has a very short depth of field, while the tube lens of 750mm has a much larger depth of field, the needed precision for the alignment of the tube lens is far smaller.

The allowable misalignment of the tube lens was estimated in a simulation. For a 4f-setup of the same parameters, the tube lens was misaligned by an increasing amount. Using a USAF1951 resolution test chart as an input intensity pattern, where the smallest

structure (group 1,6) has a line width of about  $2.5\mu\text{m}$  in the atom plane, the defocus of the tube lens was simulated and the loss of resolution was visually probed.

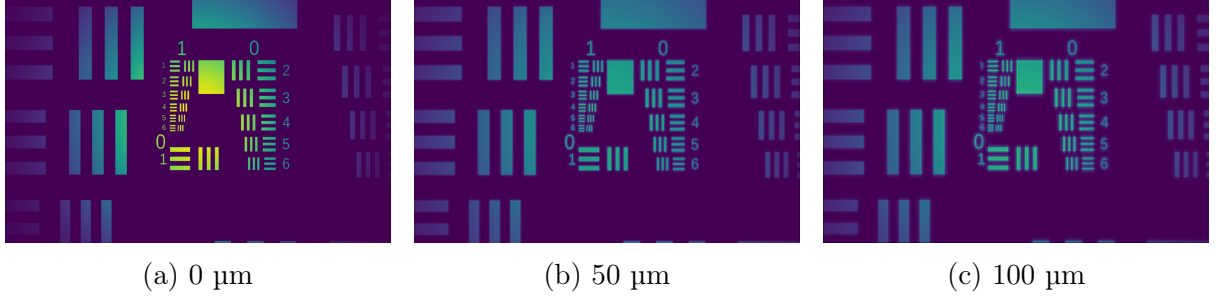


Figure 4.11: USAF1951 resolution test chart with a smallest line width of  $2.5\mu\text{m}$  in group 1,6 in a 4f-setup with  $M=23.3$ . The 750mm tube lens was misaligned by  $0\mu\text{m}$ ,  $50\mu\text{m}$  and  $100\mu\text{m}$

As this imaging system will be used to investigate supersolid states with density modulated features on the order of a few microns and to be able to use the full resolution of about  $0.5\mu\text{m}$ , the loss of resolution for a  $50\mu\text{m}$  displacement was deemed as a limit.

Thus if the tube lens can be aligned within  $50\mu\text{m}$  precision to the camera, the objective may then be aligned by focusing small structures in a camera image. However, reaching a  $50\mu\text{m}$  precision on a distance of  $750\text{mm}$  is still a challenging task.

#### 4.7.1 Alignment of 4f-setup with a large Gaussian beam

One way to precisely position the tube lens compared to the camera is by focussing a large Gaussian beam to the smallest possible waist with the tube lens. By moving the camera to the position where the width of the beam is smallest, that is where the beam profile on the camera screen is smallest, the camera can be brought into the focal plane of the lens. The resolution achieved is then on the order of the Rayleigh range of the focussed beam.

Two issues arise however. First of all, the large beam need to be collimated very well, which is to say, the lens has to be placed more or less exactly at the beam waist. The notion of ‘more or less’ is specified by the Rayleigh length of the beam. For a Gaussian beam with large waist, the Rayleigh length can be huge (for a  $20\text{mm}$  Gaussian beam at  $421\text{nm}$  it is around  $3\text{km}$ ). That means that the placement of the lens relative to actual beam waist does not have to be all that precise at all! However, the issue remains at collimating such a beam. Without being able to measure the beam width at different positions over the range of the Rayleigh range itself (which can be several kilometres), it is not easy to find its waist or to be able to tell where it actually is collimated.

Another issue is that with a  $750\text{mm}$  lens even a  $20\text{mm}$  beam cannot be focussed down such that its Rayleigh range is small to allow for a  $50\mu\text{m}$  precision. This can be seen in a basic calculation for the width of a Gaussian beam (see Figure 4.12).

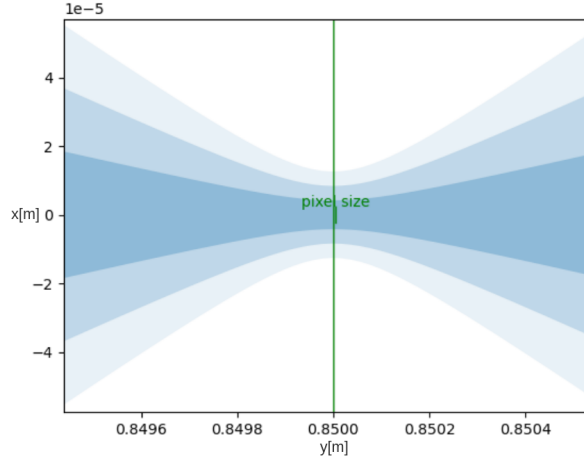


Figure 4.12: Width  $\omega(y)$  of a 24mm Gaussian beam, focussed by a 750mm lens

The waist of the focussed beam is 4.2μm and it about doubles after 250μm. That means that the beam diverges from a spot with a radius at  $1/e^2$  Intensity of just around 1 pixel to a radius of around 2 pixels, 250μm away from focus. Thus finding the focus point within a precision of 50μm can be quite challenging.

#### 4.7.2 Alignment of 4f-Setup with a Bahtinov-type mask

Instead of finding the focal plane of a large Gaussian beam, one can also exploit the property of a lens that the Fourier transform of the field in the front focal plane can be found in the back focal plane. Thus a mask with a pattern that has a known and recognisable Fourier transform may be placed in front of the lens and the focal plane will be found there, where the Fourier transform of the mask pattern is visible. This can be expected to yield a greater precision in alignment, as the structures in an optical Fourier transform will diverge faster than a Gaussian beam.

In the beginning of the 20th century masks with holes at specific locations where developed by Hartmann [Har04], which could be used to map out aberrations in astronomical telescopes and to bring them into focus. Following along similar ideas Bahtinov presented a specific mask design as a focusing aid for amateur astronomers in an online forum [Bac05]. This kind of mask seems to have gained quite some popularity among (amateur) astronomers and sparked different, similar kinds of designs [Car09].

As the mask is intended to be used on focusing telescopes on stars, which are dim point-like sources of white light, a mask as presented by Bahtinov can be quite helpful (see Figure 4.13).

The use of grids at three different angles, as presented by the Bahtinov mask in Figure 4.13, serves the dual purpose of 1) allowing enough light of a dim light source through the mask to the sensor and 2) having an *asymmetric* Fourier transform. As can be seen in Figure 4.13, the Fourier image (the 2D Fourier Transform of the image) of the mask is

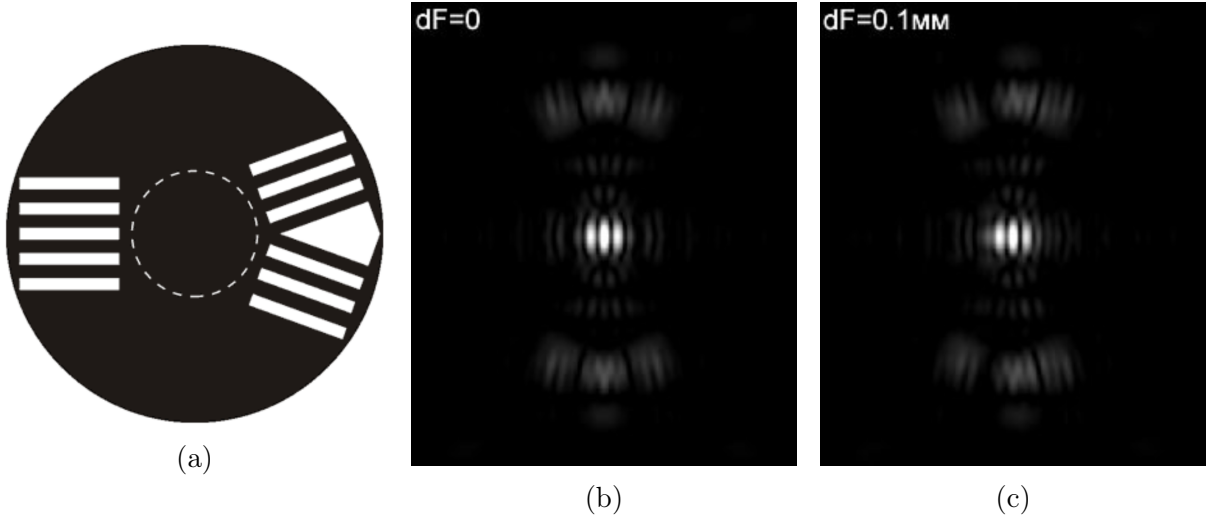


Figure 4.13: (a) Original Bahtinov Mask with simulations of the observed pattern on a screen (b) in focus and (c) out of focus by  $100\mu\text{m}$ . Figures adapted from [Bac05].

only symmetric in the focal plane, but starts to tilt away from this position as the screen moves out of focus.

In a cold atom experiment a similar kind of mask may be used, however it should be adapted as very different light sources are available. First of all, the use of white light may cause chromatic aberrations in the Fourier image, which are actually rather helpful in the case of astronomy. In our case however, we can illuminate a mask with monochromatic laser light of comparatively arbitrary intensity. That means, while a similar arrangement of angles may be kept in a mask design to form an asymmetric Fourier image, the grids can be replaced by single slits. While the Fourier image of a finite grid consists of points of decreasing intensity, the Fourier image of a slit is again a line, which will be helpful in trying to focus our system.

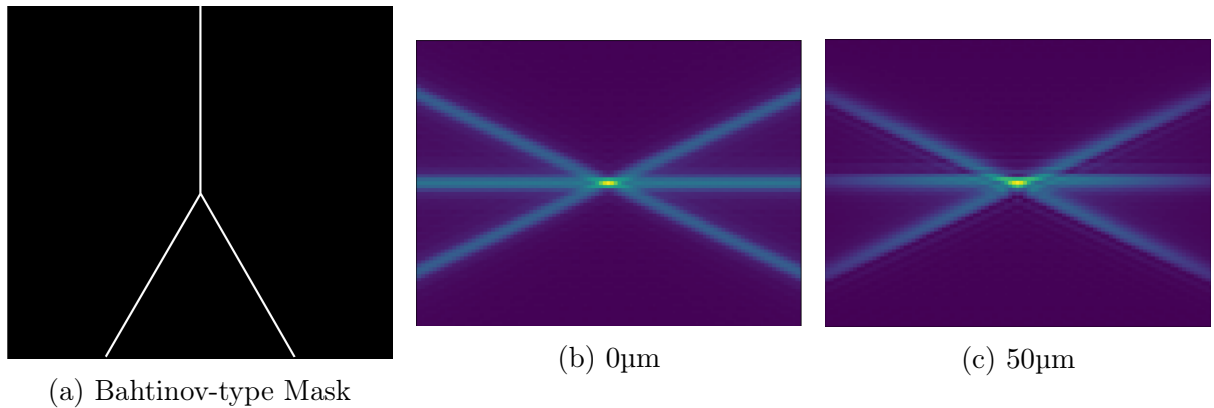


Figure 4.14: (a) Adapted Bahtinov-Type Mask with the observed pattern on a screen (b) in focus and (c) out of focus by  $50\mu\text{m}$  simulated with using the propagation algorithm presented in Section 4.4.

Figure 4.14 shows the adapted Bahtinov-type mask that was designed and used for

aligning the tube lens in this thesis. The simple pattern of three slits forming a Y shape, where the lower two slits meet at a  $30^\circ$  angle, produces a Fourier image of three lines intersecting in one point. If the screen is displaced from the focal plane of the lens by even a small amount, the central line is displaced against the other two lines that are forming an X shape (see Figure 4.14c).

Due to the nature of the Fourier transform, the Fourier image will have some degree of modulation due to the finite aperture of the mask. The size of the pattern itself in the Fourier plane is determined by the width of the slits in the mask. Here, as the tube lens in question has an aperture of  $2''$ , all masks shared that same aperture. In this case the pattern-modulation due to the aperture was of no concern.

The smaller the slits are (up to Abbe's limit) the longer the pattern will appear in the Fourier plane. After simulating and experimenting with Bahtinov-type masks of different slit widths, the smallest slit that could be manufactured with a width of  $100\mu\text{m}$  was found to work best. In fact, for a slit of such small size at an aperture of  $2''$  and a  $405\text{nm}$  laser of around  $20\text{mm}$  waist and around  $1\mu\text{W}$  power, the pattern is so large that it is easily visible by eye and can serve as a rough positioning guide for the camera already.

Figure 4.15 shows a mask that was used for the alignment of the tube lens and exemplary images in and out of focus by a few hundred micrometers. This should illustrate how the misalignment of the lens can be seen in the Fourier plane. With a high resolution camera and a fitting algorithm, to quantify the displacement of the centre line in the Fourier image, an alignment within tens of micrometer was achieved.

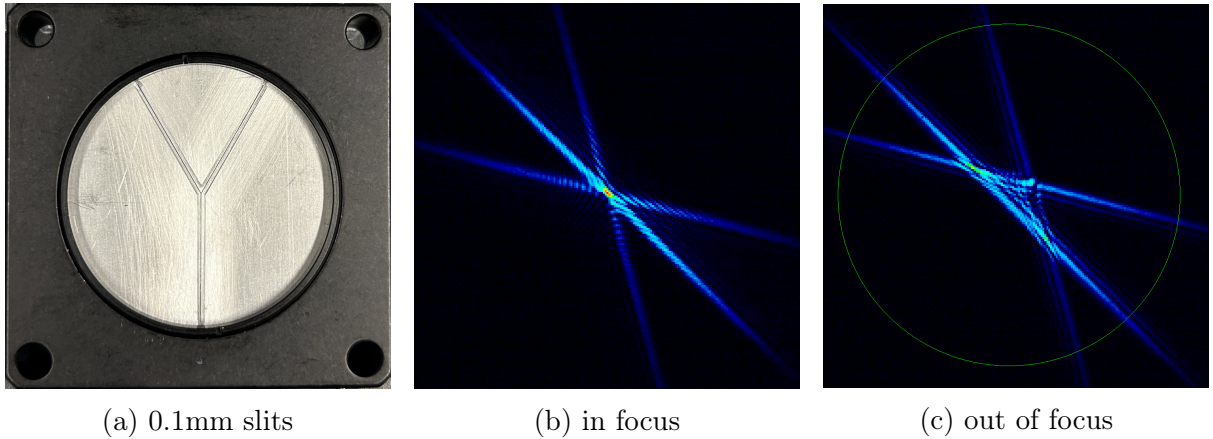


Figure 4.15: (a) Bahtinov-type mask with 0.1 mm slits that was used to align the tube lens of a 4f setup. Notice the small 0.1mm slits in a larger groove. The measured intensity in the Fourier plane when the tube lens is in focus (b) and out of focus (c).

A large beam is again helpful for precise alignment and the alignment is again critically dependent on the collimation of the beam. While this problem cannot be circumvented by the Bahtinov-type alignment tools, this method proved to serve as a good initial alignment of the tube lens. From there, the objective can be focussed on small structures

in the object plane. In practice a beam of  $25\text{mm}$  waist was used and collimated with a shear plate.

Prior to this effort the collimation and intensity of the imaging beam was unclear and the 4f-setup was not well aligned. Neither the ideal position of the objective, nor of the tube lens were known and the alignment of both was done in the image plane on the camera. In such an alignment their positions are coupled however and it turned out (as the microscope objective was misaligned) that the  $750\text{mm}$  tube lens was roughly  $100\text{mm}$  out of ideal alignment. Once the tube lens was aligned to the camera independently of the objective position, the objective could be brought into focus and the resolution of the imaging system could be improved.

### 4.7.3 In-Situ Images of Density Modulated States

After increasing the intensity of the vertical absorption imaging arm and its aligning images of density modulated phases of Dy could be taken. A few of these pictures, taken at different intensities and exposure times, are shown in Figure 4.16. These pictures demonstrate that the high-intensity absorption imaging scheme is suitable for imaging highly dense atomic clouds in-situ. They also finally allow the verification of the calculated SNRs and probe conditions.

In the images of the droplet phases of Figure 4.16, we find that the actual maximum bare OD increases with intensity and is around  $\sigma_{eff}\bar{n}_z = 8$  in the highest intensity pictures. The increase with intensity could indicate that the fully saturated regime is not yet reached and that the SNR is underestimated at lower intensities. But even at the highest intensities the value  $\sigma_{eff}\bar{n}_z = 8$  is much smaller than the bare OD of 254 previously estimated from a similar experiment [Soh+21] (see Table 4.1). Partly this reduced OD can be attributed to the polarisation of the light currently used, which reduces the absorption cross-section by about half ( $\sigma_{eff} = \sigma_0/2$ ). On the other side, this can also simply be attributed to differences in the experimental conditions. Indeed, compared to [Soh+21], we observe a larger system size.

At the maximum bare OD of around 8, the SNR and appropriate probe conditions can once again be calculated (see 4.3). Both for the used absorption imaging scheme and for the designed phase contrast imaging scheme, the result are shown in Figure 4.17. The parameters that were used to take the images in Figure 4.16 are indicated by the letters  $a, b, c$  and  $d$ . By eye, there seems to be a nice agreement between the experimental pictures and the estimated SNR. Interestingly, the pictures with parameters  $a$  and  $d$  are outside of the appropriate probe conditions. It may therefore be assumed that the droplets in the picture taken at  $s=0.7$  were dispersed by the imaging light itself. Also, in the image taken at  $s=63$ , a problem of apparent negative OD appears. The colour scheme in Figure 4.16 is cut at OD=0, but the regions of apparent negative OD can be



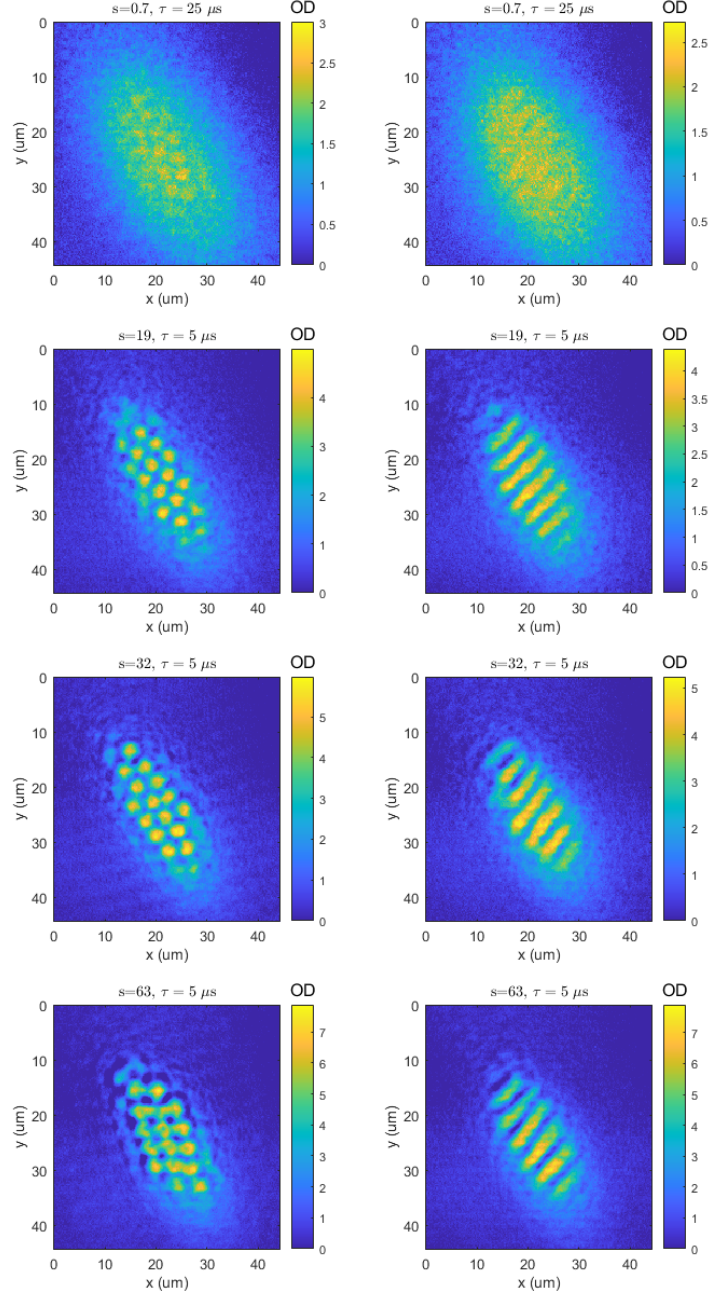


Figure 4.16: In-Situ absorption imaging pictures of droplet and stripe phases. The droplets (stripes) were prepared at an external magnetic field of 2.30G (2.45G). The images were taken at different intensities and exposure times indicated above the figures.

seen where ‘voids’ appear in the cloud of droplets. Comparing to Figure 4.17, this issue may arise due to the saturation of the pixel in the bright background picture.

The calculated SNRs for the dispersive imaging scheme indicates a usable parameter regime for high SNR images. Quite large saturation parameters may be needed on the order a few hundreds. Due to the low saturation intensity of the 626nm transition, this may actually be achieved even at a large beam waist of 12mm. A phase contrast imaging scheme may thus still present a useful addition to the experiment providing non-destructive measurements.

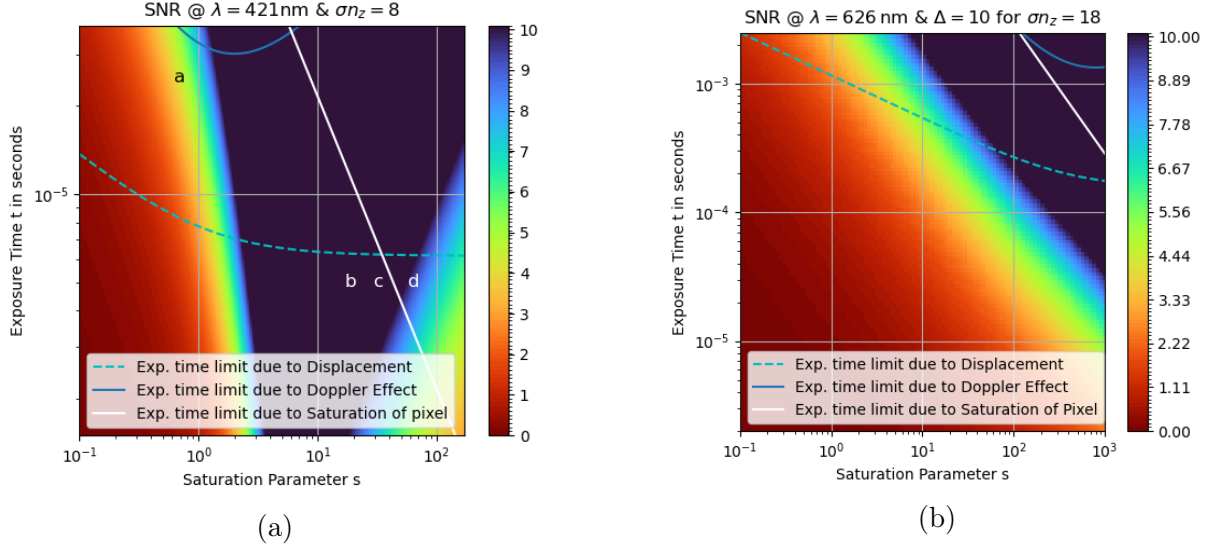


Figure 4.17: Calculated SNRs and appropriate probe conditions for the measured in-situ density of droplets. For the (a) absorptive imaging scheme at 421nm and (b) for the dispersive imaging scheme at 626nm. The letters in (a) indicate the parameters used in Figure 4.16. Notice, that the bare OD for the phase contrast imaging differs from the absorption imaging scheme, due to a change of the absorption cross section  $\sigma$ .



# Chapter 5

## Simulating $^{161}\text{Dy}$ Trapping for FerDy Experiment

### 5.1 Experimental Results from BoDy

During the planning phase of the new FerDy experiment in which fermionic Dysprosium is to be studied, the trapping of  $^{161}\text{Dy}$  was attempted in the 2DMOT of the currently operating "BoDy" experiment in Heidelberg. The 2DMOT is well described in [Jin+23; Gao22]. While it was clear that the fermionic isotopes will behave differently to the bosonic ones due to the hyperfine splitting of the former, it is a priori not clear how this difference would affect the trapping efficiency.

In principle, two choices for fermionic Dysprosium isotopes are available due to the abundance of isotopes. The isotope  $^{163}\text{Dy}$  has an inverted hyperfine structure due to a positive  $A_{HFS}$  coefficient, which results in the ground state hyperfine level  $F = 21/2$  having the highest energy. The only closed hyperfine transition between  $J = 8$  to  $J' = 9$  is the transition between the  $F = 21/2$  to the  $F = 23/2$  sublevels, it is required to drive a transition between these highest hyperfine sublevels. Cooling to degeneracy from these highest hyperfine states leads to losses due to spin changing collisions.

Therefore, we focus on trapping  $^{161}\text{Dy}$ . To probe the influence of the hyperfine structure, trapping of the different largely available isotopes from  $^{160}\text{Dy}$  to  $^{164}\text{Dy}$  was attempted in the current experimental setup of BoDy.

Different transition of the different isotopes are detuned by only a few GHz from the 421nm transition of  $^{164}\text{Dy}$ . A spectrum of different transitions can be seen in Figure 5.1. Thus, by simply scanning the detuning of the single laser in bow-tie configuration, that forms the 2DMOT, the trapping of different isotopes can be selected. To quantify the trapping of the different isotopes, fluorescence images were taken at many different detunings. By the brightness of these pictures and the data from [LCB09], the different transitions and isotopes could be identified.

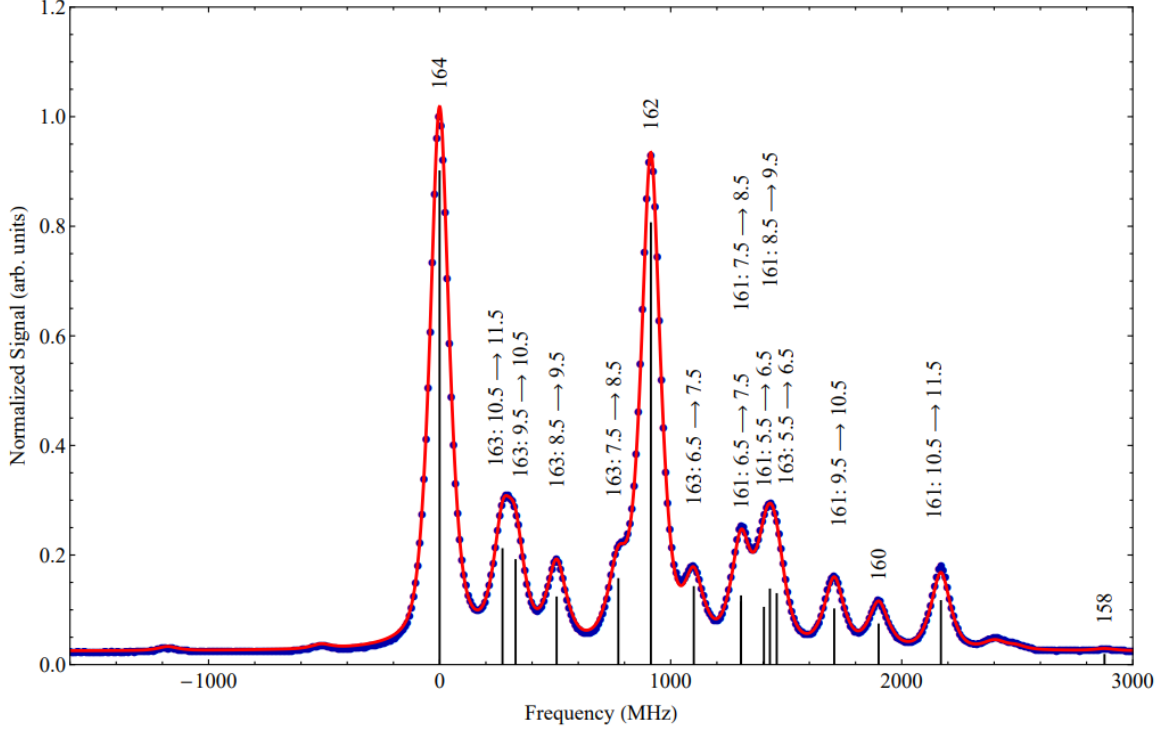


Figure 5.1: Spectrum of different transitions of different Dysprosium isotopes. All transitions are from  $J = 8$  to  $J' = 9$ , for the bosonic isotopes, this gives only one peak each, for the fermionic the spectrum is divided into the different hyperfine transition, labelled by  $(F \rightarrow F')$ . Figure taken from [LCB09].

With the 2DMOT of BoDy that features a magnetic field gradient of 34G/cm, four 421nm laser beams in a bow-tie configuration at an intensity of  $1.76I_{sat}$  and a detuning of  $-1.8\Gamma$ , no trapping of  $^{161}\text{Dy}$  was observed. It was tried to improve the trapping, by adding a (up to 20mW) repumper was added. The repumper is an additional laser beam, that serves the purpose of pumping atoms that are in the ‘wrong’ hyperfine state back into the desired one (see Figure 5.2). The blue laser that drives the closed transition from  $F = 21/2$  to  $F' = 23/2$ , that forms the 2DMOT, has a small chance to drive the  $F = 21/2$  to  $F' = 21/2$  transition. Even though this transition is around  $10\Gamma$  detuned from resonance, including the detunings from the Zeeman and Doppler shifts, the transition probability is non-negligible. Once in the  $F' = 21/2$  state, the atoms may decay back into the  $F = 21/2$  or the  $F = 19/2$  hyperfine state as  $F = F' \pm 0, 1$ . The purpose of the repumper then is to pump atoms that decayed into the  $F = 19/2$  state back to the  $F' = 21/2$  state, where they again have some probability to enter back into the ‘closed’ transition starting from  $F = 21/2$ .

The results of the attempted trapping including a repumper are shown in Table 5.1. For better clarity the intensities of the images have been integrated along the horizontal. The background brightnesses come from the strongly and broadly distributed Doppler shifted atomic jet being more or less resonant with the fluorescence light. The intensity of

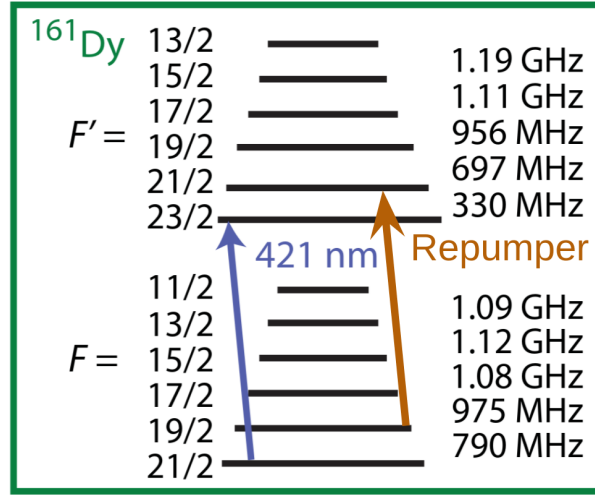


Figure 5.2: Hyperfine structure of  $^{161}\text{Dy}$  and the two beams used for an attempted 2DMOT. The blue arrow indicates the 2DMOT beam driving the 421nm transition, whereas the orange arrow indicates the repumper that was used in an attempt to improve the trapping of  $^{161}\text{Dy}$ . Figure taken from [LCB09] and adapted.

the 2DMOT is both dependent on the trapping efficiency and on the natural abundance of a given isotope. The 2DMOT of  $^{160}\text{Dy}$  with a natural abundance of only 2.3% [Kon+21] shows up only faintly against the background in fluorescence imaging. But evidently, there is still no trace of a  $^{161}\text{Dy}$  2DMOT even though its natural abundance is comparable to that of  $^{164}\text{Dy}$ . At this point it is not yet clear if the atoms are actually not being trapped or if the fluorescence signal is merely too faint. It is clear however, that this issue requires a more thorough understanding.

Thus, two approaches were chosen to investigate the dynamics of trapping  $^{161}\text{Dy}$ . An analytical model was built to investigate the relevant detunings between the different hyperfine transitions under different magnetic fields. At the same time the trapping of different Dysprosium isotopes was simulated with the PyLCP python package [Eck+20]. In the following, first the analytical model is introduced, then the working principles of the PyLCP simulation are described and the combined results and conclusions are presented.

## 5.2 Analytical Model

The aim of the analytical model was to calculate the detuning of all possible hyperfine transitions for a set laser frequency and from this, calculate a scattering rate for each of the transitions. This can be used to estimate the force contribution of each of these transitions and to help understand the dynamics of optically pumping the atoms into specific states.

As a fast atom travels into a 2DMOT, it experiences a whole range of Zeeman shifts

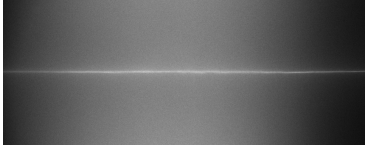

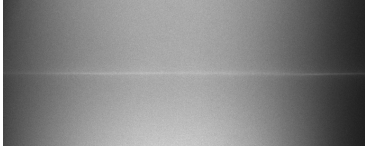

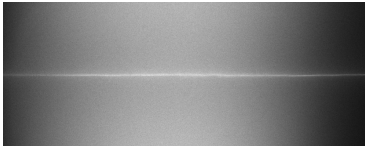



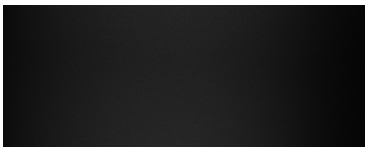

Isotope	Detuning[GHz]	Fluorescence Image	Integrated Intensity [a.u.]
$^{164}\text{Dy}$	0		
$^{163}\text{Dy}$	0.29		
$^{162}\text{Dy}$	0.93		
$^{160}\text{Dy}$	1.93		
$^{161}\text{Dy}$	2.18		

Table 5.1: Fluorescence pictures of a 2DMOT for the different isotopes. To help see even the faint 2DMOTs, the intensity of the fluorescence pictures was integrated along the horizontal and is depicted in the rightmost column. The laser detuning was optimized to maximise the brightness of the fluorescence images. In the range of frequencies that are expected to trap  $^{161}\text{Dy}$  no indication of a 2DMOT was found. The detuning is given relative to the optimized  $^{164}\text{Dy}$  2DMOT. Data taken (with repumper) by the DyLab team.

due to the gradient field in the MOT and (if it is affected by the MOT beams) a similarly large range of Doppler shifts due to the change of velocity. It is therefore quite possible that some transition becomes resonant with one of the four MOT beams at an unwanted position in the phase space spanned by velocity and local magnetic field. To estimate this behaviour, the analytical model takes the following mechanisms into account:

## Doppler Shift

The detunings and scattering rates are calculated at some fixed velocity  $v$ . This velocity causes a Doppler shift given by Equation (2.65).

## Light Detuning

All detunings are specified to a reference frequency (usually the frequency of the closed  $F = 21/2 \rightarrow F' = 23/2$  transition). The laser frequency is statically red detuned to the reference frequency. Each transition is given the linewidth of 32.3MHz, which dictates the scattering rate for detuned light. Furthermore, a certain polarisation of the laser light is specified, which limits the amount of available transitions between hyperfine levels.

## Hyperfine Structure

Essentially, the hyperfine structure of the isotopes is specified. Each hyperfine level is split into Zeeman sublevels in the presence of a magnetic field following Equation (2.68).

The average force contribution of the transition between two states was estimated, following Equation (2.53) & Section 2.2.6, to be:

$$\mathbf{F}_{m_F m'_F}^{FF'} = \langle F m_F | \mathbf{d} | F' m'_F \rangle \frac{\hbar \mathbf{k}}{2} \Gamma \frac{s}{1 + 4(\Delta/\Gamma)^2} \quad (5.1)$$

The detuning  $\Delta = \Delta_L + \Delta_{Dop} + \Delta_{Zem} + \Delta_{HFS}$  is the total detuning of the laser light from a reference value. As reference, the  $F = 21/2 \rightarrow F' = 23/2$  hyperfine transition was chosen. The hyperfine splitting from the fine structure level at zero field is given by  $\Delta_{HFS}$ . The Zeeman effect shift the energy levels of the Hyperfine states, lifting the degeneracy of the hyperfine manifolds. This energy shift is described by the described as the detuning  $\Delta_{Zem}$ .

This rate equation model does not model the actual force on an atom accurately. It rather described the scattering probability between different hyperfine levels. The force is approximated by multiplying this rate with photon momentum  $\hbar k/2$ . This model does not take the actual populations of specific hyperfine levels into account and there is no mechanism implemented, that simulates the optical pumping to different levels. This dynamic is implemented in PyLCP to some degree (see Section 5.3.1).

## Hyperfine Detunings at Zero Field

Nonetheless, it offers some understanding of the relative detunings of different transitions and how likely these transitions are. As a first example, the accelerations in the rate equation model for the fermionic isotopes in a counter-propagating beam at zero magnetic field are shown in Figure 5.3 for a range of different velocities. Here, the push beam points in the ‘negative’ direction, resulting in negative accelerations. The beam is resonant with the  $F = 21/2 \rightarrow F' = 23/2$  transition at zero velocity. The analytical model and the PyLCP simulation yield near-identical results, as both implement a similar rate equation model (see Section 5.3.1).



Where a bosonic isotope would only show one central peak at zero velocity with a width given by  $\Gamma$ , due to the more complex hyperfine structure the fermionic isotopes show multiple, distinct peaks. The analytical model calculates the detuning of every possible  $|F m_F\rangle \rightarrow |F' m_{F'}\rangle$  transition, which are plotted individually and summed to give the total accelerations at each velocity. By plotting  $F \rightarrow F' = F \pm 0, 1$  in different colours, the overall accelerations can be assigned to different transitions. In this case, the  $F \rightarrow F' = F + 1$  transitions contribute the largest scattering rates, a small contribution is given by the  $F \rightarrow F' = F$  transitions whereas no contribution of the  $F \rightarrow F' = F - 1$  transitions can be seen on this scale. The ‘closed’ cooling transition  $F = 21/2 \rightarrow F' = 23/2$  is therefore about 40 times more probable than the  $F = 21/2 \rightarrow F' = 21/2$  transition, even when both transitions are resonant with the light.

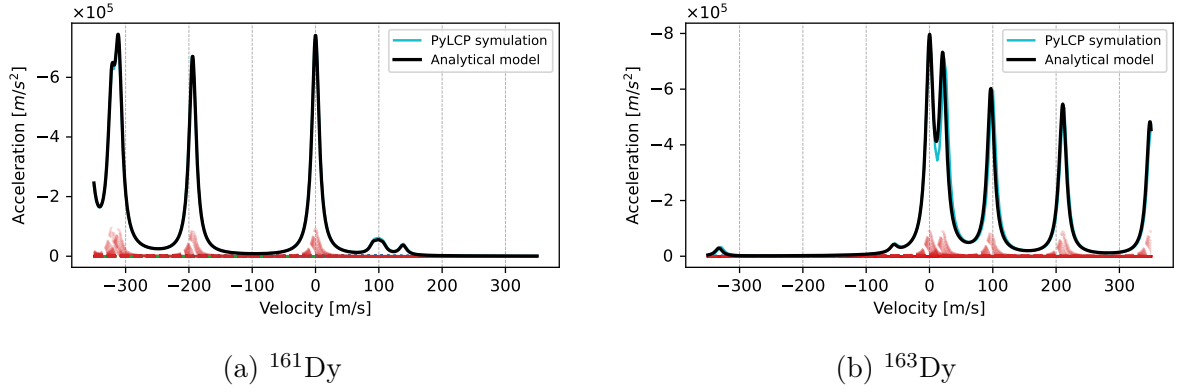


Figure 5.3: Accelerations due to a counter-propagating push beam for (a)  $^{161}\text{Dy}$  and (b)  $^{163}\text{Dy}$  atoms at different velocities, without a magnetic field. The push beam has an intensity of  $I = I_{\text{sat}}$  and is resonant with the  $F = 21/2 \rightarrow F' = 23/2$  transition at zero velocity. The accelerations are calculated both via the analytical model (black) and the PyLCP simulation (cyan). Due to the good agreement between both models, the cyan and black curve appear mostly identical in the plot. In the analytical model, every possible  $|F m_F\rangle \rightarrow |F' m_{F'}\rangle$  transition is plotted and later summed yielding the total acceleration (black).  $F \rightarrow F' = F - 1$  transitions are plotted in dash-dotted green,  $F \rightarrow F' = F$  transitions are plotted in dotted blue, and  $F \rightarrow F' = F + 1$  transitions are plotted in dashed red.

The centered peak for both fermions belongs to the  $F = 21/2 \rightarrow F' = 23/2$  transition, to which the laser is resonant at zero velocity. For  $^{161}\text{Dy}$ , in the regime of negative velocities (velocities that are parallel to the push beam direction) different transitions with large scattering rates can be seen. The peak around -200m/s belongs to the  $F = 19/2 \rightarrow F' = 21/2$  transition, the peak above -300m/s is a combination of the  $F = 17/2 \rightarrow F' = 19/2$  and  $F = 11/2 \rightarrow F' = 13/2$  transitions. At positive velocities of around  $100\text{m/s}^{-1}$  to  $150\text{m/s}^{-1}$  there seem to be two smaller peaks. These are actually the contributions of *all* five transitions where  $F = F'$ . The individual scattering rates of these transitions are so small however, that they are next to invisible in a linear scaled plot.

Similarly, for the  $^{163}\text{Dy}$  isotope, the larger peaks, which are in this case found at negative detunings, belong to the five different possible  $F \rightarrow F' = F + 1$  transitions. The smaller peaks in the range of negative velocities/ more positive detunings belong to the  $F \rightarrow F' = F$  transitions. However, in this case they can be identified to belong to the  $F = 15/2 \rightarrow F' = 15/2$  and the  $F = 17/2 \rightarrow F' = 17/2$ . Importantly, the  $F = 21/2 \rightarrow F' = 21/2$  transition is so far detuned, that it only becomes resonant at a velocity of around  $-890\text{m s}^{-1}$ . As will be discussed below, this large detuning will explain the observed trapping of  $^{163}\text{Dy}$  where  $^{161}\text{Dy}$  was elusive.

The relative strength of scattering rates, which is indicated by the height of the peaks in Figure 5.3, is given by the the squares of the values of the Wigner-6j symbols (see Equation (5.1) and (2.62)). The values for Dy are given in Table 5.2. We can see that the contributions of  $F \rightarrow F' = F - 1$  transitions is heavily suppressed, that  $F \rightarrow F' = F$  transitions give only a small contribution and that the scattering rate is largest for the  $F \rightarrow F' = F + 1$  transitions.

$F \setminus F'$	13/2	15/2	17/2	19/2	21/2	23/2
11/2	1.0000	0	0	0	0	0
13/2	0.0370	0.9630	0	0	0	0
15/2	0.0005	0.0514	0.9481	0	0	0
17/2	0	0.0007	0.0513	0.9480	0	0
19/2	0	0	0.0006	0.0413	0.9582	0
21/2	0	0	0	0.0003	0.0237	0.9761

Table 5.2: Squares of Wigner 6j symbols for the transitions  $F \rightarrow F'$ .

## Hyperfine Detunings in a Magnetic Field

To study the effect of a magnetic field on the above transitions, the same scenario as above but at a constant magnetic field of  $|\mathbf{B}| = 100\text{G}$  is plotted in Figure 5.4. A field of  $100\text{G}$  was chosen because it roughly corresponds to the field magnitude where the atoms enter the 2DMOT in BoDy. To keep the  $F = 21/2 \rightarrow F' = 23/2$  resonant, a detuning of around  $-4.11\text{G}/100\text{G}$  was applied. A detuning of around  $-7.37\text{G}/100\text{m s}^{-1}$  has to be applied to compensate for the Doppler effect. While there are quantitative differences between the PyLCP simulation and the analytical model, they agree qualitatively. The likely origin of these differences is the definition of the eigenstates in the two different approaches. While in PyLCP the eigenstates are determined locally (see Section 5.3.1), by diagonalizing the atomic Hamiltonian including the Zeeman shift, the eigenstates in the analytical model are always taken to be the  $|F m_F\rangle$  states. As discussed in Section 2.2.4, this basis will cease to be a good approximation as the Zeeman effect can no longer be treated as a perturbation to the hyperfine Hamiltonian. Working at moderate field strengths, this only causes quantitative differences.

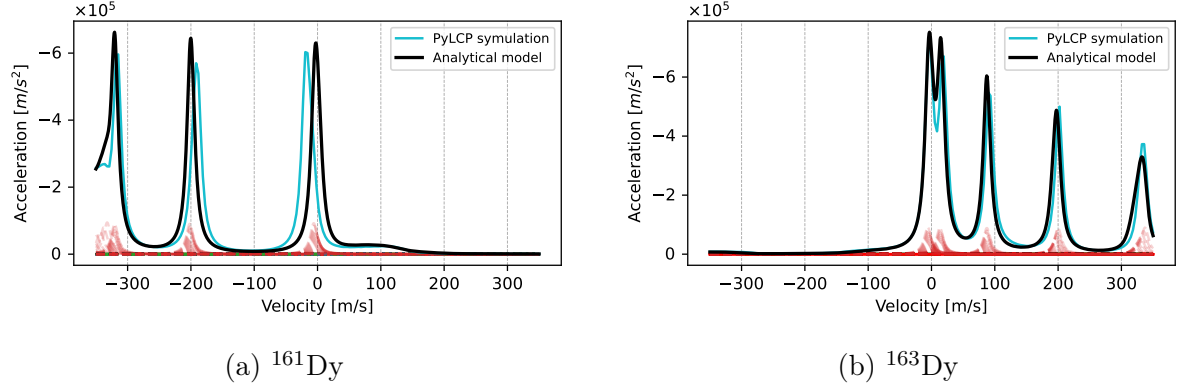


Figure 5.4: Accelerations due to a counter-propagating push beam for (a)  $^{161}\text{Dy}$  and (b)  $^{163}\text{Dy}$  atoms in dependence of velocity at a magnetic field of 100G. The push beam has an intensity of  $I = I_{\text{sat}}$  and is right-handed polarised along  $\mathbf{k}$ . A detuning of  $\Delta = -4.11\Gamma$  keeps the beam resonant with the  $F = 21/2 \rightarrow F' = 23/2$  transition at zero velocity. The accelerations are calculated both via the analytical model (black) and the PyLCP simulation (cyan). For the analytical model, every possible  $|F m_F\rangle \rightarrow |F' m'_{F'}\rangle$  transition is plotted and later summed. The colour scheme is identical to Figure 5.3.

In the presence of a magnetic field the polarisation of the laser becomes important. Here the laser has a right-handed polarisation along the wavevector  $\mathbf{k}$  which will drive  $\sigma^-$  transitions, where  $m_F \rightarrow m'_{F'} = m_F - 1$ . Most importantly Figure 5.4 shows how the Zeeman effect broadens the  $F \rightarrow F' = F$  transitions. In the case of  $^{161}\text{Dy}$ , the  $F = 21/2 \rightarrow F' = 21/2$  transitions, which is detuned by around  $-10\Gamma$  at zero field, becomes nearly resonant with the light at zero velocity.

## The Influence of the $F = 21/2 \rightarrow F' = 21/2$ Transition

To understand the relevance of the  $F \rightarrow F' = F$  transitions we need to consult Table 5.2 again. Evidently, the  $F = 21/2 \rightarrow F' = 21/2$  transition remains relatively unprobable, even if it becomes resonant with the laser. However, if it does happen the atom that is now in the  $F' = 21/2$  state will decay into the  $F = 19/2$  state with a 96% probability. That means that *if* a  $F = 21/2 \rightarrow F' = 21/2$  transition happens, it will cause a pumping to smaller  $F$  with near certainty. At the same time there is nearly no natural pumping from other  $F \neq 21/2$  into the cooling transition. Even though the  $F = 21/2 \rightarrow F' = 21/2$  transition remains unlikely, as the probability of ‘losing’ the atom into another state is large and the number of scattering events is very high, this transition causes a quick de-pumping of the ‘closed’ cooling transition as soon as it is resonant with the light. This causes the atoms to no longer be resonant with the MOT light and it will be lost. In comparison, this does not happen in the case of  $^{163}\text{Dy}$ , as the  $F = 21/2 \rightarrow F' = 21/2$  transition is too far detuned from resonance to have any significant effect.

The Figure 5.4, may be interpreted as depicting the situation at the ‘entrance’ of a Zeeman Slower, where the velocity is given relative to the capture velocity of the Zeeman slower. The positive velocity in the graph correspond to atoms with velocities larger than the capture velocity, which will not be captured. The negative velocities indicate atoms that have a velocity smaller than the capture velocity, which are supposed to become resonant with the light at a later point in the Zeeman slower. In this picture, for  $^{161}\text{Dy}$ , the  $F = 21/2 \rightarrow F' = 21/2$  causes rapid de-pumping of the slowing transition if the fields are large enough. At some point if the magnetic field is small enough, the scattering rate of this transition might become small enough, such that its de-pumping effect is negligible or that it can be compensated. The other  $F \rightarrow F' = F + 1$  transitions do not matter much in this scenario, as they will not result in any significant pumping to the  $F = 21/2$  state. If atoms in the  $F \neq 21/2$  states will be slowed by the Zeeman slower and to what degree will depend on its design.

Similarly this picture can be extended to the ‘beginning of’ a 2DMOT. At the position where the atoms first come into contact with the beams of the 2DMOT, the situation is similar as to the entrance of a Zeeman slower as described above, only that an additional beam is added, co-propagating with the atoms. In this case, atoms that are too slow to be resonant with the counter-propagating beam at the beginning, will actually be accelerated *into* the 2DMOT by the co-propagating beam. This beam will become resonant with the  $F \rightarrow F' = F + 1$  before it becomes resonant with the cooling transition, causing fast optical pumping out of the cooling transition before the atom even reaches the center of the 2DMOT, from whereon it is supposed to be slowed by the counter-propagating beam.

The analytical estimates alone, therefore suggest that low maximal magnetic fields might be necessary, to successfully capture  $^{161}\text{Dy}$ . To get a better quantitative estimate

on the usable magnetic field range, a simulation of the atomic trajectories can be helpful. An approach to such a simulation will be discussed in the following section.

## 5.3 PyLCP Simulation

To better understand the trapping behaviour of the different isotopes in experiment, the trapping of Dy was simulated. Previously, during the design of the 2DMOT for BoDy, a Monte-Carlo simulation was written [Gao22]. This simulation however focussed on the behaviour of  $^{164}\text{Dy}$  which was approximated as a two-level system. While this approximation is reasonable for the bosonic isotopes, the complex hyperfine structure of the fermionic isotopes necessitates a more precise description.

Other simulations are available in literature either for two-level atoms [Che+21] or for multi-level, hyperfine structure resolved atoms [Eck+20]. It was decided to rather try and adapt the existing PyLCP simulation instead of building a new simulation able to handle multi-level atoms from scratch.

### 5.3.1 PyLCP Overview

PyLCP is a object orientated simulation written in Python [Eck+20]. The user can choose between different atomic species and between different levels of approximation of the governing equations. Arbitrary laser beams can be set up, that are specified by their beam profile, intensity, detuning and polarisation. By being able to add a custom magnetic field profile and atoms with initial velocities in initial electronic states, the simulation can calculate the trajectories of a variety of different atomic species in good agreement with experimental results [Ste20].

The PyLCP package is able to automatically generate the optical Bloch equations (OBEs) (see [Ste07; Foo05b]) and solve them for any given atomic species. However for complex atoms these will be hundreds of (time and) position dependent coupled differential equations which can be computationally expensive to solve. As we are aiming to simulate the propagation of Dy atoms we would need to solve the OBEs for a large number of time steps which will result in very long computation times. The PyLCP package however offers a step of simplification of the calculations.

By generating rate equations, that compute the scattering rate for transitions between different eigenstates of the hamiltonian, the calculations can be greatly simplified and speed up. The full Hamiltonian that is to be approximated is given by: [Eck+20]

$$\hat{H} = \hat{H}_{atom} + \hat{H}_{field} - \mathbf{d} \cdot \mathbf{E} - \boldsymbol{\mu} \cdot \mathbf{B} \quad (5.2)$$

The first term is the unperturbed atomic Hamiltonian

$$\hat{H}_{atom} = \frac{p^2}{2M} + \hat{H}_{int} \quad (5.3)$$

with atomic mass  $M$  and momentum  $p$ , where the term  $\hat{H}_{int}$  contains the internal (electronic) structure of the atom. The second term describes the external field by

$$\hat{H}_{field} = \int \frac{\epsilon_0 \mathbf{E}^2}{2} + \frac{\mathbf{B}^2}{2\mu_0} \quad (5.4)$$

where  $\mathbf{E}$  and  $\mathbf{B}$  are the electric and magnetic field operators.

For complex atoms the eigenstates of the atomic Hamiltonian are grouped into manifolds  $n, m, \dots$  associated with a carrier frequency  $\omega_{n \rightarrow m}$  and a linewidth  $\Gamma^{n \rightarrow m}$ . For Dysprosium, these manifolds correspond to the total atomic angular momentum  $F$  manifolds where the carrier frequency is given by the difference in energy between the  $|F_n m_{F_n}\rangle$  and the  $|F_m m_{F_m}\rangle$  states at zero magnetic field.

The manifolds are coupled through the third term in Equation (5.2),  $\mathbf{d}\mathbf{E}$ , while the last term  $\boldsymbol{\mu}\mathbf{B}$  only acts on the states within a manifold. The  $\boldsymbol{\mu}\mathbf{B}$  interactions introduces Zeeman shifts and lifts the degeneracy between the states in one manifold which are here denoted as  $|i, n\rangle$  with an energy  $\omega_i^n$ . Finally, to find the eigenstates of the atom  $|i, n\rangle$ , the Hamiltonian  $\hat{H}_{int} - \boldsymbol{\mu}\mathbf{B}$  is diagonalized and the states are sorted and labelled by energy.

The scattering rate between two states  $|i, n\rangle$  and  $|j, m\rangle$  due to the laser  $L$  with detuning  $\Delta_L$  from  $\omega_{n \rightarrow m}$  is then given by:

$$R_{ij,L}^{n \rightarrow m} = \frac{(\Omega_{ij,L}^{n \rightarrow m})^2}{\Gamma^{n \rightarrow m}} \frac{1}{1 + 4 [(\Delta_L - (\omega_j^m - \omega_i^n) - \mathbf{k}_L \cdot \mathbf{v}) / \Gamma^{m \rightarrow n}]^2} \quad (5.5)$$

where the excitation rate is a generalized Rabi frequency

$$\Omega_{ij,L}^{n \rightarrow m} = \frac{\Gamma^{m \rightarrow n}}{2} (\mathbf{d}_{ij}^{nm} \cdot \boldsymbol{\epsilon}_L) \sqrt{2s(\mathbf{r}, t)} \quad (5.6)$$

Here,  $\boldsymbol{\epsilon}'_L$  is the polarisation of the laser and the dipole matrix operator between the manifolds  $n, m$  is given by

$$\mathbf{d}_{ij}^{nm} = \langle i, n | \mathbf{d}^{nm} | j, m \rangle \quad (5.7)$$

The Doppler effect is captured by the term  $\mathbf{k}_L \cdot \mathbf{v}$  while the Zeeman effect is captured in the energies of the local eigenstates  $\omega_i^n$ . The quantisation axis is given by the local magnetic field. A derivation of this rate equation can be found in [Tar15].

The evolution of population  $N_i^n$  in the state  $|i, n\rangle$  is given by:

$$\dot{N}_i^n = \sum_{m>n,j,L} R_{ij,L}^{n\rightarrow m} (N_j^m - N_i^n) + \sum_{m<n,j,L} R_{ji,L}^{m\rightarrow n} (N_j^m - N_i^n) + \sum_{m>n,j} \Gamma_{ij}^{m\rightarrow n} N_j^m - \sum_{m<n} \Gamma^{n\rightarrow m} N_i^n \quad (5.8)$$

where the first two terms denote the evolution of the population due to optical pumping and stimulated emission. The last two terms describe the rate of spontaneous emission into and from the state  $n$ .  $\Gamma^{m\rightarrow n}$  is the decay rate of manifold  $m$  to  $n$  and  $\Gamma_{ij}^{m\rightarrow n}$  is the branching ratio

$$\Gamma_{ij}^{m\rightarrow n} = \Gamma^{m\rightarrow n} \frac{|\mathbf{d}_{ij}^{nm}|^2}{\sum_i |\mathbf{d}_{ij}^{nm}|^2} \quad (5.9)$$

For each time step in the simulation, the evolution of the populations of states is calculated and the force at each time step is connected to the sum of scattering rates of all lasers as:

$$\mathbf{F} = \sum_L \frac{\hbar \mathbf{k}_L}{2} \sum_{m,n,j,L} R_{ij,L}^{n\rightarrow m} (N_j^m - N_i^n) + M \mathbf{a} \quad (5.10)$$

where  $\mathbf{a}$  is a constant acceleration due to gravity that can be specified.

The user now only has to define a number of time steps that are to be simulated and the simulation will calculate the trajectory for the specified amount of time.

### 5.3.2 Adaptations to PyLCP

While PyLCP allows the use of different pre-defined atomic species, Dy is not included in this list. Therefore, a function was added, that includes the necessary data to set up the Hamiltonian  $\hat{H}_{int}$  for Dy in the coupled hyperfine basis. This data consists of the atomic mass, the nuclear spin and nuclear magnetic moment to define the nuclear properties. To define the relevant electronic states, the ground state and the  $^1P_1$  excited state of Dy was specified, including the quantum numbers, the lifetime, the Landé factor, and hyperfine coefficients of each state and the energy of the excited state compare to the ground state. The relevant data can be found in Section 2.1. The relevant code can be found here: [Hoe25b].

Apart from calculating trajectories, PyLCP can generate force fields in the phase space of velocity and position. These forcefields can give a useful visualisation of the local forces in a MOT. However, the generation of these profiles was implemented by basically pinning an atom at one position in phase space and letting the populations involve until they reach an equilibrium. Only then is the force calculated for this specific equilibrium population.

Due to different pumping effects and the possible non-adiabaticity of a trapping trajectory, this can lead to confusing results. Instead, the function was adapted, such that some initial population can be defined and will remain fixed, while the forces at each

point in phase space is being calculated. This variation of the calculated force can be found (among other useful functions) here: [Hoe25a].

Finally, as the simulation of a single trajectory of an atom with hyperfine structure can take many hours, meaningful abort conditions were added to the package. These conditions terminate the simulation when the atom enters a certain region in phase space. Specifically, the user can add a global radius in real space, that ends the simulation once an atom surpasses it. This is useful to end simulation runs of atoms that are not trapped. The user can also specify a set of velocity and position, that defines a ‘trapped’ region. Once the atom is slow enough *and* within a certain radius, the simulation is interrupted.

### 5.3.3 Limitations of the rate equation formalism and the PyLCP Package

Before showcasing some results of the simulation an important issue has to be mentioned. Due to the way PyLCP finds the eigenvalues of the Hamiltonian  $\hat{H}_{int} - \boldsymbol{\mu}\mathbf{B}$  and the way state populations are handled, certain issues arise that can lead to unphysical and meaningless results.

#### Underestimation of the Force

This limitation arises due to the simplifications made in the rate equation model. As the force on an atom is calculated according to Equation (5.10), the force an atom experiences is proportional to the population in the transition states that are being driven.

This is quite unphysical however, as only the scattering rate depends on the probability that an atom is in a certain state, but the overall force per scattering event will always be the same. That means that in the simulation, because an atom is always treated as being in a superposition of all states, the accelerations of trajectories can be underestimated. Instead of accelerating/decelerating the few atoms that are in the ‘correct’ state with the full maximal acceleration and separating their trajectories from those that are in the ‘wrong’ state, a sort of average trajectory is calculated that misrepresents both cases. If the cooling transition is a closed transition and the atoms are continuously being pumped into the cooling transition this effect may not matter much. But if there are de-pumping processes that cause only a small percentage of the atoms to remain in the cooling transition, their trajectories will not be estimated to a usable degree of accuracy.

#### Labelling of Hyperfine States

PyLCP finds the eigenstates of the local Hamiltonian  $\hat{H}_{int} - \boldsymbol{\mu}\mathbf{B}$ , by diagonalizing it numerically and returns states ordered by energy. At low fields this yields the states in the hyperfine  $|F m_F\rangle$  basis. As discussed in Section 2.2.4, the hyperfine basis will cease



to be a good approximation with increasing field strength. Therefore, the states  $|i, n\rangle$  are given in the local eigenbasis rather than in the  $|F m_F\rangle$  basis. As the dipole matrix operator  $\mathbf{d}^{nm}$  is projected onto this local eigenbasis, this method gives correct results.

However, the method of labelling eigenstates by energy gives unphysical results. Because the hyperfine manifolds of Dy are closely spaced in energy, the energies of hyperfine states in different manifolds can cross at moderate fields already. This is illustrated in Figure 5.5. At fields of only tens of Gauss, the hyperfine sub-states cross in energy values. Labelling the states only by their energy, then results in an entirely different case as properly labelling them according to their  $|F m_F\rangle$  labels. The numerical diagonalisation and sorting does not retain any information about state labels, and thus the populations of two states will exchange abruptly as they cross energy levels. This causes a kind of sudden, unphysical pumping between states and yields unphysical results.

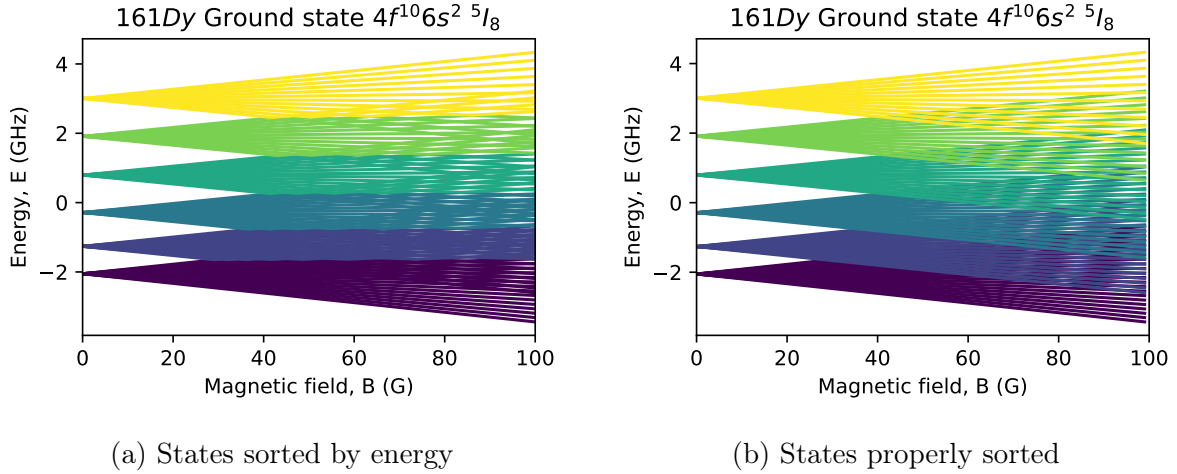


Figure 5.5: Sorting of hyperfine states. The colours in (a) indicate states merely sorted by their energies. The colours in (b) indicate the actual energies of the  $|F m_F\rangle$  states.

As will be illustrated in the following, both of these limitations only apply to atoms that exhibit a hyperfine structure and the latter due to the pumping dynamics between different hyperfine states, these issues have only a small effect on  $^{163}\text{Dy}$  but basically prohibit a meaningful simulation of  $^{161}\text{Dy}$  trajectories.

### 5.3.4 Simulation Results

To benchmark the PyLCP simulation, it was first compared to the previously established results of trapping bosonic  $^{164}\text{Dy}$  (see [Gao22]) which were compared to experiment in good agreement.

In Figure 5.6 simulations of the trapping of  $^{164}\text{Dy}$  in the 2DMOT of BoDy are shown. Both the results of the PyLCP simulation as well as the previously used Monte-Carlo simulation of a two-level atom are compared in the figure. For the atoms, initially traveling along the x-axis into the 2DMOT angled at  $45^\circ$ , a good agreement is found between

both between the qualitative behaviour of the simulations, as well as for the trapping velocity of around  $100 \frac{m}{s}$ . Both graphs show the accelerations, that the atoms experience at each point in the (phase) space in colour and a set of exemplary trajectories in white. The cut-off of the force field at a position of around 25mm is due to the aperture of the cooling beams. A good quantitative agreement of the accelerations is found between the two simulations.

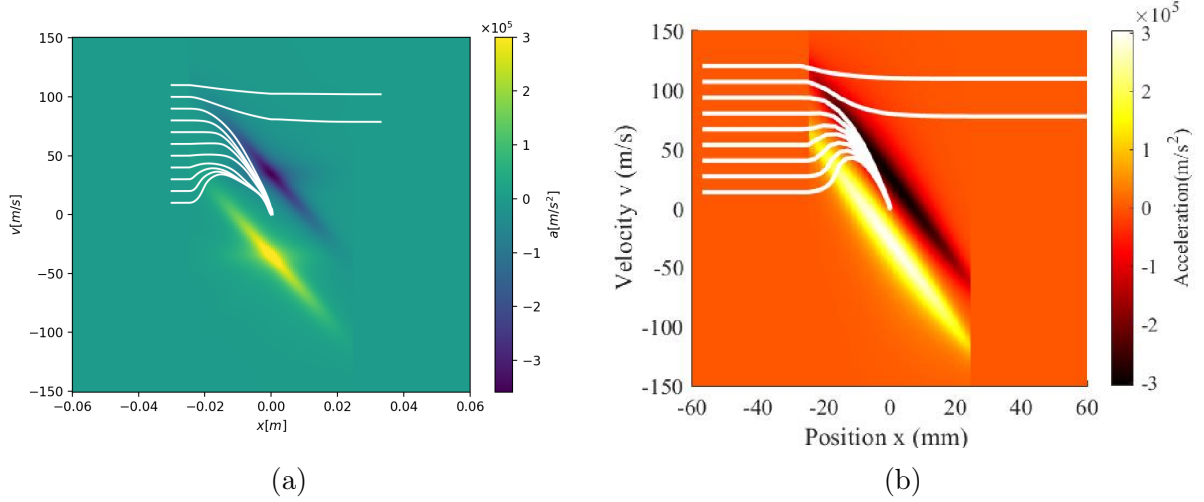


Figure 5.6: Simulated trajectories of  $^{164}\text{Dy}$  into the 2DMOT of BoDy. The results of the PyLCP simulation (a) are in good agreement with those of the Monte Carlo simulation developed previously [Gao22].

In this case it becomes evident, that the shortcomings of the rate equation model of PyLCP do not affect the trapping behaviour of  $^{164}\text{Dy}$  significantly. First of all the mislabelling of states does not occur as the bosonic isotope has no hyperfine structure and all available states can indeed be sorted by energy. And secondly the forces acting on the atoms are not significantly underestimated, as the circular polarised light quickly pumps the Zeeman sublevels into a closed transition. There, the population of one state becomes large and the force is adequately estimated.

The simulations of fermionic Dy are more affected by the limitations of PyLCPs rate equation model that were explained above. Due to the complex hyperfine structure and the energetic mixing of different Zeeman sublevels at even moderate fields, the results of fermionic trapping break down in many cases. For  $^{161}\text{Dy}$ , the mislabelling of Zeeman sublevels happens at around 30G for the ground state and at only around 10G for the excited state. This leads to an unphysical kind of pumping between sublevels, which will typically result in a fast depumping of the cooling transitions causing the 2DMOT light to become ‘invisible’ to the atoms in the simulation. In early simulation runs, a 2DMOT of  $^{163}\text{Dy}$  was seen while  $^{161}\text{Dy}$  could not be trapped. What was initially thought to be a qualitative agreement between the experimental results of Table 5.1, was soon discovered to be more or less coincidence. The Zeeman energetic mixing between sublevels of the

$F = 21/2$  manifold with others, happens only at larger fields (around 80G for the ground state and around 70G for the excited state) for the  $^{163}\text{Dy}$  isotope. Therefore, the issue of mislabelling the hyperfine states will affect this isotope less (for a fixed magnetic field).

By simulating the trapping of  $^{161}\text{Dy}$  in a 2DMOT that works at a lower magnetic field gradient and thus has a smaller trapping velocity, the effect of the above mentioned issues can be reduced. And indeed by simulating an angled 2DMOT, similar to that of BoDy, but at a smaller magnetic field and laser parameters as used in a 3DMOT for  $^{161}\text{Dy}$  developed by Lev et al. [You+10], a 2DMOT of  $^{161}\text{Dy}$  was found.

Figure 5.7 shows the simulated trajectories for  $^{161}\text{Dy}$  both for the BoDy 2DMOT and an angled 2DMOT inspired by Lev et al. The 2DMOT of BoDy has a magnetic field gradient of 34G/cm a detuning of  $-1.8\Gamma$  and an aperture of 17.5mm. The Lev et al. MOT in this simulation has a magnetic field gradient of 10G/cm a detuning of  $-1.2\Gamma$  and an aperture of 11mm.

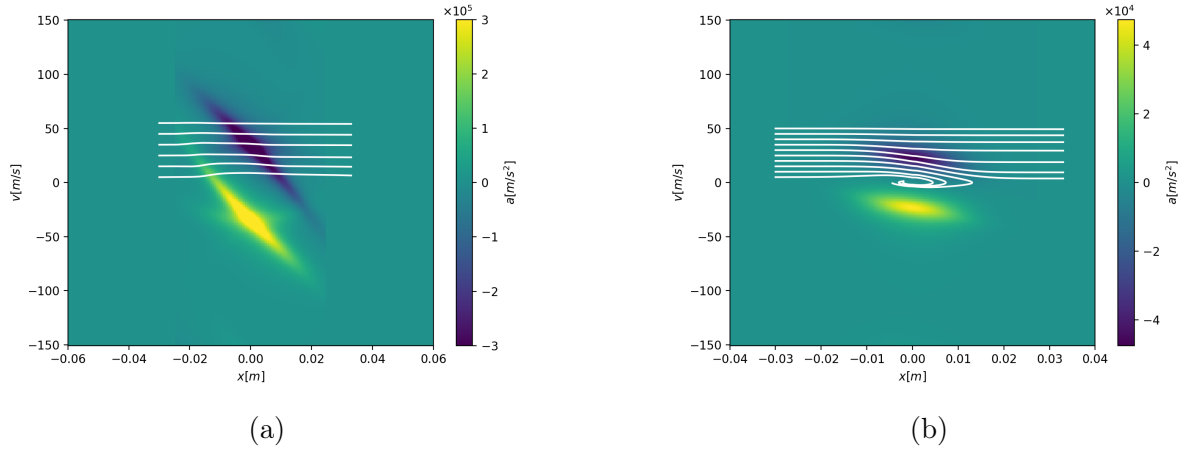


Figure 5.7: Simulations of trapping  $^{161}\text{Dy}$  in a 2DMOT. These results suffer from the limitations of the simulated model, as explained above. The parameters for the 2DMOTs follow the 2DMOT of (a) the Body experiment and (b) the 3DMOT for fermionic Dy of Lev et al.[You+10].

Due to the lower magnetic field gradient, the trapping velocity of the 2DMOT in Figure 5.7 (b) is reduced, but trapping of velocities of up to  $15 \frac{m}{s}$  can be observed. These results however, should be seen as merely qualitative examples, as the mislabelling of states was not resolved in these simulations.

## 5.4 Conclusions from Analytics and PyLCP

The comparison of the hyperfine detunings including different Doppler and Zeeman shifts shows a good agreement between the analytical model and the PyLCP simulation, validating the working principle of the simulation.

The analytical considerations indicate that a quick de-pumping of the cooling transition at large magnetic fields, due to the  $F = 11/2 \rightarrow F' = 11/2$  transition becoming resonant, prohibits the capture of  $^{161}\text{Dy}$  in the 2DMOT of the BoDy experiment. As soon as an atom is pumped out of the closed cooling transition, it will be ‘lost’ as further scattering events and decays will only pump it to lower  $F$  manifolds. Also due to the scattering rates between the hyperfine manifolds, the repumper that was used experimentally, was less effective than naïvely expected.

With the PyLCP simulation successful trapping of  $^{161}\text{Dy}$  was simulated, as long as the maximal magnetic field strength was below 11G. This limitation both reduced unwanted, unphysical errors in the simulation as well as the expected influence of the  $F = 21/2 \rightarrow F' = 21/2$ . Due to the limitations of the rate equation model as well as the mislabelling of hyperfine sub-states, the simulation could not be used to determine optimal field parameter. However, the limitations mentioned above should both reduce the trapping velocity of  $^{161}\text{Dy}$ , as the simulated forces are weaker and the pumping in other hyperfine manifolds is stronger than in reality. Therefore, the simulation can be treated as a worst case limit, and trapping of  $^{161}\text{Dy}$  can be expected at small field gradients, limiting the maximal field magnitude.

These results indicate that the permanent-magnet 2DMOT used in BoDy is not suitable for trapping  $^{161}\text{Dy}$ , and that a 2DMOT operating at much lower magnetic field gradients will be required. A smaller magnetic field gradient will limit the capture velocity of the MOT, which will necessitate the use of a Zeeman slower to increase the flux of captured atoms. Lev et al. successfully trapped  $^{161}\text{Dy}$  in a 3DMOT, after slowing a thermal atomic jet in a Zeeman slower [You+10]. The use of a glass cell prohibits positioning the science chamber in line with the thermal atomic jet however, because this would result in coating at least one optical window of the cell. Therefore a design featuring a Zeeman Slower and an angled 2DMOT loading a 3DMOT in the science chamber might be adapted [Wod+21; Li+23].

More work has to be done, regarding the simulation of trapping  $^{161}\text{Dy}$ . The issue of labelling the hyperfine sub-states will have to be fixed and the rate-equation model may either need to be improved or a less simplified model might need to be used. These improvements to the simulation of the trapping of fermionic Dy are currently being implemented by Ximeng Song and the results will be soon be found in his Bachelor’s Thesis.



# Chapter 6

## Outlook

This thesis was split into two separate projects, one dealing with the in-situ imaging of Dy in the BoDy experiment and the other with trapping fermionic Dy in the FerDy experiment.

For the BoDy experiment signal to noise ratios (SNRs) of different imaging schemes were estimated and a high absorption imaging setup was implemented that enabled the imaging of density modulated states of a cold quantum gas of Dy in-situ. With these images the SNR estimates were validated. The design of a new phase contrast imaging system was presented, it could not be implemented however, due to long delays in the manufacturing process. In the future this system may still be implemented as it would enable non-destructive measurements of a highly dense degenerate gas in situ. Both the ability to measure even larger densities accurately and to take many images of the same degenerate gas sample may be a useful addition to the experiment. Also a rather unusual method for aligning a 4f imaging system was employed successfully which enabled an increase in the resolution of the absorption imaging system.

For the FerDy experiment, the trapping of  $^{161}\text{Dy}$  was analysed both analytically and numerically. The combination of both gave some insights as to why  $^{161}\text{Dy}$  can not be trapped with the BoDy 2DMOT. The  $F = 21/2 \rightarrow F' = 21/2$  was identified to cause significant losses of the atoms out of their ‘closed’ cooling transition. While a reliable numerical simulation of the trapping of Dy could finally not be implemented, the findings indicate that a Zeeman slower will have to be implemented into the experimental design in order to trap  $^{161}\text{Dy}$ . Improvements to the model and to the PyLCP simulation will be pursued by Ximeng Song, to further aid the design of the new experimental setup.



# Bibliography

- [Abb82] Ernst Abbe. “The Relation of Aperture and Power in the Microscope (continued).” In: *Journal of the Royal Microscopical Society* 2.4 (1882), pp. 460–473. DOI: <https://doi.org/10.1111/j.1365-2818.1882.tb04805.x>. URL: <https://onlinelibrary.wiley.com/doi/abs/10.1111/j.1365-2818.1882.tb04805.x>.
- [AF05] P. Atkins and R. Friedman. “MolecularQuantumMechanics”. In: Oxford University Press, 2005. Chap. 9, pp. 287–341. ISBN: 0-19-927498-3. URL: <https://web.stanford.edu/~oas/SI/QM/Atkins05.pdf>.
- [And+96] M. R. Andrews et al. “Direct, Nondestructive Observation of a Bose Condensate”. In: *Science* 273.5271 (1996), pp. 84–87. DOI: 10.1126/science.273.5271.84. URL: <https://www.science.org/doi/abs/10.1126/science.273.5271.84>.
- [And+97] M. R. Andrews et al. “Propagation of Sound in a Bose-Einstein Condensate”. In: *Phys. Rev. Lett.* 79 (4 July 1997), pp. 553–556. DOI: 10.1103/PhysRevLett.79.553. URL: <https://link.aps.org/doi/10.1103/PhysRevLett.79.553>.
- [Ash70] A. Ashkin. “Acceleration and Trapping of Particles by Radiation Pressure”. In: *Phys. Rev. Lett.* 24 (4 Jan. 1970), pp. 156–159. DOI: 10.1103/PhysRevLett.24.156. URL: <https://link.aps.org/doi/10.1103/PhysRevLett.24.156>.
- [Bac05] Pawel Iwanowitsch Bachtinow. *Focusing mask option*. 2005. URL: <https://astronomy.ru/forum/index.php/topic,10421.0.html> (visited on 05/09/2025).
- [Bad23] B. Bader. *Absorption Imaging for Ultracold Gases of Dysprosium: Optical Set-Up, Noise Analysis and Investigation of the Fitting Routine’s Reliability*. 2023. URL: [https://www.physi.uni-heidelberg.de/Forschung/QF/datafiles/publications/Britta\\_2023\\_BA\\_final.pdf](https://www.physi.uni-heidelberg.de/Forschung/QF/datafiles/publications/Britta_2023_BA_final.pdf).
- [Ber+18] Andrea Bergschneider et al. “Spin-resolved single-atom imaging of  ${}^6\text{Li}$  in free space”. In: *Phys. Rev. A* 97 (6 June 2018), p. 063613. DOI: 10.1103/



- PhysRevA.97.063613. URL: <https://link.aps.org/doi/10.1103/PhysRevA.97.063613>.
- [BJ83a] B.H. Bransden and C.J. Joachain. “Physics of Atoms and Molecules”. In: Longman Scientific & Technical, 1983. Chap. 5, pp. 195–247. ISBN: 0-582-44401-2. URL: [https://www.if.ufrj.br/~ginette/2017-FIW476/livros%20e%20artigos/Physics\\_of\\_atoms\\_and\\_molecules\\_Bransden\\_Joachain.pdf](https://www.if.ufrj.br/~ginette/2017-FIW476/livros%20e%20artigos/Physics_of_atoms_and_molecules_Bransden_Joachain.pdf).
- [BJ83b] B.H. Bransden and C.J. Joachain. “Physics of Atoms and Molecules”. In: Longman Scientific & Technical, 1983. Chap. 7, pp. 290–354. ISBN: 0-582-44401-2. URL: [https://www.if.ufrj.br/~ginette/2017-FIW476/livros%20e%20artigos/Physics\\_of\\_atoms\\_and\\_molecules\\_Bransden\\_Joachain.pdf](https://www.if.ufrj.br/~ginette/2017-FIW476/livros%20e%20artigos/Physics_of_atoms_and_molecules_Bransden_Joachain.pdf).
- [Blo+23] Damien Bloch et al. “Trapping and Imaging Single Dysprosium Atoms in Optical Tweezer Arrays”. In: *Physical Review Letters* 131.20 (Nov. 2023). ISSN: 1079-7114. DOI: 10.1103/PhysRevLett.131.203401. URL: <http://dx.doi.org/10.1103/PhysRevLett.131.203401>.
- [Blo05] Immanuel Bloch. “Ultracold quantum gases in optical lattices”. In: *Nature Physics* (2005). DOI: <https://doi.org/10.1038/nphys138>. URL: <https://www.nature.com/articles/nphys138>.
- [Bro24] Louis Victor de Broglie. “On the Theory of Quanta”. PhD thesis. Paris University, 1924. URL: [https://fondationlouisdebroglie.org/LDB-oeuvres/De\\_Broglie\\_Kracklauer.pdf](https://fondationlouisdebroglie.org/LDB-oeuvres/De_Broglie_Kracklauer.pdf).
- [Brü06] Arndt Brünner. *Trigonometrische Zusammenhänge, Vereinfachungen, Formeln*. 2006. URL: <https://www.arndt-bruenner.de/mathe/Allgemein/trigsimpl.htm> (visited on 05/07/2025).
- [BSH97] C. C. Bradley, C. A. Sackett, and R. G. Hulet. “Bose-Einstein Condensation of Lithium: Observation of Limited Condensate Number”. In: *Phys. Rev. Lett.* 78 (6 Feb. 1997), pp. 985–989. DOI: 10.1103/PhysRevLett.78.985. URL: <https://link.aps.org/doi/10.1103/PhysRevLett.78.985>.
- [Büc+11] Robert Bücker et al. “Twin-atom beams”. In: *Nature Physics* 7.8 (May 2011), pp. 608–611. ISSN: 1745-2481. DOI: 10.1038/nphys1992. URL: <http://dx.doi.org/10.1038/nphys1992>.
- [Cab+18] C. R. Cabrera et al. “Quantum liquid droplets in a mixture of Bose-Einstein condensates”. In: *Science* 359.6373 (Jan. 2018), pp. 301–304. ISSN: 1095-9203. DOI: 10.1126/science.aao5686. URL: <http://dx.doi.org/10.1126/science.aao5686>.

- [Car09] George Carey. *The Carey Mask*. 2009. URL: <http://www.geoastro.co.uk/careymask.htm> (visited on 05/09/2025).
- [CDG98] Claude Cohen-Tannoudji, Jacques Dupont-Roc, and Gilbert Grynberg. “Optical Bloch Equations”. In: *Atom—Photon Interactions*. John Wiley & Sons, Ltd, 1998. Chap. 5, pp. 353–405. ISBN: 9783527617197. DOI: <https://doi.org/10.1002/9783527617197.ch5>. URL: <https://onlinelibrary.wiley.com/doi/abs/10.1002/9783527617197.ch5>.
- [Che+21] X. Chen et al. *AtomECS: Simulate laser cooling and magneto-optical traps*. 2021. URL: <https://arxiv.org/abs/2105.06447>.
- [Cho+12] L Chomaz et al. “Absorption imaging of a quasi-two-dimensional gas: a multiple scattering analysis”. In: *New Journal of Physics* 14.5 (May 2012), p. 055001. ISSN: 1367-2630. DOI: 10.1088/1367-2630/14/5/055001. URL: <http://dx.doi.org/10.1088/1367-2630/14/5/055001>.
- [Cho+19] L. Chomaz et al. “Long-Lived and Transient Supersolid Behaviors in Dipolar Quantum Gases”. In: *Phys. Rev. X* 9 (2 Apr. 2019), p. 021012. DOI: 10.1103/PhysRevX.9.021012. URL: <https://link.aps.org/doi/10.1103/PhysRevX.9.021012>.
- [Cho25] Lauriane Chomaz. *Quantum-stabilized states in magnetic dipolar quantum gases*. 2025. URL: <https://arxiv.org/abs/2504.06221>.
- [con25] Wikipedia contributors. *Table of Clebsch-Gordan Coefficients*. 2025. URL: [https://en.wikipedia.org/wiki/Table\\_of\\_Clebsch%E2%80%93Gordan\\_coefficients](https://en.wikipedia.org/wiki/Table_of_Clebsch%E2%80%93Gordan_coefficients) (visited on 05/09/2025).
- [Cor25] Newport Corporation. *Parallel Optical Window, UV Fused Silica, 50.8 mm,  $\lambda/20$ , Uncoated*. 2025. URL: <https://www.newport.com/p/20QW40-30> (visited on 05/30/2025).
- [DeP+00] Marshall T DePue et al. “Transient compression of a MOT and high intensity fluorescent imaging of optically thick clouds of atoms”. In: *Optics Communications* 180.1 (2000), pp. 73–79. ISSN: 0030-4018. DOI: [https://doi.org/10.1016/S0030-4018\(00\)00701-X](https://doi.org/10.1016/S0030-4018(00)00701-X). URL: <https://www.sciencedirect.com/science/article/pii/S003040180000701X>.
- [Eck+20] S. Eckel et al. “PyLCP: A python package for computing laser cooling physics”. In: (2020). URL: <https://arxiv.org/abs/2011.07979>.
- [FDG74] J. Ferch, W. Dankwort, and H. Gebauer. “Hyperfine structure investigations in DyI with the atomic beam magnetic resonance method”. In: *Physics Letters A* 49.4 (1974), pp. 287–288. ISSN: 0375-9601. DOI: [https://doi.org/10.1016/0375-9601\(74\)90814-7](https://doi.org/10.1016/0375-9601(74)90814-7). URL: <https://www.sciencedirect.com/science/article/pii/0375960174908147>.

- [FF12] Alexander L. Fetter and Christopher J. Foot. *Bose gas: Theory and Experiment*. 2012. URL: <https://arxiv.org/abs/1203.3183>.
- [Foo05a] C.J. Foot. “Atomic Physics”. In: Oxford University Press, 2005. Chap. 6, pp. 97–120. ISBN: 0 19 850695 3. URL: <https://archive.org/details/AtomicPhysicsChristopherJ1.Foot/page/n3/mode/2up>.
- [Foo05b] C.J. Foot. “Atomic Physics”. In: Oxford University Press, 2005. Chap. 7, pp. 123–150. ISBN: 0 19 850695 3. URL: <https://archive.org/details/AtomicPhysicsChristopherJ1.Foot/page/n3/mode/2up>.
- [Foo05c] C.J. Foot. “Atomic Physics”. In: Oxford University Press, 2005. Chap. 9, pp. 178–217. ISBN: 0 19 850695 3. URL: <https://archive.org/details/AtomicPhysicsChristopherJ1.Foot/page/n3/mode/2up>.
- [Fri14] Albert Frisch. “Dipolar Quantum Gases of Erbium”. PhD thesis. University of Innsbruck, 2014. URL: [https://www.erbium.at/FF/wp-content/uploads/2015/10/thesis\\_albert\\_frisch.pdf](https://www.erbium.at/FF/wp-content/uploads/2015/10/thesis_albert_frisch.pdf).
- [Gaj+13] Miroslav Gajdacz et al. “Non-destructive Faraday imaging of dynamically controlled ultracold atoms”. In: *Review of Scientific Instruments* 84.8 (Aug. 2013), p. 083105. ISSN: 0034-6748. DOI: 10.1063/1.4818913. URL: <https://doi.org/10.1063/1.4818913>.
- [Gao22] Jianshun Gao. “A First Two-Dimensional Magneto-Optical Trap for Dysprosium”. MA thesis. University of Heidelberg, 2022.
- [GWO99] Rudolf Grimm, Matthias Weidemüller, and Yurii B. Ovchinnikov. *Optical dipole traps for neutral atoms*. 1999. URL: <https://arxiv.org/abs/physics/9902072>.
- [Ham+25] Tobias Hammel et al. *A modular quantum gas platform*. 2025. URL: <https://arxiv.org/abs/2501.08211>.
- [Har04] J. Hartmann. “Objectivuntersuchungen”. In: *Zeitschrift für Instrumentenkunde* 24 (1 Jan. 1904), pp. 1–21. URL: [https://books.google.de/books?id=XK-Xh\\_kaxogC&hl=de&source=gb\\_s\\_navlinks\\_s](https://books.google.de/books?id=XK-Xh_kaxogC&hl=de&source=gb_s_navlinks_s).
- [Her+21] J. Hertkorn et al. “Pattern formation in quantum ferrofluids: From supersolids to superglasses”. In: *Phys. Rev. Res.* 3 (3 Aug. 2021), p. 033125. DOI: 10.1103/PhysRevResearch.3.033125. URL: <https://link.aps.org/doi/10.1103/PhysRevResearch.3.033125>.
- [Hoe25a] Lennart Hoenen. *Common, useful functions around the PyLCP package*. 2025. URL: [https://git.physi.uni-heidelberg.de/lhoenen/Trapping\\_Simulation/src/branch/main/custom\\_rateeq.py](https://git.physi.uni-heidelberg.de/lhoenen/Trapping_Simulation/src/branch/main/custom_rateeq.py) (visited on 05/23/2025).

- [Hoe25b] Lennart Hoenen. *DyAtom, an extension to the PyLCP package*. 2025. URL: [https://git.physi.uni-heidelberg.de/lhoenen/Trapping\\_Simulation/src/branch/main/Dy\\_atom.py](https://git.physi.uni-heidelberg.de/lhoenen/Trapping_Simulation/src/branch/main/Dy_atom.py) (visited on 05/23/2025).
- [Hor+17] Munekazu Horikoshi et al. “Appropriate Probe Condition for Absorption Imaging of Ultracold 6Li Atoms”. In: *Journal of the Physical Society of Japan* 86.10 (2017), p. 104301. DOI: 10.7566/JPSJ.86.104301. URL: <https://arxiv.org/pdf/1608.07152>.
- [Hue+17] Klaus Hueck et al. “Calibrating high intensity absorption imaging of ultracold atoms”. In: *Optics Express* 25.8 (Apr. 2017), p. 8670. ISSN: 1094-4087. DOI: 10.1364/oe.25.008670. URL: <http://dx.doi.org/10.1364/OE.25.008670>.
- [Ilz20] Philipp Ilzhöfer. “Creation of Dipolar Quantum Mixtures of Erbium and Dysprosium”. PhD thesis. University of Innsbruck, 2020. URL: [https://www.erbium.at/FF/wp-content/uploads/2021/01/Dissertation\\_Ilzhoefer\\_Philipp.pdf#cite.00FrischThesis\\_2014](https://www.erbium.at/FF/wp-content/uploads/2021/01/Dissertation_Ilzhoefer_Philipp.pdf#cite.00FrischThesis_2014).
- [Jan07] James R. Janesick. *Photon Transfer DN  $\rightarrow$   $\lambda$* . SPIE, 2007. URL: <https://picture.iczhiku.com/resource/eetop/shITqHhziPtOLvcx.pdf>.
- [Jin+23] Shuwei Jin et al. “Two-dimensional magneto-optical trap of dysprosium atoms as a compact source for efficient loading of a narrow-line three-dimensional magneto-optical trap”. In: *Physical Review A* 108.2 (Aug. 2023). ISSN: 2469-9934. DOI: 10.1103/physreva.108.023719. URL: <http://dx.doi.org/10.1103/PhysRevA.108.023719>.
- [JL61] B. R. Judd and I. Lindgren. “Theory of Zeeman Effect in the Ground Multiplets of Rare-Earth Atoms”. In: *Phys. Rev.* 122 (6 June 1961), pp. 1802–1812. DOI: 10.1103/PhysRev.122.1802. URL: <https://link.aps.org/doi/10.1103/PhysRev.122.1802>.
- [Joo13] Maxime Joos. *Phase contrast imaging of mesoscopic Bose-Einstein condensates*. 2013. URL: <https://www.kip.uni-heidelberg.de/Veroeffentlichungen/download/5289/pdf-5289.pdf>.
- [Kad+16] Holger Kadau et al. “Observing the Rosensweig instability of a quantum ferrofluid”. In: *Nature* (2016). DOI: <https://doi.org/10.1038/nature16485>. URL: <https://www.nature.com/articles/nature16485>.
- [KDS99] W. Ketterle, D. S. Durfee, and D. M. Stamper-Kurn. *Making, probing and understanding Bose-Einstein condensates*. 1999. URL: <https://arxiv.org/abs/cond-mat/9904034>.

- [KK22] Hamamatsu Photonics K.K. *Technical Note ORCA-Quest qCMOS camera C15550-20UP*. Hamamatsu Photonics K.K. 2022. URL: [https://camera.hamamatsu.com/content/dam/hamamatsu-photonics/sites/documents/99\\_SALES\\_LIBRARY/sys/SCAS0154E\\_C15550-20UP\\_tec.pdf](https://camera.hamamatsu.com/content/dam/hamamatsu-photonics/sites/documents/99_SALES_LIBRARY/sys/SCAS0154E_C15550-20UP_tec.pdf).
- [Kon+21] F.G. Kondev et al. “The NUBASE2020 evaluation of nuclear physics properties \*”. In: *Chinese Physics C* 45.3 (Mar. 2021), p. 030001. DOI: 10.1088/1674-1137/abddae. URL: <https://dx.doi.org/10.1088/1674-1137/abddae>.
- [Lae+09] John Laeter et al. “Atomic weights of the elements: Review 2000 (IUPAC Technical Report)”. In: *Pure and Applied Chemistry - PURE APPL CHEM* 81 (Jan. 2009), pp. 1535–1536. DOI: 10.1351/PAC-REP-09-06-03\_errata.
- [Lan+08] Max Langer et al. “Quantitative comparison of direct phase retrieval algorithms in in-line phase tomography”. In: *Medical Physics* 35.10 (2008), pp. 4556–4566. DOI: <https://doi.org/10.1118/1.2975224>. URL: <https://aapm.onlinelibrary.wiley.com/doi/abs/10.1118/1.2975224>.
- [LCB09] Nathan Leefer, Arman Cingöz, and Dmitry Budker. “Measurement of hyperfine structure and isotope shifts in the Dy 421 nm transition”. In: *Optics Letters* 34.17 (Aug. 2009), p. 2548. ISSN: 1539-4794. DOI: 10.1364/ol.34.002548. URL: <http://dx.doi.org/10.1364/OL.34.002548>.
- [Li+23] Jie Li et al. “An integrated high-flux cold atomic beam source for strontium”. In: *Review of Scientific Instruments* 94.9 (Sept. 2023), p. 093202. ISSN: 0034-6748. DOI: 10.1063/5.0162128. URL: <https://doi.org/10.1063/5.0162128>.
- [Mai15] T. Maier. *Interactions in a Quantum Gas of Dysprosium Atoms*. 2015. URL: <https://www.pi5.uni-stuttgart.de/documents/abgeschlossene-arbeiten/2015-Maier-Thomas-Interactions-in-a-Quantum-Gas-of-Dysprosium-Atoms-PhD.pdf>.
- [Mei+16] Juris Meija et al. “Isotopic compositions of the elements 2013 (IUPAC Technical Report)”. In: *Pure and Applied Chemistry* 88.3 (2016), pp. 293–306. DOI: doi:10.1515/pac-2015-0503. URL: <https://doi.org/10.1515/pac-2015-0503>.
- [Mep+10] R. Meppelink et al. “Thermodynamics of Bose-Einstein-condensed clouds using phase-contrast imaging”. In: *Phys. Rev. A* 81 (5 May 2010), p. 053632. DOI: 10.1103/PhysRevA.81.053632. URL: <https://link.aps.org/doi/10.1103/PhysRevA.81.053632>.
- [Mer25] Theo J. Mertzimekis. *NUCLEAR ELECTROMAGNETIC MOMENTS*. 2025. URL: <https://www-nds.iaea.org/nuclearmoments/> (visited on 05/26/2025).

- [Oec25] U. Oechsner. *Fiber Collimator series 60FC-SF*. 2025. URL: <https://www.sukhamburg.com/products/fiberoptics/fibercoupler/series/60fc-sf.html> (visited on 05/25/2025).
- [Phi23] S Philips. *Characterizing a High-Resolution Imaging System for the Dysprosium Experiment*. 2023. URL: [https://www.physi.uni-heidelberg.de/Forschung/QF/datafiles/publications/Britta\\_2023\\_BA\\_final.pdf](https://www.physi.uni-heidelberg.de/Forschung/QF/datafiles/publications/Britta_2023_BA_final.pdf).
- [RBB23] B. T. E. Ripley, D. Baillie, and P. B. Blakie. “Two-dimensional supersolidity in a planar dipolar Bose gas”. In: *Phys. Rev. A* 108 (5 Nov. 2023), p. 053321. DOI: 10.1103/PhysRevA.108.053321. URL: <https://link.aps.org/doi/10.1103/PhysRevA.108.053321>.
- [Rei+07] G. Reinaudi et al. “Strong saturation absorption imaging of dense clouds of ultracold atoms”. In: *Optics Letters* 32.21 (Oct. 2007), p. 3143. ISSN: 1539-4794. DOI: 10.1364/ol.32.003143. URL: <https://arxiv.org/pdf/0707.2930>.
- [Sad06] Lorraine Elizabeth Sadler. “Dynamics of a Spin 1 Ferromagnetic Condensate”. PhD thesis. University of California, Berkeley, 2006. URL: <https://citeseerx.ist.psu.edu/document?repid=rep1&type=pdf&doi=6af2f3ec95a723fdd16188cc99a3c86f67ebb370>.
- [Ser+11] F. Serwane et al. “Deterministic Preparation of a Tunable Few-Fermion System”. In: *Science* 332.6027 (2011), pp. 336–338. DOI: 10.1126/science.1201351. URL: <https://www.science.org/doi/abs/10.1126/science.1201351>.
- [SF16] Dakota A. Starkey and Eric R. Fossum. “Determining Conversion Gain and Read Noise Using a Photon-Counting Histogram Method for Deep Sub-Electron Read Noise Image Sensors”. In: *IEEE Journal of the Electron Devices Society* 4.3 (2016), pp. 129–135. DOI: 10.1109/JEDS.2016.2536719.
- [SG64] A. Savitzky and M.J.E. Golay. “Smoothing and Differentiation of Data by Simplified Least Squares Procedures”. In: *Analytical Chemistry* (1964). DOI: 10.1021/ac60214a047. URL: <https://pubs.acs.org/doi/abs/10.1021/ac60214a047>.
- [Sil23] Valentina Salazar Silva. “The Accordion Lattice: Towards Trapping of Dysprosium Ultracold Gases in Two Dimensions”. MA thesis. Universität Heidelberg, 2023. URL: [https://www.physi.uni-heidelberg.de/Forschung/QF/datafiles/publications/2023\\_Valentina\\_MA.pdf](https://www.physi.uni-heidelberg.de/Forschung/QF/datafiles/publications/2023_Valentina_MA.pdf).

- [Smi13] Daniel Gene Smith. “Imaging”. In: *Field Guide to Physical Optics*. SPIE, 2013. Chap. 5, pp. 67–81. ISBN: 978-0-8194-8548-9. DOI: <https://doi.org/10.1117/3.883971>. URL: <https://www.spiedigitallibrary.org/ebooks/FG/Field-Guide-to-Physical-Optics/eISBN-9780819485496/10.1117/3.883971>.
- [SMS20] J. Smits, A. P. Mosk, and P. van der Straten. “Imaging trapped quantum gases by off-axis holography”. In: *Opt. Lett.* 45.4 (Feb. 2020), pp. 981–984. DOI: 10.1364/OL.384120. URL: <https://opg.optica.org/ol/abstract.cfm?URI=ol-45-4-981>.
- [Soh+21] Maximilian Sohmen et al. “Birth, Life, and Death of a Dipolar Supersolid”. In: *Phys. Rev. Lett.* 126 (23 Jan. 2021), p. 233401. DOI: 10.1103/PhysRevLett.126.233401. URL: <https://link.aps.org/doi/10.1103/PhysRevLett.126.233401>.
- [Soh21] Maximilian Sohmen. “Supersolidity in Dipolar Quantum Gases in and out of Equilibrium”. PhD thesis. Leopold-Franzens-Universität Innsbruck, 2021. URL: [https://www.erbium.at/FF/wp-content/uploads/2024/01/phdthesis\\_max\\_2021.pdf](https://www.erbium.at/FF/wp-content/uploads/2024/01/phdthesis_max_2021.pdf).
- [ST91a] B.E.A. Saleh and M.C. Teich. “Beam Optics”. In: *Fundamentals of Photonics*. John Wiley & Sons, Ltd, 1991. Chap. 3, pp. 80–107. ISBN: 9780471213741. DOI: <https://doi.org/10.1002/0471213748.ch2>. URL: <https://onlinelibrary.wiley.com/doi/abs/10.1002/0471213748.ch2>.
- [ST91b] B.E.A. Saleh and M.C. Teich. “Fourier Optics”. In: *Fundamentals of Photonics*. John Wiley & Sons, Ltd, 1991. Chap. 4, pp. 108–156. ISBN: 9780471213741. DOI: <https://doi.org/10.1002/0471213748.ch4>. URL: <https://onlinelibrary.wiley.com/doi/abs/10.1002/0471213748.ch4>.
- [ST91c] B.E.A. Saleh and M.C. Teich. “Wave Optics”. In: *Fundamentals of Photonics*. John Wiley & Sons, Ltd, 1991. Chap. 1, pp. 41–79. ISBN: 9780471213741. DOI: <https://doi.org/10.1002/0471213748.ch2>. URL: <https://onlinelibrary.wiley.com/doi/abs/10.1002/0471213748.ch2>.
- [ST91d] B.E.A. Saleh and M.C. Teich. “Wave Optics”. In: *Fundamentals of Photonics*. John Wiley & Sons, Ltd, 1991. Chap. 2, pp. 41–79. ISBN: 9780471213741. DOI: <https://doi.org/10.1002/0471213748.ch2>. URL: <https://onlinelibrary.wiley.com/doi/abs/10.1002/0471213748.ch2>.
- [Ste07] Daniel Adam Steck. *Quantum and Atom Optics*. revision 0.16.4, 7 May 2025. 2007. URL: <https://atomoptics.uoregon.edu/~dsteck/teaching/quantum-optics/quantum-optics-notes.pdf> (visited on 05/09/2025).

- [Ste20] Eric Norrgard Stephen Eckel Daniel Barker. *PyLCP - A python package for simulating laser cooling physics*. 2020. URL: <https://python-laser-cooling-physics.readthedocs.io/en/stable/index.html#> (visited on 05/22/2025).
- [Su+25] Lin Su et al. “Fast single atom imaging in optical lattice arrays”. In: *Nat Commun* (16 2025), p. 1017. DOI: 10.1038/s41467-025-56305-y.
- [Tar15] M R Tarbutt. “Magneto-optical trapping forces for atoms and molecules with complex level structures”. In: *New Journal of Physics* 17.1 (Jan. 2015), p. 015007. DOI: 10.1088/1367-2630/17/1/015007. URL: <https://dx.doi.org/10.1088/1367-2630/17/1/015007>.
- [Tea25] SymPy Development Team. *Python Package for Calculation of Clebsch-Gordan Coefficients*. 2025. URL: <https://docs.sympy.org/latest/modules/physics/quantum/cg.html> (visited on 05/09/2025).
- [Wen15] M. Wenzel. *A dysprosium quantum gas in highly controllable optical traps*. 2015. URL: <https://www.pi5.uni-stuttgart.de/documents/abgeschlossene-arbeiten/2015-Wenzel-Matthias-A-dysprosium-quantum-gas-in-highly-controllable-optical-traps-MSC.pdf>.
- [Wig+16] P. B. Wigley et al. “Non-destructive shadowgraph imaging of ultra-cold atoms”. In: *Opt. Lett.* 41.20 (Oct. 2016), pp. 4795–4798. DOI: 10.1364/OL.41.004795. URL: [https://opg.optica.org/directpdfaccess/6e93fed7-99c3-48bc-9d6eebc6a3941d34\\_351045/ol-41-20-4795.pdf?da=1&id=351045&seq=0&mobile=no](https://opg.optica.org/directpdfaccess/6e93fed7-99c3-48bc-9d6eebc6a3941d34_351045/ol-41-20-4795.pdf?da=1&id=351045&seq=0&mobile=no).
- [Wil+08] R. A. Williams et al. “Dynamic optical lattices: two-dimensional rotating and accordion lattices for ultracold atoms”. In: *Opt. Express* 16.21 (Oct. 2008), pp. 16977–16983. DOI: 10.1364/OE.16.016977. URL: <https://opg.optica.org/oe/abstract.cfm?URI=oe-16-21-16977>.
- [Wod+21] E Wodey et al. “A robust, high-flux source of laser-cooled ytterbium atoms”. In: *Journal of Physics B: Atomic, Molecular and Optical Physics* 54.3 (Feb. 2021), p. 035301. DOI: 10.1088/1361-6455/abd2d1. URL: <https://dx.doi.org/10.1088/1361-6455/abd2d1>.
- [You+10] Seo Ho Youn et al. “Dysprosium magneto-optical traps”. In: *Phys. Rev. A* 82 (4 Oct. 2010), p. 043425. DOI: 10.1103/PhysRevA.82.043425. URL: <https://link.aps.org/doi/10.1103/PhysRevA.82.043425>.



- [You11] Seo Ho Youn. “Bose-Fermi Mixtures of Ultracold Gases of Dysprosium”. PhD thesis. University of Illinois at Urbana-Champaign, 2011. URL: <https://levlab.stanford.edu/sites/default/files/Youn%20%202011%20BOSE-FERMI%20MIXTURES%20OF%20ULTRACOLD%20GASES%20OF%20DYSPROSIUM.pdf>.